The Pennsylvania State University

The Graduate School

College of Engineering

LABORATORY-SCALE BLAST TESTING OF POLYMERS

A Dissertation in

Mechanical Engineering

by

Forrest Robert Svingala

©2012 Forrest Robert Svingala

Submitted in partial fulfillment
of the requirements
for the degree of

Doctor of Philosophy

August 2012

The dissertation of Forrest Robert Svingala was reviewed and approved* by the following:

Gary S. Settles
Distinguished Professor of Mechanical Engineering
Dissertation Advisor
Chair of Committee

Richard A. Yetter
Professor of Mechanical Engineering

Panagiotis Michaleris
Associate Professor of Mechanical Engineering

James Runt
Professor of Polymer Science

Karen Thole
Department Head of Mechanical and Nuclear Engineering
Professor of Mechanical Engineering

* Signatures are on file in the Graduate School

Abstract

There presently exists a great body of work on the blast-relevant properties of metals, ceramics, and geomaterials. These materials have been extensively studied under shock-wave loading for the past 6 decades, and their shock behavior is generally well understood. Comparatively little is known about the shock and blast response of polymeric materials. Advanced polymer systems, such as the polyurethanes and polyureas, have recently shown promise in both ballistic armor and in blast-wave-mitigation applications, but the physics behind the shock performance of these materials is currently under debate. As a first step in understanding the behavior of these materials, and to optimize the performance of these systems, their properties under shock loading must be determined. This work develops a suite of optically-based, laboratory-scale experimental techniques to measure the response of these polymers to blast loading. These techniques are used to determine the blast response and shock Hugoniot of a polycarbonate, a polyurethane and a polyurea. The results compare well with data from previously-published full-scale tests. The optical lab-scale approach to blast testing developed here is also applicable to other transparent and semi-transparent materials, and has a more-limited applicability to opaque materials as well.

Contents

List of Figures **vi**

List of Tables **xiv**

1 Introduction **1**

2 Literature Review **3**

2.1 Polyureas and Polyurethanes 3

2.2 Inverse Parameter Identification Methods for Determination of Material Constitutive Properties 4

2.3 Shock Waves and the Shock Hugoniot 7

2.4 Blast Testing 9

2.4.1 Prediction of Witness Plate Deformation 11

3 Experimental Methods **14**

3.1 Material Specimens 14

3.1.1 Polyurethane and Polyurea Synthesis Procedure 14

3.2 Light Gas Gun Facility 16

3.2.1 Design Considerations 17

3.2.2 Operation of the Light Gas Gun 21

3.3 Shock Wave Transmission 24

3.3.1 Stress Waves 25

3.3.2 Shock Waves 27

3.4 Dynamic Response of Plates Under Blast Loading 30

3.4.1 'Shock Hole' Fixture 31

3.4.2 Optical Deformation Measurement 31

4 Results and Discussion **34**

4.1 Stress Wave Imaging 34
4.2 Shock Wave Imaging and the Shock Hugoniot 35
4.2.1 Constant-Velocity Shock Waves 35
4.2.2 Decelerating Shock Waves 36
4.2.3 Tracer particle development 43
4.2.4 Surface Velocity Measurements 43
4.2.5 Shock Hugoniot Data 50
4.2.6 Energy Dissipation during the Shock-Release Cycle 54
4.3 Dynamic Response of Plates Under Blast Loading 58
4.3.1 Blast Loading 58
4.3.2 Boundary Condition 67
4.3.3 Description of Dynamic Plate Deformation 68
4.3.4 Maximum Deformation Results 78

5 Summary and Conclusions **83**
5.1 Shock Wave Transmission 83
5.2 Dynamic Plate Deformation 84

6 Future Work **86**
6.1 Shock Wave Transmission 86
6.2 Dynamic Plate Deformation 87

7 Appendix 1: Matlab Blast Loading Calculator **88**

8 Appendix 2: Dynamic Plate Deformation Data **96**

List of Figures

2.1 Polyurea and polyurethane chemical formulae. R and R' represent groups of atoms associated with the polyisocyanate and polyol or polyamine used, respectively. 3

2.2 Reference diagram for steady Rankine-Hugoniot equations. Coordinate frame is fixed to the shock wave and material moves from right to left 8

3.1 Schematic of light gas gun facility. 17

3.2 Wave diagram of a projectile impacting an initially stationary sample. Solid black lines represent material interfaces, long-dashed gray lines represent shock waves, and short-dashed gray lines represent release waves. L is the length of the projectile, t_i is the time of impact, and t_s is the time of separation caused by the release wave reaching the projectile-sample interface. $t_{pressurepulse} = t_s - t_i$ 18

3.3 (a) Schematic diagram of projectile yaw caused by poor tolerance of re-machined projectiles; diameter mis-match is exaggerated for clarity. (b) Shadowgraph image with significant aluminum dust blocking parts of the experiment. Projectile motion is from left to right. 20

3.4 The shape of the frangible diaphragms used with this gas gun. The front edges are angled to center the diaphragm over the chamber by contact with the flange bolts. 21

3.5 A plot of average burst pressures for diaphragms using 1–6x sheets of transparency material. 22

3.6 A plot comparing the velocity of a 50 g projectile as predicted by Equation 3.3, assuming an effectively infinite chamber and neglecting friction, to experimentally measured velocities. While Equation 3.3 consistently over-predicts the projectile velocity by about 10%, it may still be used as a rough guide for experimental design. 23

3.7 A schematic diagram of the shadowgraph system used in this investigation. 24
3.8 4 x 4 x 30 cm polycarbonate bar, a) pretest, b) raw shadowgram of stress wave, c) same image after processing, wave motion is from left to right. 26
3.9 Stress wave motion in polycarbonate demonstrating the development of a 1-D planar stress wave from an initial point load. Wave motion is from left to right, and times given are elapsed time after EBW detonation. 27
3.10 Diagram of the lateral relief process after passage of a shock wave. The aluminum projectile moves from left to right. The shock wave in the polymer sample is represented by a solid line, and the first expansion wave from each surface is represented by a dashed line. All Hugoniot measurements in the present work are made in the triangular region of 1-D strain before the arrival of the expansion wave front. 28
3.11 Schematic of charge arrangement used to induce decelerating shock waves in polyurethane 29
3.12 (a): Schematic wave diagram of explosively-generated shock motion in polyurethane. A indicates direct light from the detonation of the explosive, B, the primary shock wave, C, a few massless tracer particles, and D, the free surface velocity. Solid lines represent shock waves, and dashed lines represent expansion waves. 30
3.13 Fixture used in plate blast testing 31
3.14 Stereoscopic high-speed camera arrangement allowing time-resolved 3-D strain measurement during a shock-hole test 32
3.15 Left, witness plate clamped in test fixture, with random speckle pattern for digital image correlation. Black rectangle outlines area of interest. Right, example deformation field obtained in plate blast testing. . . . 33

3.16 Typical pair of images of a calibration target with 25 mm spacing between dots. 34

4.1 (a): Raw frame from the high-speed shadowgraph record, with cropped area bounded in white. (b): Streak diagram of a ballistic impact experiment in polyurethane, assembled from a temporal series of cropped images. The ballistic projectile enters from the left, striking the sample and producing a shock wave. The projectile-sample interface is indicated by A, and the primary shock is labeled as B. U_{fs} is measured in the linear portion of the free surface record, C. An air shock transmitted through the sample is labeled as D. (c): Wave diagram of the test shown in (b). Features are labeled as in (b), with the addition of a massless tracer particle, E. Solid lines represent shock waves, and dashed lines represent expansion waves. 37

4.2 (a):Shadowgraph streak diagram of ballistic impact test in an opaque polyurea. Production of voids by the reflected rarefaction complicates motion of the free surface, C. U_{p2} is, instead, measured at the projectile–sample interface, A, to avoid this phenomena. D indicates the shock wave transmitted through the sample into the air. (b):Wave diagram of the test shown in (a). Features are labeled as in (a), with the addition of the primary shock, B, a massless tracer particle, E, and area of void formation/collapse, F. Solid lines represent shock waves, and dashed lines represent expansion waves. 38

4.3 Micrographs, left, untested polyurea; right, polyurea with voids formed by tensile stress after shock wave reflection. 39

4.4 Schematic pressure-time plot at the high-explosive–polymer interface. P_1 is the unshocked pressure of the sample, P_{im} is the pressure calculated by impedance matching between the explosive products and the sample, and t_{det} the time of detonation. 40

4.5 (a): Shadowgraph streak diagram of explosively-generated shock motion in polyurethane. A indicates direct light from the detonation of the explosive, B, the primary shock wave, C, the free surface motion , D, the transmitted air shock, and E, a few tracer bubbles. (b): Wave diagram of the test shown in (a), with primary shock curvature exaggerated for clarity. Solid lines represent shock waves, and dashed lines represent expansion waves. 42

4.6 Shadowgraph image of glass micro-spheres in polyurethane. Sample width is approximately 20 mm. 44

4.7 (a)Schematic representation of the deformation of the optical surfaces of the bar during a Hugoniot test, with vertical axis exaggerated for clarity. $\theta \approx 2$ degrees in actual testing. (b) Image of the surface deformation of a polyurethane sample during a Hugoniot test. All internal velocity measurements are made during the region of linear surface shape. 45

4.8 Image of a ballistic projectile and a polyurea sample with random speckle pattern for surface velocity measurements. 46

4.9 Plot of surface velocity rise time as a function of distance traveled in the sample for polyurethane and a P-1000 polyurea. 46

4.10 Schematic diagram of a shock wave moving through a heterogeneous material. The 'primary' phase with a low sound speed is shown in gray, and the 'secondary' phase with a high sound speed is shown in white. Shock wave reflections are omitted for clarity. Initially, the shock front is smooth and sharp as in (a). As the shock encounters a heterogeneity (b) a portion of the wave front enters the secondary phase. Due to the increased sound speed in the secondary phase, the shock wave travels more quickly, while the shock in the primary phase continues at U_s. After the shock has exited the secondary phase, (c), the shock front is spatially dispersed in the primary phase. 48

4.11 Tapping mode atomic force microscopy phase images (scale=5°) of a bulk-polymerized polyurea. (a) a 1x1 micrometer image, (b) a 0.5x0.5 micrometer image showing the ribbon-like, nano-scale hard domains in light orange. 49

4.12 Shock Hugoniot data for Polyurethane. Empty circles represent explosively-generated data, with associated error band represented by dot-dot-dash lines. Filled circles represent ballistic projectile data, with sub-symbol-size error. The dashed line represents an extrapolated fit from LANL gas-gun data. 51

4.13 Shock Hugoniot data for hot-cured polyurea. Black circles represent data from experiment 1, with no front lighting. Gray circle represent data from experiment 2, with front lighting to reduce the measurement error in U_{p2}. Data and a linear fit proposed by Mock et al. are shown for comparison. 52

4.14 Comparison of shock Hugoniot data for room-tempertuare-cured and hot-cured polyurea. 53

4.15 Plot of the shock-release cycle on pressure-specific volume coordinates. The material is shocked along the Rayleigh line from state 1-2, and released quasi-isentropically along the Hugoniot curve from 2-1. The area between the curves represents the shock energy dissipated as heat for one shock-release cycle. 54

4.16 Plot of the shock-release cycle for aluminum, polyurethane and polyurea on Pressure-specific volume coordinates. The area between the curves represents the shock energy dissipated as heat for one shock-release cycle. Metals transmit shock waves efficiently, with with very little shock energy dissipated as heat. The two polymers studied here dissipate orders of magnitude more energy in the shock-release process than does aluminum. 56

4.17 Plot of the shock energy dissipated by the shock-release process as a function of shock pressure for aluminum, polyurethane, and polyurea. Polyurea dissipates the most shock energy of these materials, with its advantage increasing with increasing shock pressure. 57

4.18 Schematic diagram of a typical pressure-time profile associated with an explosive blast wave. P^+ is the gauge overpressure immediately behind the shock wave, t_0 is the arrival time of the shock wave, and T^+ is the positive overpressure duration. 59

4.19 Plot of the experimentally measured waveform parameter (α) as a function of scaled charge stand-off, and linear fit to these data (equation 4.4). Pressure traces were measured by M. Biss, and alpha parameters were determined by the present author. 60

4.20 Diagram of a spherical shock wave impinging on a plate. At centerline, the shock reflects normally to the surface of the plate, but at all other locations the shock reflects at an oblique angle. 61

4.21 Schematic diagram of (a)an oblique shock reflection and (b)its steady flow counterpart. 62
4.22 (a) Schematic diagram of a regular oblique shock wave reflection. Such a regular reflection occurs for angles of incidence below 40 degrees. (b) Schematic diagram of a Mach reflection, which occurs for angles of incidence greater than 40 degrees. 64
4.23 Plot of calculated reflected overpressure as a function of time at the center of a witness plate. Test conditions: 0.947g charge at a 12.5cm stand-off distance 65
4.24 Plot of calculated maximum reflected overpressure as a function of radial location on a witness plate. Test conditions: 0.947g charge at a 12.5cm stand-off distance 66
4.25 Polycarbonate plate deformation plots 0.5 ms after blast loading from a 1g charge at a 12.5 cm stand-off. A center-seeking deformation wave is observed for both boundary conditions tested: (a) Clamped boundary condition, (b) unclamped boundary condition. 67
4.26 Schematic diagram of the unclamped boundary condition. In this configuration, the polymer test plate is placed in front of, and in contact with, the shock hole fixture, instead of being clamped into the fixture as in Figure 3.13. 68
4.27 Deformation of polyurea plates in the (a) small stand-off regime, and (b) large stand-off regime. Both frames are taken at the time of maximum deformation, 0.62 ms and 2.1 ms, respectively. 69

4.28 Plot of maximum reflected overpressure as a function of radial location on the witness plate. Short stand-off distances lead to a non-uniform centrally-weighted overpressure loading, while large stand off distances lead to more uniform overpressure loading. Test conditions: 0.947 g charge at a 12.5 cm stand-off distance and 0.935 g charge at a 2.5 cm stand-off distance 70
4.29 Plot of deformation and velocity as a function of time for a P-1000 polyurea witness plate exposed to a 0.947 g charge at a 12.5 cm stand-off distance. 72
4.30 Plot of deformation as a function of radial location for a P-1000 polyurea witness plate exposed to a 0.947 g charge at a 12.5 cm stand-off distance. 73
4.31 Plot of the surface shape of a P-1000 polyurea witness plate 0.1 ms after exposure to the blast wave produced by a 0.947 g charge at a 12.5 cm stand-off distance. 74
4.32 Plot of the surface shape of a P-1000 polyurea witness plate 0.3 ms after exposure to the blast wave produced by a 0.947 g charge at a 12.5 cm stand-off distance. 75
4.33 Plot of the surface shape of a P-1000 polyurea witness plate 0.8 ms after exposure to the blast wave produced by a 0.947 g charge at a 12.5 cm stand-off distance. 76
4.34 Plot of the surface shape of a P-1000 polyurea witness plate 1.2 ms after exposure to the blast wave produced by a 0.947 g charge at a 12.5 cm stand-off distance. 77
4.35 Plot of unnormalized plate deformation data. A general trend towards smaller deformations at large stand-off distances is observed. 80
4.36 Plot of normalized plate deformation data. Only large stand-off ($R_{scaled} > 7cm$) experiments are included in this plot. 81

List of Tables

4.1 Longitudinal sound speeds as observed by ultrasound and shadowgraph techniques, all values in m/s. 34

4.2 Summary of the maximum deformation results for P-1000 polyurea plates 82

4.3 Summary of the maximum deformation results for P-650 polyurea plates 82

4.4 Summary of the maximum deformation results for polyurethane plates 83

4.5 Summary of the maximum deformation results for polycarbonate plates 83

8.1 Out-of-plane deformation of a 2.7 mm-thick P-650 Polyurea plate, exposed to a 0.949 g PETN charge at a 12.5 cm stand-off distance. . . 97

8.1a Continuation of table 8.1 98

8.1b Continuation of table 8.1 99

8.1c Continuation of table 8.1 100

8.1d Continuation of table 8.1 101

8.1e Continuation of table 8.1 102

8.1f Continuation of table 8.1 103

8.2 Out-of-plane deformation of a 3 mm-thick P-1000 Polyurea plate, exposed to a 0.935 g PETN charge at a 2.5 cm stand-off distance. . . . 104

8.2a Continuation of table 8.2 105

8.2b Continuation of table 8.2 106

8.2c Continuation of table 8.2 107

8.2d Continuation of table 8.2 108

8.2e Continuation of table 8.2 109

8.2f Continuation of table 8.2 110

8.3 Out-of-plane deformation of a 3 mm-thick P-1000 Polyurea plate, exposed to a 0.947 g PETN charge at a 12.5 cm stand-off distance. . . 111

8.3a Continuation of table 8.3 112

8.3b Continuation of table 8.3 113

8.3c Continuation of table 8.3 114
8.3d Continuation of table 8.3 115
8.3e Continuation of table 8.3 116
8.3f Continuation of table 8.3 117

1 Introduction

Recently, there has been a push to develop polymer-based systems to protect people and equipment from explosively-generated shock waves (air blasts). This is due, in part, to anecdotal evidence that some polymers may be uniquely suited to this role due to an enhanced ability to attenuate or disperse the energy of a shock wave [1]. Interest is primarily focused on protection from relatively low-pressure shock waves, i.e., those with overpressures in the kPa–MPa range. These waves are typically produced by air blasts in the mid-to-far-field. Soldiers in Iraq and Afghanistan often encounter and survive shock waves of this magnitude, which can result in mild to severe traumatic brain injury (TBI), and other long-term medical problems [2, 3]. Thus, many recent experimental [4–7] and computational [8–10] efforts have centered around the system-level response of polymer and polymer-composites to these types of threats.

To successfully predict the response of any material to blast loading, two main relationships must be defined: the shock Hugoniot, which determines the thermodynamic state of a material after shock passage, and a constitutive model, which defines the state of stress and strain in the material. Research into these relationships in metals exposed to blast loading began in earnest in the 1940s and 50s. These studies focused primarily on common metals loaded by very-high-pressure shock waves (overpressure $\geq$ 10 GPa) through direct contact with a high-explosive, or high-velocity ballistic impact [11–14]. Many studies have since been published on the response of metals to shock loading, and, consequently, their behavior is relatively-well understood.

Comparatively few publications, however, have focused on these fundamental relationships for polymeric materials under blast loading. Those that do exist have primarily studied pressures in the 1–50 GPa range, far above the pressures produced by interaction with a blast wave in air [15]. This leaves few experimental data to inform the design of blast-resistant polymer systems.

Traditional blast experiments are performed at the full-scale, often using many kilograms of high-explosive. This makes these experiments difficult to instrument and troublesome to perform, due to the many required safety precautions and the expense of a licensed outdoor explosives range. These factors severely limit the number of experiments that may be performed, and they also limit the amount and types of data that may be collected.

The goal of the present work is to develop a collection of novel, optically-based techniques to quantitatively measure the response of transparent and opaque polymeric materials to explosive blast loading. These techniques can be divided into two main areas: shock transmission experiments, which define the shock Hugoniot of the material, and dynamic plate response experiments, which produce data supporting the development of constitutive models. All techniques presented here are performed at the laboratory scale, using either a single-stage light gas gun or less than 3 g of high-explosive to shock the material under study. This allows at least some of the traditionally-cumbersome and expensive work of full-scale blast testing to be brought into the lab, where experiments are more easily and controllably instrumented with a sizable reduction in cost and investigator risk. In this dissertation these techniques have been developed and applied to measure the blast response of a polycarbonate, a polyurethane, and a polyurea.

2 Literature Review

2.1 Polyureas and Polyurethanes

The polyureas and polyurethanes comprise a versatile class of organic polymers. Their bulk properties are chemically adjustable over a wide range, making them easily tailorable to a wide variety of applications, such as synthetic fibers and foams, adhesives and sealants, and injection-molded hard plastic parts [16]. They are made by the reaction of a polyisocyanate with a polyol or a polyamine, to form a polyurethane or polyurea, respectively. A basic diagram of these chemical systems is shown in Figure 2.1. Each polymer chain consists of alternating hard and soft segments in proportions varied by reactant selection [16]. Depending on the reactants and processing techniques used, these can be homogeneously distributed in a non-phase-separated polymer, or self-assembled into nano-scale hard and soft domains, resulting in a phase-separated polymer.

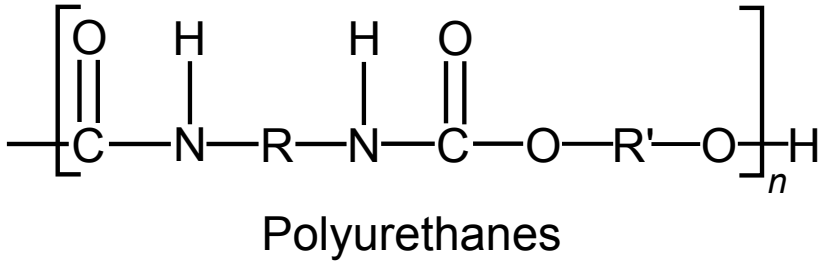

Polyurethanes

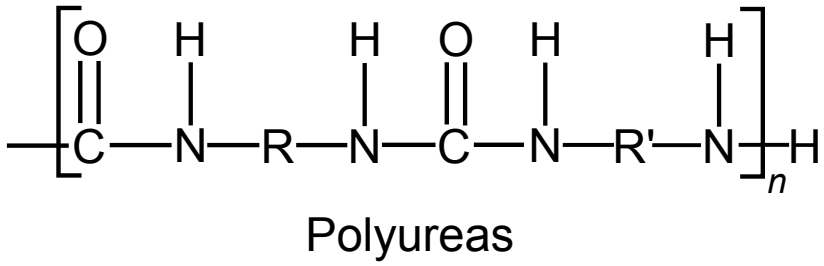

Polyureas

Figure 2.1: Polyurea and polyurethane chemical formulae [16]. R and R' represent groups of atoms associated with the polyisocyanate and polyol or polyamine used, respectively.

Recently, anecdotal evidence of polyureas exhibiting desirable properties under blast and ballistic loading has sparked several research programs. Resulting experimental and computational work with polyureas has shown them to be promising candidate materials for both blast and ballistic-mitigation applications [5, 7, 10, 17]. The physics behind these potentially-desirable properties is still under study and debate. An atomistic-scale computational simulation by Grujicic et al. suggests that shock passage through a phase-segregated polyurea results in breakage of many hydrogen bonds, a process that absorbs significant energy [18]. Other sources of these desirable shock-response properties may include a second-order phase change, plastic deformation of the hard phases and shock-wave dispersion. To date, there are no detailed experimental papers examining these effects, leaving modeling efforts with little to go on. In fact, even the most basic of shock wave relations–the shock Hugoniot–for polyurea is inadequately defined in the literature, with only a single reference found covering a relatively-narrow range of shock strengths [19].

2.2 Inverse Parameter Identification Methods for Determination of Material Constitutive Properties

Inverse problems are those which seek to determine the causes associated with an observed effect, e.g., the determination of unknown material properties from the application of a known load and an observed strain field. Traditionally, material model parameters are determined in 1-D, homogeneous states of strain. This simplifies data collection and analysis, but fails to reflect the conditions present when the material is subjected to more-complex loading. It has been shown that polyurea material models derived from quasi-static, low-rate impact, and and from split-Hopkinson bar data, collectively with strain rates from .001–10,000 s^{-1}, do not properly characterize the shock properties of this material [20]. All of these tests were designed to induce simple, homogeneous strain fields.

With the advent of digital image correlation software like VIC-3D [21], it is feasible to accurately measure complex strain fields, such as those present in the blast testing of thin plates. However, even with well-defined loading, boundary conditions, and resulting strains, the evaluation of constitutive modeling parameters from such data is not trivial. Inverse parameter identification methods offer an opportunity to use these complex strain fields to determine constitutive parameters under more realistic conditions.

In cases of simple loading, the inverse problem is easily solved algebraically. However, if the loading is highly dynamic or the induced strain is heterogeneous, an algebraic solution to the inverse problem may not exist. In these cases, an iterative finite-element (FE) modeling technique may be applied. In this method, the experiment is simulated using finite-element modeling with an assumed set of material properties. The simulated and experimental strain fields are then used to compute a 'cost' function, which is minimized in order to determine values of the correct material parameters. The least-squares form of this cost function is shown below in equation 2.1:

$$C(\bar{p}) = \sqrt{\sum_{i=1}^{n} \left(\frac{\epsilon_i^{FE}(\bar{p}) - \epsilon_i^{exp}}{\epsilon_i^{exp}} \right)^2} \tag{2.1}$$

where $\bar{p}$ is a vector containing the unknown material properties, n is the number of experimentally-measured strain points, and ϵ_i^{FE} and ϵ_i^{exp} represent the resulting strains from the FE model and experiment, respectively. Formally, equation 2.1 is minimized by finding values of $\bar{p}$ which satisfy $\frac{\partial C(\bar{p})}{\partial p_j} = 0$. By applying a Taylor series approximation to the computated strains, one can develop a sensitivity matrix S_{ij} in terms of each element of $\bar{p}$ and each strain component. As an example, Cooreman et al. determine S_{ij} in 2D cartesian coordinates for the case of in-plane deformation as equation 2.2 [22]:

$$S_{ij} = \begin{bmatrix} \left(\frac{\partial \epsilon_x^{FE}}{\partial p_1}\right)_1 & \left(\frac{\partial \epsilon_x^{FE}}{\partial p_2}\right)_1 & \cdots & \left(\frac{\partial \epsilon_x^{FE}}{\partial p_m}\right)_1 \\ \left(\frac{\partial \epsilon_y^{FE}}{\partial p_1}\right)_1 & \left(\frac{\partial \epsilon_y^{FE}}{\partial p_2}\right)_1 & \cdots & \left(\frac{\partial \epsilon_y^{FE}}{\partial p_m}\right)_1 \\ \left(\frac{\partial \epsilon_{xy}^{FE}}{\partial p_1}\right)_1 & \left(\frac{\partial \epsilon_{xy}^{FE}}{\partial p_2}\right)_1 & \cdots & \left(\frac{\partial \epsilon_{xy}^{FE}}{\partial p_m}\right)_1 \\ \left(\frac{\partial \epsilon_x^{FE}}{\partial p_1}\right)_2 & \left(\frac{\partial \epsilon_x^{FE}}{\partial p_2}\right)_2 & \cdots & \left(\frac{\partial \epsilon_x^{FE}}{\partial p_m}\right)_2 \\ \left(\frac{\partial \epsilon_y^{FE}}{\partial p_1}\right)_2 & \left(\frac{\partial \epsilon_y^{FE}}{\partial p_2}\right)_2 & \cdots & \left(\frac{\partial \epsilon_y^{FE}}{\partial p_m}\right)_2 \\ \left(\frac{\partial \epsilon_{xy}^{FE}}{\partial p_1}\right)_2 & \left(\frac{\partial \epsilon_{xy}^{FE}}{\partial p_2}\right)_2 & \cdots & \left(\frac{\partial \epsilon_{xy}^{FE}}{\partial p_m}\right)_2 \\ \vdots & \vdots & \ddots & \\ \left(\frac{\partial \epsilon_x^{FE}}{\partial p_1}\right)_n & \left(\frac{\partial \epsilon_x^{FE}}{\partial p_2}\right)_n & \cdots & \left(\frac{\partial \epsilon_x^{FE}}{\partial p_m}\right)_n \\ \left(\frac{\partial \epsilon_y^{FE}}{\partial p_1}\right)_n & \left(\frac{\partial \epsilon_y^{FE}}{\partial p_2}\right)_n & \cdots & \left(\frac{\partial \epsilon_y^{FE}}{\partial p_m}\right)_n \\ \left(\frac{\partial \epsilon_{xy}^{FE}}{\partial p_1}\right)_n & \left(\frac{\partial \epsilon_{xy}^{FE}}{\partial p_2}\right)_n & \cdots & \left(\frac{\partial \epsilon_{xy}^{FE}}{\partial p_m}\right)_n \end{bmatrix} \tag{2.2}$$

where n is the number of unknown parameters.

Many techniques for populating the sensitivity matrix have been reported in the literature, including finite-difference, adjoint, and analytical methods [23]. Once the sensitivity matrix is populated, the updated $\bar{p}$ is calculated by a simple Gauss-Newton algorithm (2.3):

$$\bar{p}_{\ updated} = (\bar{\bar{S}}^T \cdot \bar{\bar{S}})^{-1} \cdot \bar{\bar{S}}^T \cdot (\epsilon^{exp} - \epsilon_i^{FE}(\bar{p})) \tag{2.3}$$

The updated material properties are then used as input to the finite element model, and the process is repeated. Iterations continue in this way until equation (2.1) is minimized to within a desired error tolerance.

This method was used to determine the constitutive properties of a steel alloy under bi-axial tension [22] and an aluminum alloy in a combination of tension and bending [24]. This method has also been applied to blast testing, where the interaction pressure was determined between explosively-shocked sand and a thin aluminum plate of known properties [25]. Blast testing has apparently not been applied to determine material properties using this method, however.

2.3 Shock Waves and the Shock Hugoniot

Shock waves are sharp discontinuities in pressure, density, and internal energy in any continuous material. They can result from a localized rapid release of energy, as in an explosion, or from a high-velocity impact. Knowledge of material shock response is critical for the design of systems that may be subjected to explosive or projectile loading, e.g., infantry helmets, ship hulls, building facades, etc. Shock response is defined by the Rankine-Hugoniot equations, which represent conservation of mass, momentum, and energy across a shock wave. These equations define a locus of possible pressure-density-energy states that a material may attain across a shock wave. The steady-state form of these relations is given in equations (2.4), (2.5) , and (2.6)

$$\frac{\rho_2}{\rho_1} = \frac{U_s - U_{p1}}{U_s - U_{p2}} \tag{2.4}$$

$$P_2 - P_1 = \rho_1 (U_{p2} - U_{p1})(U_s - U_{p1}) \tag{2.5}$$

$$e_2 - e_1 = \frac{1}{\rho_1} \frac{(P_2 U_{p2} - P_1 U_{p1})}{(U_s - U_{p1})} - \frac{1}{2}(U_{p2}^2 - U_{p1}^2) \tag{2.6}$$

where, ρ represents density, U_s represents shock wave velocity, U_p represents the velocity of the material through which the shock passes, and e represents internal energy. Variables with a subscript of 1 represent values in the unshocked material while subscript 2 represents the shocked values, as shown in Figure 2.2. Once the shock Hugoniot of a material is defined, its response to a given shock wave can be calculated. Of particular interest are the pressure induced by the passage of the shock wave and the amount of shock energy dissipated in the shock-relief process. These values are important metrics in designing systems that can both survive a given blast overpressure and reduce transmitted shock energy by attenuating the wave as it passes.

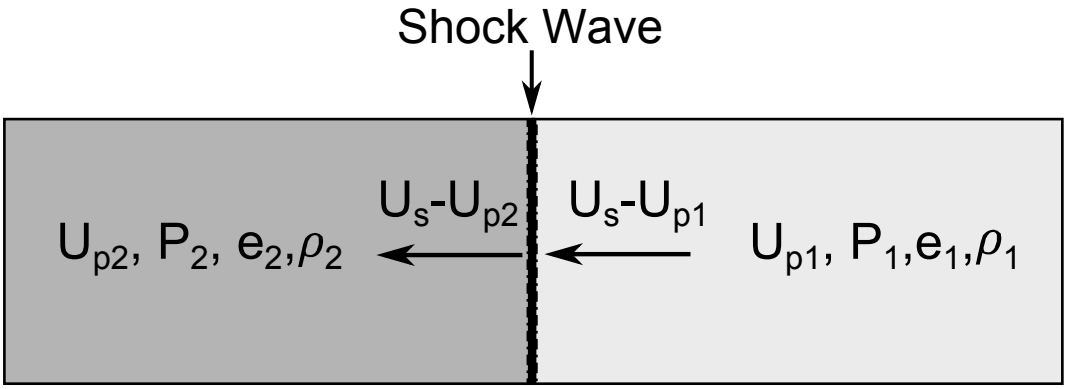

Figure 2.2: Reference diagram for steady Rankine-Hugoniot equations. Coordinate frame is fixed to the shock wave and material moves from right to left

Experimentally measuring the shock Hugoniot requires the initiation of a shock wave in the material of interest and simultaneous measurement of any two variables in the shocked state, i.e., U_{p2}, P_2, U_s, e_2, or ρ_2. In practice, U_{p2}, P_2, and U_s are the most readily observed. U_s and U_{p2} are commonly measured by laser interferometry at the back surface of the sample and P_2 may be measured with frangible manganin gages at the sample surface[26, 27]. If the material of interest has at least some transparency, the schlieren or shadowgraph technique, combined with high-speed imaging, allows the direct visualization of a shock wave in the bulk material[28]. Per Settles[28], shadowgraphy is the preferable method if the goal is shock wave imaging. Yamada et al. developed the steady shock Hugoniot for PMMA optically, using shadowgraphy and a high-speed-film streak camera[29]. All of these tests occur with steady state shock motion, providing only a single point of the shock Hugoniot curve. Thus, determining the entire shock Hugoniot in this manner requires an extensive series of shock experiments.

There are many methods of initiating a shock wave in the laboratory, the most common being impact by a ballistic projectile accelerated up to as much as several km/s by a light gas gun [30]. Walsh and Christian used an explosively-driven shock wave to measure Hugoniot equation-of-state data [13]. In that work, sheets of high explosive were detonated in direct contact with the materials of interest. By using

thin samples (6mm–50mm) and thick explosive sheets (50mm–305mm), pressure at the input surface of the sample could be maintained nearly constant for the duration of the test, producing steady shock waves, and Hugoniot data on a point-by-point basis.

While the Rankine-Hugoniot relation properly defines the material state before and after a shock wave, it contains no information about the shape and width of the shock front, i.e. the shock wave profile. An ideal shock wave is represented by the Heavyside step function, with an instantaneous transition from the pre-shock to the post-shock state. In most fluids this shock 'jump' is very nearly ideal. However, in materials with significant viscosity, strength, heat conduction, and/or heterogeneity, the shock profile may deviate significantly from the ideal. Shock fronts in solids and mixed-phase systems, e.g. dusty air, have been observed to have rise times on the order of 2 μs [31, 32]. Tsukinovsky et. al. observed a shock rise time which increased with distance traveled by the shock wave in a polyurethane[33]. The shape of this shock wave profile can be complex, but with proper interpretation it contains a wealth of information about the physical processes occurring when a material is shocked[31]. The shock wave profile is generally measured by velocity interferometer (VISAR) or manganin pressure gages. Investigators interested mainly in the macroscopic shock behavior often invoke the *hydrodynamic approximation* which assumes that the shock front is ideal. This allows the calculation of U_{p2}, P_2, U_s, etc., without considering the details of the shock profile.

2.4 Blast Testing

Traditionally, blast testing has been performed at the full-scale, using kilograms of high-explosive and full- or near-full-size structures of interest[34–36]. Due to the destructive nature of large quantities of high-explosives, these tests are performed outdoors, often with poor control over many experimental variables. In many cases,

one must also be willing to destroy the measurement devices used, making these tests difficult and expensive to perform. For this reason, most investigations rely on a few point-wise measurements of pressure, displacement, and/or velocity. Each test is also quite expensive, due to the quantities of explosive involved, requisite safety precautions, the size of the test structure, and maintenance of a dedicated outdoor explosives range with trained explosives technicians. These factors greatly limit the number of tests which may be practically performed. Full-scale tests are useful in the engineering sense, in that—for a particular loading and test geometry—they provide a measure of which structure performed 'best'. However, the necessarily-crude instrumentation and limited number of tests at full-scale often makes interpretation of the underlying physical mechanisms involved in blast response difficult or impossible. This makes full-scale blast testing less than ideal for scientific research.

Testing at the laboratory scale avoids many of the pitfalls of full-scale testing: individual test cost is much reduced, while safety, repeatability and ease of instrumentation are improved. The observation of the response of a thin plate to explosive loading is one of the simplest laboratory-scale blast response tests. A reasonable body of data exists for thin metal plates subjected to explosive loading (see review paper by Nurick and Martin[37] and work by Hargather and Settles[38]). These data largely consist of measured impulse and maximum central deflection of circular and rectangular plates. For a variety of metals the ratio of this deflection to plate thickness is found to vary linearly with respect to Johnson's damage number, α_0 [37]:

$$\alpha_0 = \frac{I_0^2}{t^2 \rho \sigma_y} \tag{2.7}$$

where I_0 is the impulse per unit area, t is the plate thickness, ρ is the plate density, and σ_y the yield stress. Recent work by Hargather and Settles obtained time-resolved, full-field strain measurements of thin aluminum plates under air-blast loading using

a digital image correlation technique[38]. A linear relationship between maximum deformation and explosive impulse was reported for a single thickness of aluminum plate over a wide range of incident impulses.

No similar body of data for polymeric materials is available. In fact, no data at all of this type for polymer plates are reported in any literature found in the course of this review. Some work on polymer/fiberglass composites under shock tube loading has been done by Tekalur et. al., but several fundamental differences in experimental technique preclude direct comparison with explosive blast data [4, 17, 39].

2.4.1 Prediction of Witness Plate Deformation

The polymer witness plates in the present work experience a complex and unsteady deformation. To better understand this deformation, let us begin with a simpler, steady-state loading case. Consider a thin plate with an applied static pressure and a clamped circular boundary condition at a radius, R. The plate can resist the pressure load in two ways: bending stresses and membrane stresses. The bending response of a plate is inversely proportional to its bending stiffness, D: $D = \frac{Et^3}{12(1-\nu^2)}$, where E is the elastic modulus, t is the plate thickness, and ν is Poisson's ratio. This quantity is analogous to the moment of inertia, I, of a beam in the more-familiar beam bending problem.

For static loading ([40]) it has been shown that the deformation of plates is drastically over-predicted by a bending-only analysis in cases where the maximum deformation is on the order of $t/2$ or greater. In these cases, a significant portion of the load is carried by membrane stresses. These stresses develop as a result of an elongation of the plate radius caused by the deformation. This places the plate surface in tension, and significantly increases plate stiffness. For deformations greater than order t, predictions based solely on the membrane stress have been shown to agree with experimental results [40]. In cases where maximum deformation is of order t,

the bending and membrane contributions to stiffness are of the same order, and both should be considered.

From this point forward, deformations greater than order t will be considered "'large deformations"', and all others will be considered "'small deformations"'. Only large deformations will be examined in this work.

A variety of methods for predicting the deformation of a thin plate subject to uniform impulse loading has been presented in the literature, and many of these methods have been collected in a review paper by Nurick and Martin [37]. Methods considering only the stresses due to bending (such as Hopkins and Prager [12]) were found to severely over-predict the plate response in cases where the loading produced large deformations. Methods considering only the membrane action of the plate (such as work by Symonds and Wierzbicki [41]) were found to compare favorably with experimental results in cases of large deformation. These methods tend to be numerically complex, due to the rigorous application of solid mechanics. Other methods attempt to sidestep the details of solid mechanics in favor of an overall energy balance. Greenspan equated the overall strain energy required to deform the plate to the energy flux in an explosive blast wave, yielding reasonable results for far-field explosions where the blast wave impacts the plate with normal incidence [42]. This method fails, however, for near-field explosions and cases of oblique blast wave incidence. This is due to the fact that the resultant pressure loading is not simply proportional to the energy flux of the blast wave in these cases; the details of the fluid-structure interaction between the plate and the blast wave are of critical importance when reflection is oblique and shock waves are strong. Westine and Baker correctly realized this, and modified the energy method of Greenspan to depend upon the impulse acting on the plate, rather than upon the incident blast wave [42]. Those

authors give the following prediction for static midplate deflection:

$$\delta = (\frac{0.082I^2}{t^2R^2\rho\sigma_y} + 0.101t^2)^{1/2} - 0.637t \tag{2.8}$$

where I is the total impulse loading on the plate, t the plate thickness, R the shock-hole fixture radius, ρ the density of the plate, and σ_y the yield stress of the plate. Predictions using this energy method were found to be in substantial agreement with available experimental data for clamped metal plates.

A moderately-large body of deformation data for clamped metal plates subjected to impulsive loading is available in the literature. Much of these data are collected in a review paper by Nurick and Martin [37]. In this paper, these experiments were non-dimensionalized on the loading axis by a modified Johnson damage number:

$$\phi_c = \frac{I(1 + ln(\frac{R}{R_0}))}{\pi Rt^2(\rho\sigma_y)^{1/2}} \tag{2.9}$$

where I is the applied impulse, R is the radius over which this impulse is applied, R_0 is the unclamped radius of the plate, t is the plate thickness, ρ is the plate density, and σ_y is the yield stress of the plate. The response of the plate is normalized by forming the ratio of the maximum deformation to the thickness of the plate. This normalization procedure produces a roughly-linear band of all metal plate experiments having a uniform impulse loading and clamped boundary condition. Nurick and Martin present a linear fit to these data for use in predicting the peak response of a plate subject to uniform impulse loading. This fit is: $\frac{\delta}{t} = 0.425\phi_c + 0.277$, where δ is the maximum deformation of the plate. The authors suggest an error band of $\pm$ 1 $\frac{\delta}{t}$ on this prediction.

3 Experimental Methods

3.1 Material Specimens

Polycarbonate specimens were obtained from McMaster-Carr as a baseline material for both shock transmission and plate blast testing. All polyurethane and polyurea samples tested in this work were made in-house from commercially available pre-polymers. The polyurethane used here is a transparent, non-phase segregated polymer distributed by Ultralloy as Ultraclear 435 [43].

Two varieties of phase-segregated polyurea were investigated in this work; one based on the Versalink P-1000 oligomeric diamine, and the other based on the Versalink P-650 oligomeric diamine, both manufactured by Air Products [44, 45]. The Versalink products were polymerized with one of two polycarbodiimide-modified diphenylmethane diisocyanate products: Dow Chemical Isonate 143L, or the chemically-similar Huntsman Rubinate 1680. No differences in properties were observed between polyureas made with the Dow Chemical and Huntsman diisocyanates; they will be considered equivalent for the remainder of this work.

3.1.1 Polyurethane and Polyurea Synthesis Procedure

Test specimens were made from polyurethane and polyurea pre-polymers following this procedure:

1. Mass each of the two pre-polymers in two separate containers per the manufacturer's instructions. The unused portion of each pre-polymer should be blanketed with dry argon and sealed with parafilm prior to storage.

2. Expose both pre-polymers to vacuum for at least 15 minutes to remove bubbles. For polyurea, the P-1000 or P-650 component should be heated to 40-50 ° C under vacuum for 7-14 days to remove water. While maintaining vacuum, cool to room temperature prior to use.

3. Pour both pre-polymers into one container and apply vacuum.

4. Mix, under vacuum, for two minutes with a magnetic stirring bar.

5. Pour the reacting mixture into a mold coated with PTFE tape or an appropriate mold release agent.

6. Cure in a humidity-controlled ($RH < 25\%$) environment.

The ultraclear 435 polyurethane samples were cured at room temperature for 24 hours, followed by a hot-cure at 50 ° C for 12 hours. Polyurea bar samples were cured in two ways; samples designated as 'hot cure' were cured at 50 ° C for 24 hours, and samples designated as 'room-temperature-cure' were cured at room temperature for at least 2 weeks. All polyurea plates were cured at room temperature.

Three molds, or forms, were used in this work. The first was a 150 mm x 25 mm x 25 mm mold made of polycarbonate. Bare polycarbonate will stick to both polyurea and polyurethane as they cure. To prevent this, the mold was coated with adhesive-backed PTFE tape from McMaster-Carr. This prevented the bar from sticking to the mold, but lead to surface imperfections due to the texture of the PTFE tape. To improve the optical quality of the sample bars, a 300 mm x 25 mm x 30 mm mold was made from aluminum. Both mold surfaces that contacted the optical surfaces of the bar were polished to a mirror-like finish. This ensures a smooth, high-quality optical surface on the test bars. To prevent the polymers from sticking to the aluminum mold, all aluminum surfaces were treated with Frekote B-15 mold sealant and Frekote 44-NC mold release per the manufacturer's instructions.

The third mold was built to make 45 cm x 45 cm x 1-4 mm polymer plates for shock-hole testing. The base of this mold consisted of a 60 cm x 60 cm x 1 cm sheet of medium density fiberboard covered by a 0.7 mm thick sheet of PTFE. The reacting polymer was held in place by 4, 1 cm x 2.5 cm x 18 cm aluminum bars which had been treated with the Frekote sealant and release products.

Producing samples of the P-1000 polyurea with sufficient transparency to observe internal shock transmission proved to be difficult. The root cause of the difficulty is believed to be related to water absorbed by the pre-polymers [46]. The diamine component will absorb atmospheric moisture if it is not stored under very low humidity conditions; ideally under vacuum [47]. When the pre-polymers are mixed, any water in the diamine component will react with the diisocyante component, producing nano- to micro-scale carbon dioxide bubbles. These bubbles reduce the transparency of the cured material, making it difficult or impossible to employ optical diagnostics. To reduce the water content of the diamine component of polyurea, it is recommended that it be throughly dried under vacuum at elevated temperature for 1-2 weeks. This generally produces acceptably clear samples. Best results, however, are always obtained from fresh pre-polymers that have been unopened since being sealed by the manufacturer.

Air products Versalink P-650 reacts much more quickly than the P-1000 product; it will gel approximately 5 minutes after mixing, while the P-1000 polyurea gels after approximately 15 minutes. This leads to difficulties in mixing and pouring P-650-based polyureas before they gel, and traps a greater proportion of CO_2 bubbles in the cured bar. All of the P-650-based polyurea samples produced in this work were therefore essentially opaque.

3.2 Light Gas Gun Facility

As a part of this work, a light gas gun facility was designed and built to accelerate aluminum slugs to velocities of 50–350 m/s. The gun consists of two main sections, the driver or chamber section, and the barrel or driven section. The chamber section consists of a 1.5 m long, 25.4 mm I.D. schedule 80 steel pipe. This pipe is rated to a working pressure of 24 MPa and a burst pressure of 109 MPa. The barrel section was custom machined by Marlboro Tool and Manufacturing Co., Inc., in Rockaway, NJ.

It consists of a 1.5 m long, 44.5 mm O.D. 4140 steel tube, with a 25.3 ± 0.08 mm hole drilled through the length (Figure 3.1). This hole was gun-drilled on a lathe to ensure straightness, and honed smooth. The barrel has a hardness of 32 on the Rockwell C scale. It attaches to the chamber section with a standard 4-bolt pipe flange.

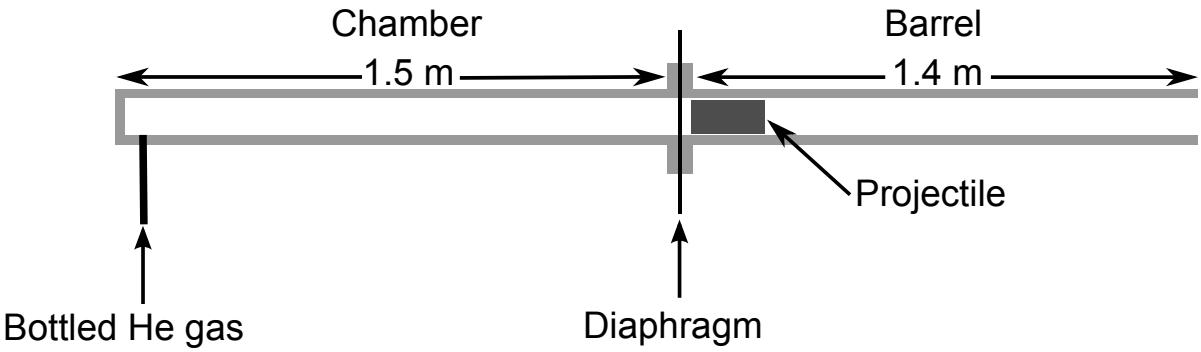

Figure 3.1: Schematic of light gas gun facility.

3.2.1 Design Considerations

The main variables in designing a high-speed light gas gun are the bore diameter and the desired range of projectile velocities. The bore diameter is directly related to the maximum distance that a 1-D constant-velocity shock wave may travel in the sample material. For weak shock waves ($M < 1.5$) the wave may be considered 1-D steady for a transmission distance of up to one projectile diameter [30]. Strong shocks experience more viscous dissipation, and therefore are only expected to maintain a constant velocity for approximately 2/3 of a projectile diameter [30]. A bore diameter of 25 mm was chosen to allow a long enough ($10\mu s$) pressure pulse to accurately measure the shock velocity, while keeping machining and material costs within reason.

The desired projectile velocity range is determined by the strength of the shock waves to be induced in the target materials. A simple 1-D impedance-match calculation can be made, given known shock Hugoniots of the target and projectile materials. If the Hugoniot of the target is unknown, as was the case for polyurea in this work, estimates can be made from the shock Hugoniot of a similar material. Thus, a pro-

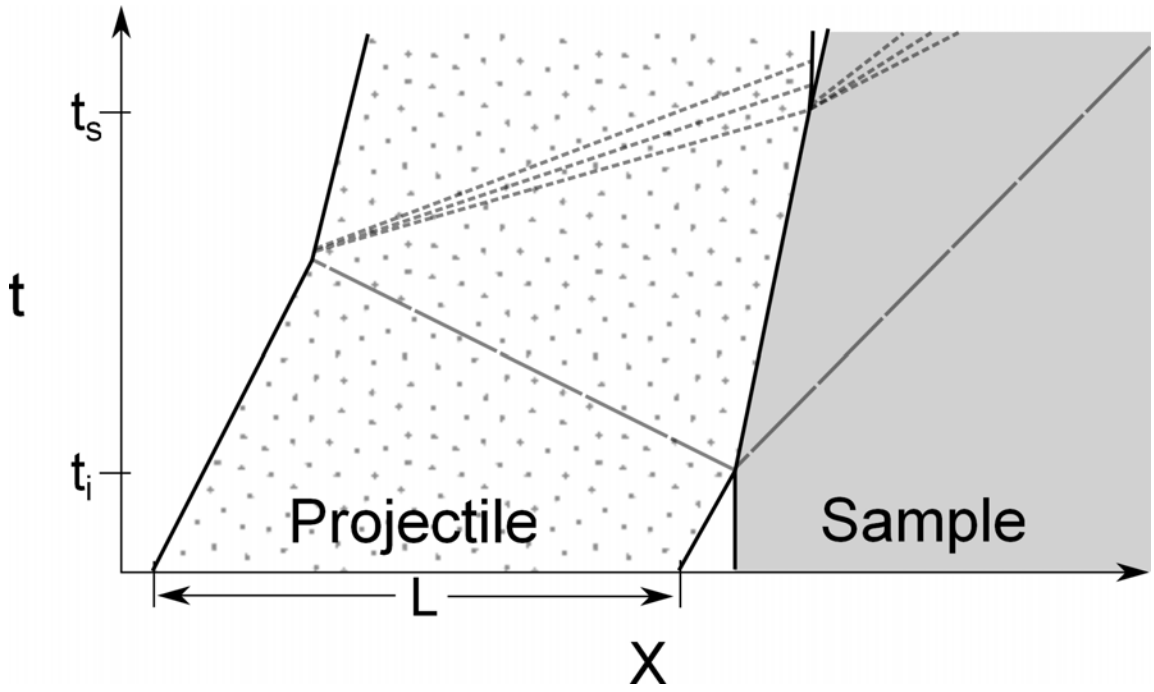

Figure 3.2: Wave diagram of a projectile impacting an initially stationary sample. Solid black lines represent material interfaces, long-dashed gray lines represent shock waves, and short-dashed gray lines represent release waves. L is the length of the projectile, t_i is the time of impact, and t_s is the time of separation caused by the release wave reaching the projectile-sample interface. $t_{pressurepulse} = t_s - t_i$

jectile velocity range of 50–350 m/s was estimated from the known shock Hugoniot of polyurethane, and the shock strengths of interest ($U_{p2} \leq 250 m/s$). Given this maximum projectile velocity, the barrel and chamber lengths may be calculated [48].

The length of the gas-gun projectiles used is also an important consideration. Higher velocities may be reached with shorter projectiles, due to their reduced mass. However, the length of the projectile also determines the length of the steady pressure pulse applied to the sample. The pressure at the impact surface remains constant until a release wave reflected from the rear of the projectile reaches the sample. At this point the projectile and sample separate, and a series of release waves enter the sample. These waves will catch up to the shock wave in the sample and reduce its velocity. This is shown schematically by the wave diagram in Figure 3.2. The length of the impact pressure pulse can be estimated for weak shocks by the following

equation:

$$t_{pressurepulse} \approx L/a_0 \tag{3.1}$$

where L is the length of the projectile and a_0 is the sound speed in the projectile material.

Finally, the tolerance on bore diameter and projectile diameter influence the minimum length projectile which may be used. Shorter projectile lengths and looser tolerances will allow the projectile to yaw inside the barrel. This leads to abrasion and the production of aluminum dust which obscures the experiment, and, in extreme cases, may cause the projectile to become jammed in the barrel (Figure 3.3). For this work, projectiles were machined to 25.3 mm $\pm$ .01 mm diameter, which is 0.025 mm below the measured mean diameter of the bore. New projectiles with these tolerances were fired without problems for projectile lengths down to 38 mm. After use, projectiles were often found to be plastically deformed; these projectiles were re-machined prior to re-use, with a tolerance on the order of + 0 - 0.1 mm. These re-machined projectiles often showed signs of yawing at lengths below 50 mm. Therefore, reuse of projectiles with $L \leq 50mm$ was discontinued. Significant yawing has not be observed with the longer projectiles.

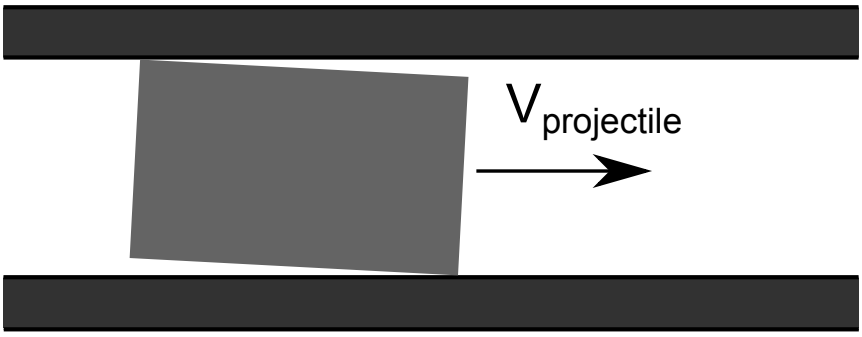

a

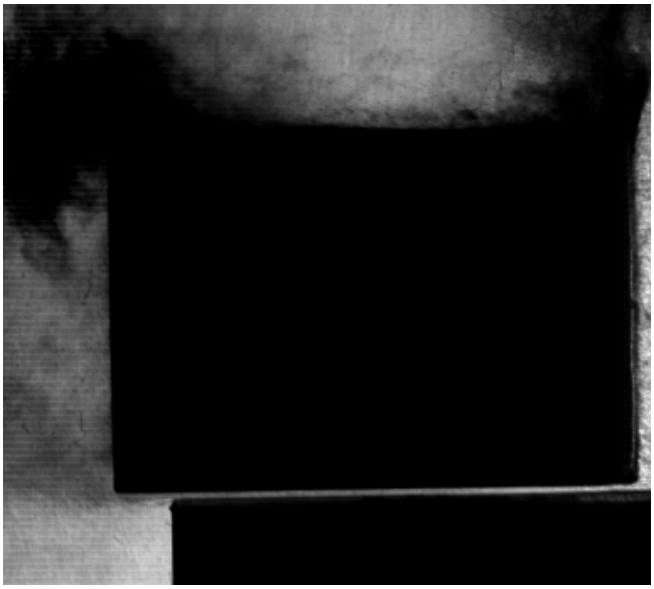

b

Figure 3.3: (a) Schematic diagram of projectile yaw caused by poor tolerance of re-machined projectiles; diameter mis-match is exaggerated for clarity. (b) Shadowgraph image with significant aluminum dust blocking parts of the experiment. Projectile motion is from left to right.

3.2.2 Operation of the Light Gas Gun

A light gas gun uses a low-density gas under high pressure to accelerate a projectile to the desired velocity. Prior to firing, a frangible diaphragm is placed between the chamber and barrel sections of the gun, cut as shown in Figure 3.4. The projectile is then loaded at the muzzle and pushed into place at the diaphragm end of the barrel with a wooden dowel. The chamber gradually filled with bottled He until the diaphragm fails at its burst pressure. The projectile is then accelerated by the high pressure gas behind it over the length of the barrel. Projectile velocity is controlled by the burst pressure of the diaphragm.

The diaphragms used in this work were cut from sheets of plastic transparency material intended for laser printers. A single sheet was found to have a nominal burst pressure of approximately 1.9 MPa. Increased burst pressures were achieved by using multiple sheets per diaphragm, the nominal burst pressures for several cases are shown in Figure 3.5. 3.2 mm polyester sheet (McMaster-Carr) was also tested as a diaphragm material, but it did not burst at pressures up to 10 MPa. Exceeding 10 MPa in the chamber section of the gas gun was deemed not necessary and unsafe, thus this polyester material was not used as a diaphragm in this work.

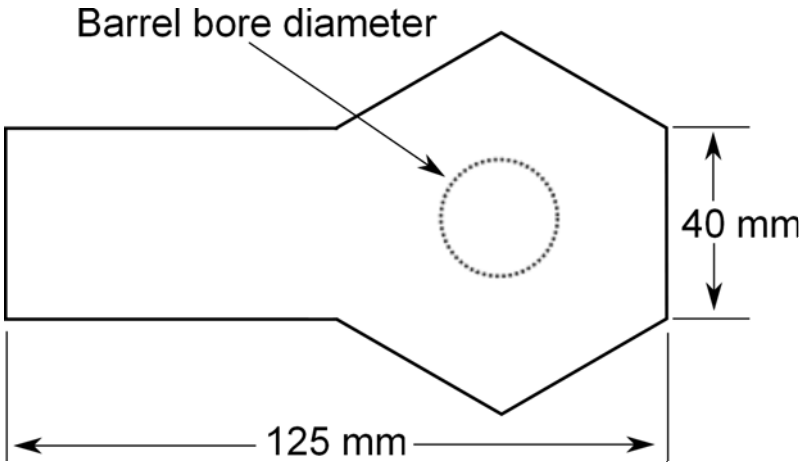

Figure 3.4: The shape of the frangible diaphragms used with this gas gun. The front edges are angled to center the diaphragm over the chamber by contact with the flange bolts.

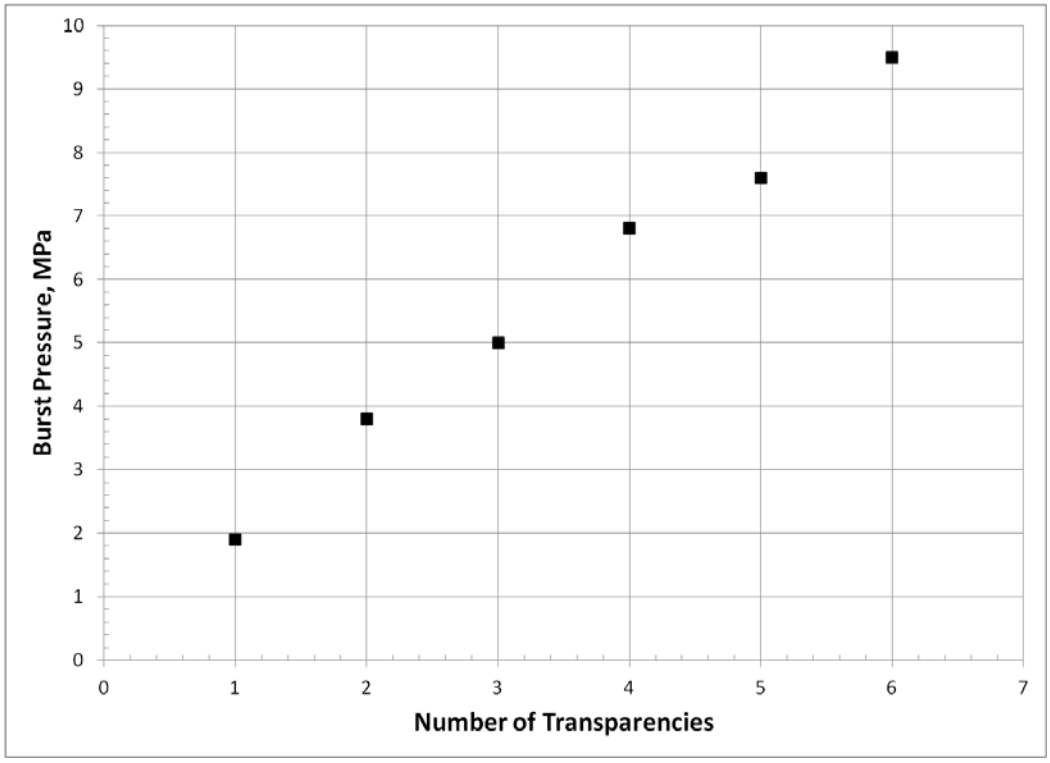

Figure 3.5: A plot of average burst pressures for diaphragms using 1–6x sheets of transparency material.

The velocity of a projectile from a light gas gun may be predicted by considering the forces acting on the projectile as it travels down the barrel. At burst, a shock wave travels toward the projectile, and a series of expansion waves propagate into the chamber section of the gun. The projectile is driven forward by the pressure of the driver gas, which initially varies only as a function of the instantaneous velocity of the projectile, Equation 3.2 [48].

$$\frac{P}{P_{burst}} = \left(1 - \frac{u_{proj}}{a_0 \frac{2}{\gamma - 1}}\right)^{\frac{2\gamma}{\gamma - 1}} \tag{3.2}$$

where u_{proj} is the instantaneous velocity of the projectile, P is the instantaneous pressure, P_{burst}, the burst pressure of the diaphragm, a_0, the sound speed of the driver gas, and γ, the specific heat ratio of the driver gas. This relation is accurate until the expansion waves created at burst reflect from the rear of the chamber and

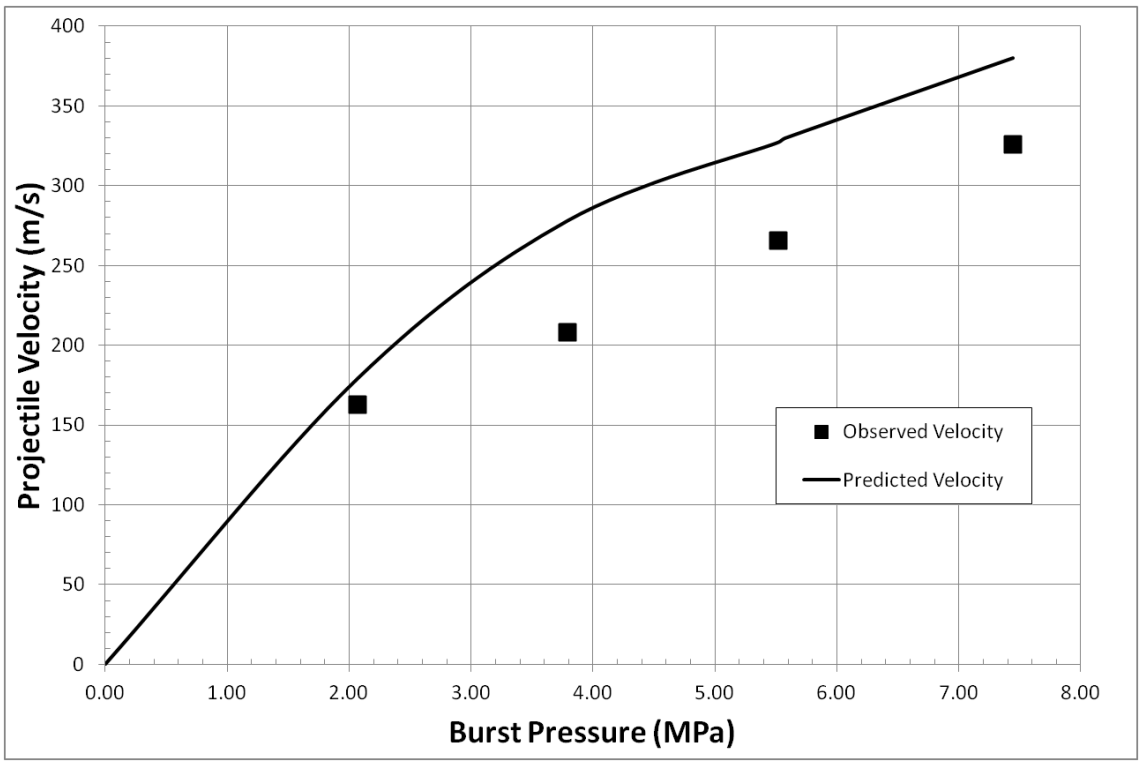

Figure 3.6: A plot comparing the velocity of a 50 g projectile as predicted by Equation 3.3, assuming an effectively infinite chamber and neglecting friction, to experimentally measured velocities. While Equation 3.3 consistently over-predicts the projectile velocity by about 10%, it may still be used as a rough guide for experimental design.

catch up to the projectile. If the projectile exits the barrel before this occurs the chamber of the gun may be considered infinitely long, since no information about the end condition of the chamber reaches the projectile. Exact prediction of the projectile velocity for a light gas gun with a finite chamber length requires a more complex method-of-characteristics solution, as outlined by A. E. Seigel [48].

Combining Equation 3.2 with Newton's law for the projectile yields the following implicit equation for the velocity of a projectile fired from a gun with an effectively infinite chamber length, equation (3.3) [48]:

$$\frac{P_{burst}AL}{Ma_0^2} = \frac{2}{\gamma+1}\left\{\frac{\frac{2}{\gamma-1} - \frac{\gamma+1}{\gamma-1}\left(1 - \frac{u_{inf}(\gamma-1)}{2a_0}\right)}{\left(1 - \frac{u_{inf}(\gamma-1)}{2a_0}\right)^{\frac{\gamma+1}{\gamma-1}}} + 1\right\} \tag{3.3}$$

where A is the the cross-sectional area of the projectile, L, the barrel length, M, the mass of the projectile, and u_{inf} the velocity of the projectile. Figure 3.6 compares the infinite chamber velocity prediction of Equation 3.3 with experimentally measured velocites across a range of burst pressures (1.8–8 MPa) and projectile masses (50–80 g). While Equation 3.3 is shown to over-predict the projectile velocity in all cases, it still functions as a rough guide for use in designing experiments.

A sample tray is rigidly attached to the barrel to ensure proper alignment of the sample with the projectile trajectory. Before firing, samples are affixed to the sample tray with a thin layer of cyanoacrylate glue (Loctite 401). This prevents the sample from moving due to air flow induced ahead oof the projectile by its motion down the barrel. Cyanoacrylate glue is ideal for this application because of its low shear strength ($< 50kPa$ [49]) which allows the sample to easily break free upon projectile impact. After impact, the sample and projectile are captured by a 55 gallon steel drum filled with sand. Projectiles are often undamaged, and, are re-used after tests at low burst pressures ($P_{burst} < 2MPa$), while tests at higher pressures lead to plastic deformation of the projectile. Deformed projectiles are set aside for re-machining prior to re-use.

3.3 Shock Wave Transmission

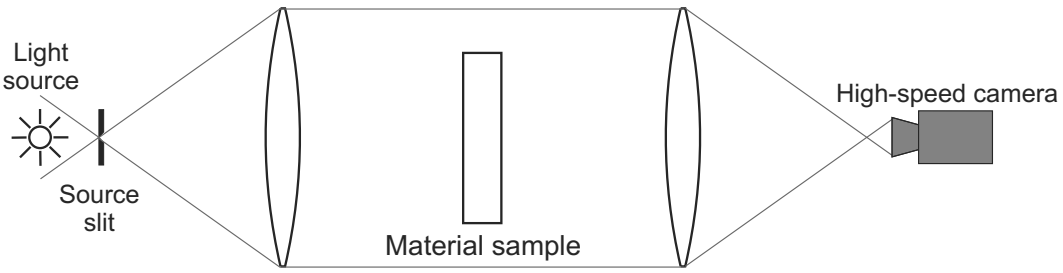

Figure 3.7: A schematic diagram of the shadowgraph system used in this investigation.

The first thrust of this work focused on characterizing the response of candidate blast-absorbing polymers to shock wave loading. Shock and stress wave motion was visualized by a 120 mm, f/10.2, lens-type shadowgraph system with a Photron SA-5 high-speed-digital camera recording at up to 10^6 frames/s (Figure 3.7). Illumination was provided by a 200W continuous white-light Hg-Xenon arc lamp. Wave velocity was measured by tracking the position of the wave front in each frame of the high-speed shadowgram record. Particle velocity was determined by similarly tracking tracer particle motion within the sample and free surface motion as a function of time. Due to the reflection of a "'release wave"' from the free surface of the sample, free surface velocity is not directly equal to U_{p2}. To calculate U_{p2} the 'free surface approximation', equation (3.4) is applied as described in [29]

$$U_{p2} = \frac{U_{fs}}{2} \tag{3.4}$$

where U_{fs} is the measured free surface velocity. This equation accurately describes U_{p2} for a vanishingly-weak shock wave, and approximates the behavior of the stronger shocks seen in this work to within 5%.

3.3.1 Stress Waves

As a preliminary step, shadowgraph wave tracking was performed on stress waves in 25mm x 25mm x 25-60mm rectangular samples of transparent polyurethane (Ultralloy Ultraclear 435) and polycarbonate. Stress waves were initiated in these polymers by an exploding 0.4 mm diameter copper bridge-wire. This exploding bridge-wire (EBW) is rapidly converted to a plasma by a 125 J capacitor discharge. Rapid expansion of this plasma drives a weak shock wave which is coupled to the polymer sample through the surrounding air. Stress waves are relatively weak disturbances and, as such, are not easily visible in the raw shadowgraph images. To increase the visibility of the

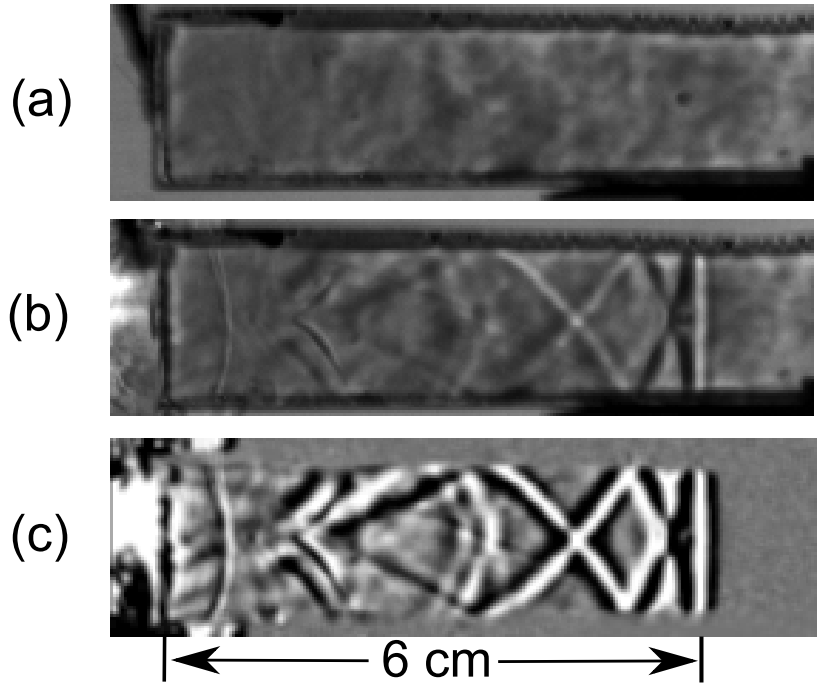

Figure 3.8: 4 x 4 x 30 cm polycarbonate bar, a) pretest, b) raw shadowgram of stress wave, c) same image after processing, wave motion is from left to right.

wave, a digital background subtraction procedure was performed on each image. A pre-test 'tare' image was subtracted from each subsequent image, so that changes from the initial wave-free image were highlighted. Fig. 3.8 demonstrates the results of this process.

The application of a point load produces an initially-spherical wavefront, which becomes completely flat after traveling about 4 times the width of the sample bar (Figure 3.9). This change in shape is the result of a dynamic Saint-Venant effect, similar to those observed by Flynn and Frocht in transparent Bakelite bars [50].

Ultrasonic sound-speed measurements were also performed on the polymers tested here in order to verify bulk sound speed. Measurements of both the longitudinal (c_l) and shear (c_s) sound speeds were performed with 5 MHz transducers in a pitch-catch arrangement. Bulk sound speed (c_b) was then calculated by equation (3.5) from[51].

$$c_b^2 = c_l^2 - \frac{4}{3}c_s^2 \tag{3.5}$$

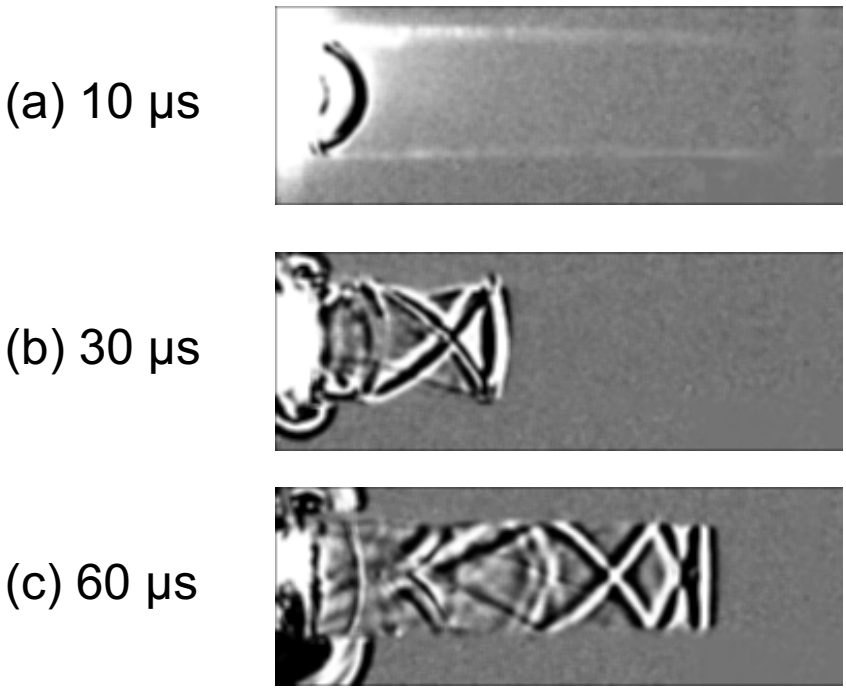

Figure 3.9: Stress wave motion in polycarbonate demonstrating the development of a 1-D planar stress wave from an initial point load. Wave motion is from left to right, and times given are elapsed time after EBW detonation.

3.3.2 Shock Waves

Constant-velocity shock waves were generated in polycarbonate, polyurethane, and polyurea sample plates by ballistic impact. Samples with a 25 x 25 mm cross-section were struck by 25mm diameter 2024-Al cylinders accelerated to velocities of 90–300 m/s by a light gas gun (Figure 3.1). Projectile and sample lengths were chosen to ensure a steady, 1-D shock wave throughout the experiment [30]. This wave initially sets up a 1-D strain condition in the sample, but lateral relief at the sides of the sample (Figure 3.10) lead to the production of an expansion wavefront traveling at the local longitudinal sound speed [52]. Passage of this expansion wave front relieves the state of 1-D strain, and begins a transition to a state of 1-D stress. All present Hugoniot measurements are made on centerline in the period of 1-D strain before this relief occurs, about 5 μs and 7 μs behind the shock wave in polyurethane and polyurea, respectively.

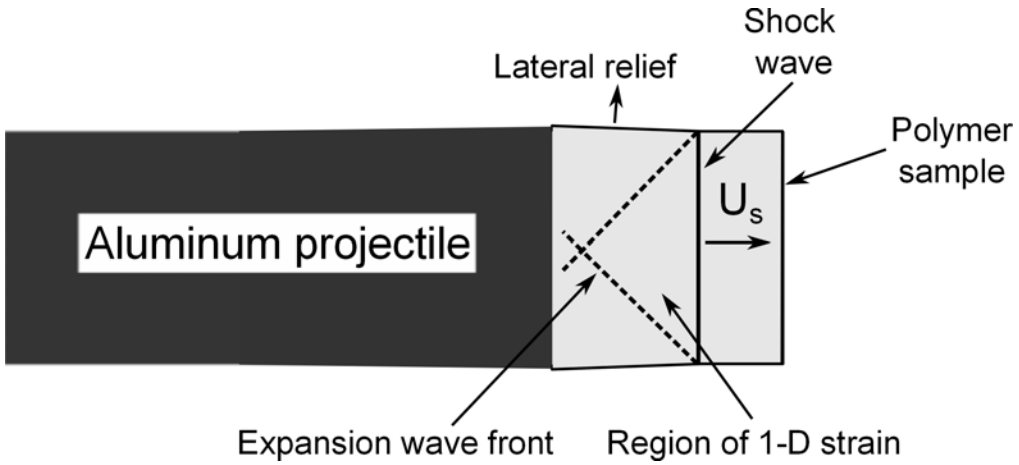

Figure 3.10: Diagram of the lateral relief process after passage of a shock wave. The aluminum projectile moves from left to right. The shock wave in the polymer sample is represented by a solid line, and the first expansion wave from each surface is represented by a dashed line. All Hugoniot measurements in the present work are made in the triangular region of 1-D strain before the arrival of the expansion wave front.

Shock wave velocities were determined optically in transparent samples by tracking the location of the shock wave as a function of time. U_s was measured in opaque and semi-opaque samples by observing the time required to traverse a sample of known length. Particle velocities were optically determined in three ways: First, by tracking the free surface of the sample (u_{fs}) and then applying the free surface approximation (equation (3.4)), second, by tracking the projectile-sample interface, and third by tracking tracer particles (fiducials) in the bulk of the sample.

Decelerating shock waves were next induced in rectangular polyurethane samples by detonating one to two grams of pentaerythritol tetranitrate (PETN), a high-explosive. A 13 mm diameter cylindrical hole was drilled into each polymer sample to the depth required to accommodate the desired amount of powdered PETN at a packing density of 1 ± 0.05 g/cc. This cylinder was filled with PETN and capped with a PETN hemisphere as shown in Figure 3.11. The charge was initiated by an EBW placed between the hemisphere and cylinder (for the details of this initiation method, see ref [53]). The bridgewire and PETN hemisphere were held in place by a few drops

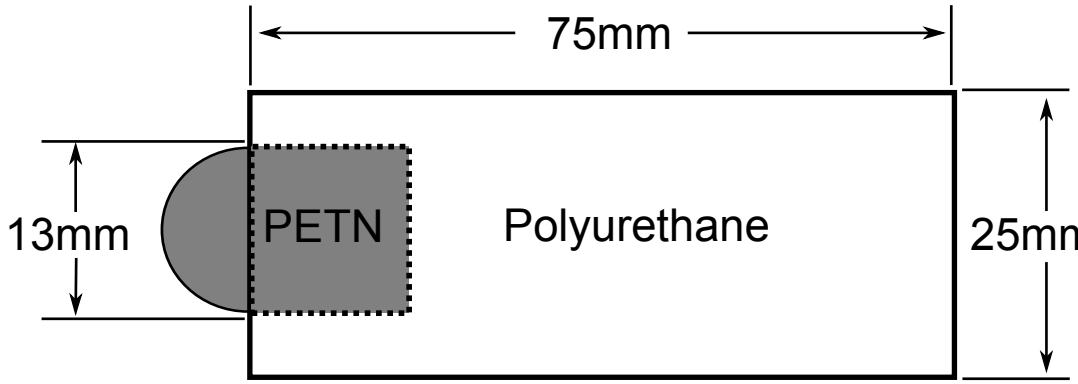

Figure 3.11: Schematic of charge arrangement used to induce decelerating shock waves in polyurethane

of nitrocellulose thinned with acetone to form an "explosive adhesive". The gram-scale explosive charge produces an initially-high pressure and a strong shock wave by direct coupling of the detonation wave into the polymer sample. As the unconfined gaseous explosive products expand after detonation, pressure at the sample surface is quickly reduced. This generates a continuous series of release waves within the sample which, in concert with the effects of viscoelasticity, slow the shock wave as it transits the long rectangular samples used in these experiments. If the sample is transparent, multiple shock- and particle-velocity combinations may be observed in a single experiment.

Shock velocities were measured by tracking the position of the shock front in the high-speed shadowgraph record. Particle velocities were observed by free-surface tracking, as was done in the constant-velocity shock testing, and by tracking the position of internal fiducials. These fiducials were small (diameter $\leq 0.1mm$) air inclusions introduced during the polymer sample plate molding process. As these fiducials were observed through a deformed surface (see Figure 3.10) they were subject to a lens effect, which altered their observed positions. The shape of the optical surfaces of the sample plate was observed to be a wedge of constant slope for an interval of 8–10 μs after the passage of the shock wave. This wedge shape shifts the

observed position of all of the internal fiducials by a constant value, and thus has no effect on the measured particle velocities in this work.

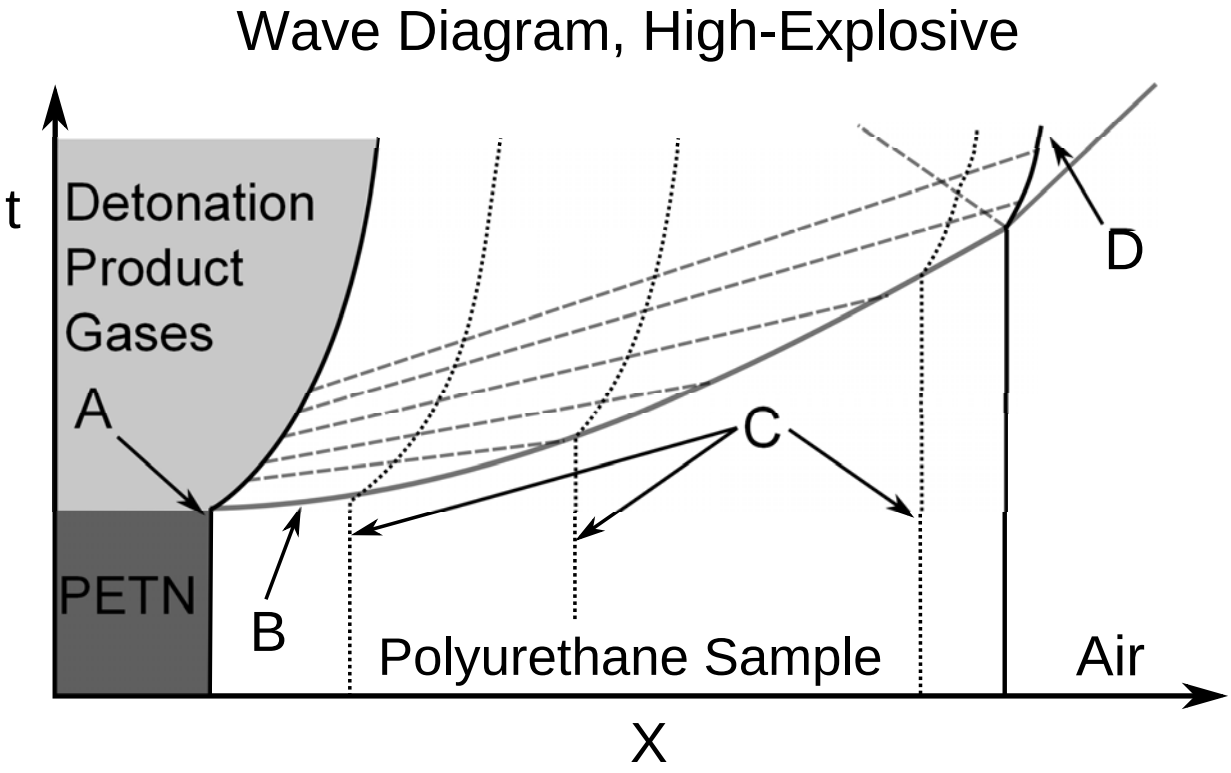

Figure 3.12: (a): Schematic wave diagram of explosively-generated shock motion in polyurethane. A indicates direct light from the detonation of the explosive, B, the primary shock wave, C, a few massless tracer particles, and D, the free surface velocity. Solid lines represent shock waves, and dashed lines represent expansion waves.

3.4 Dynamic Response of Plates Under Blast Loading

The second main thrust of this research was to explore the dynamic response of polymer plates to air-blast loading. Polymer witness plates were clamped in a laboratory-scale 'shock hole' fixture, which was modeled after a full-scale fixture in use at the US Army Aberdeen Proving Ground[1]. These plates were then subjected to air-shock loading from the detonation of 1–1.5 g spherical high-explosive charges. The resulting

[1]The name "'shock hole"' derives from Army tests in which the witness plate was often perforated by a blast. Here, however, the witness plate is never loaded all the way to failure

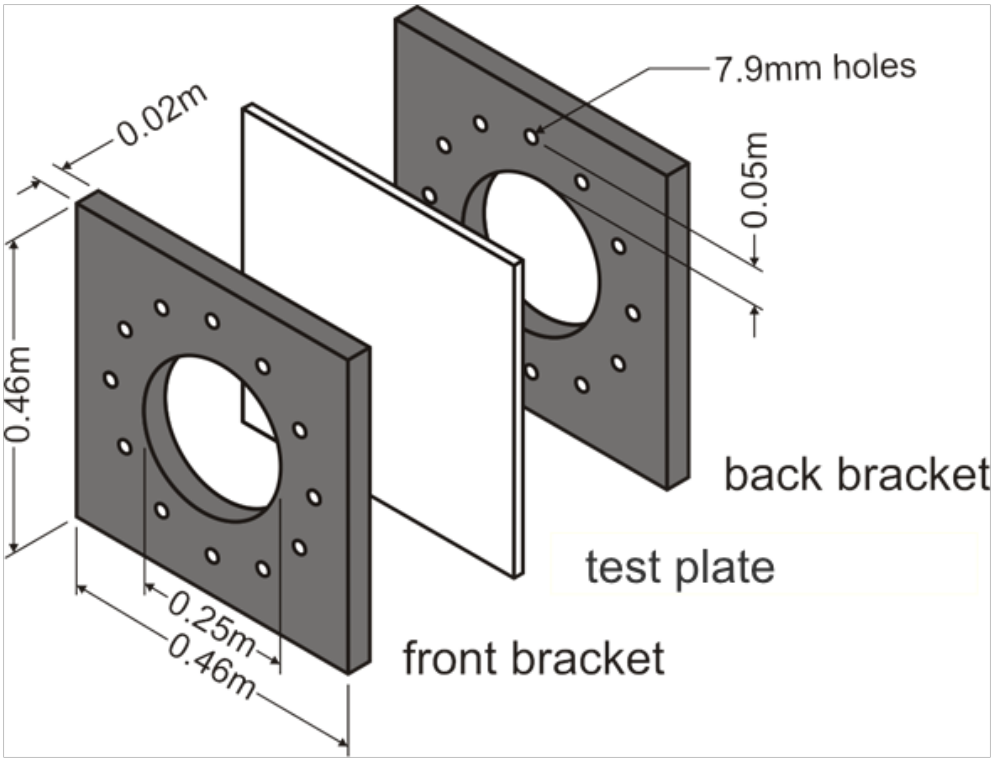

Figure 3.13: Fixture used in plate blast testing

motion of the plate was then observed throughout the event by high-speed videography.

3.4.1 'Shock Hole' Fixture

The shock hole fixture consists of two aluminum plates, 0.46 m square and 0.02 m thick, with a 0.25m diameter hole in the center. A 0.46 m square polymer sample plate is bolted in place between these aluminum plates with 12 symmetrically-arranged bolts (Figure 3.13). This ensures a fully-clamped boundary condition at the edge of the exposed plate, with no measurable slippage.

3.4.2 Optical Deformation Measurement

The motion of the witness plate throughout the test is recorded by two high-speed digital cameras (one Photron SA5 and one Photron SA1.1) in a stereoscopic arrange-

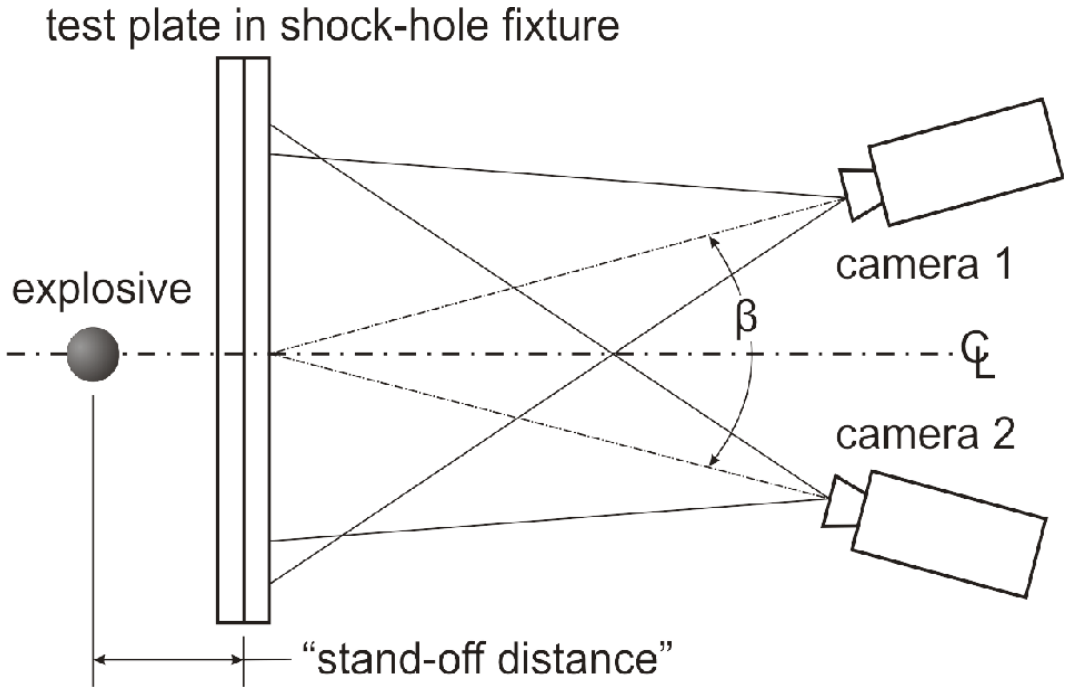

Figure 3.14: Stereoscopic high-speed camera arrangement allowing time-resolved 3-D strain measurement during a shock-hole test

ment as shown in Figure 3.14. The cameras were protected from damage in the event of plate failure by 1-cm-thick polycarbonate shields, not shown. Illumination was provided by a lamp containing an array of 9, 360 W halogen bulbs, also not shown. The surface of the test plate facing the cameras was painted with a high-contrast random speckle pattern, shown in Figure 3.15. The pattern was applied to the plate with matte Krylon spray paints. Each camera recorded data at 50,000 frames per second, and observed a field of view of approximately 0.3 m x 0.12m. By recording at 50,000 FPS the motion of the plate could be tracked without blurring or excessive plate motion between frames. The relatively large field-of-view allowed the experimenter to confirm the symmetry of the plate response.

A commercial software package, VIC 3D by Correlated Solutions Inc., is used to quantitatively measure the deformation of the plate [21]. The software first determines the position of each camera, relative to the shock-hole fixture, with a series of calibration images (Figure 3.16). These images depict a coarse dot pattern of known

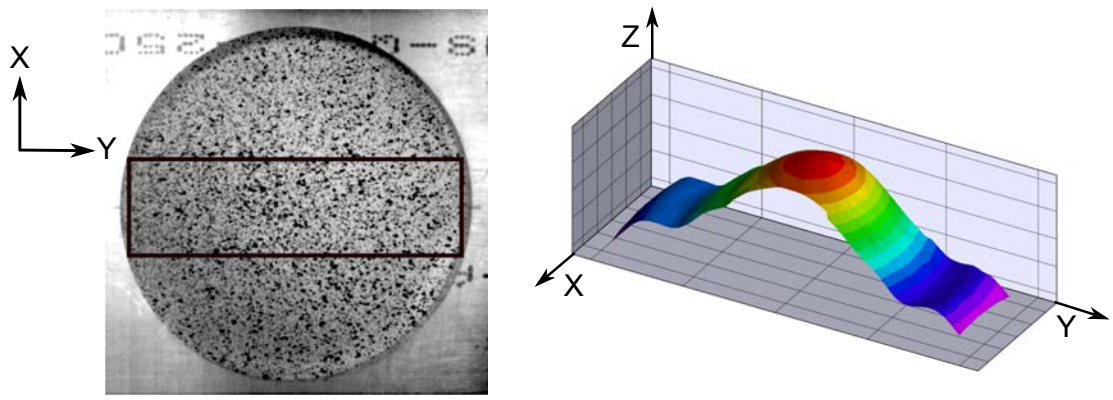

Figure 3.15: Left, witness plate clamped in test fixture, with random speckle pattern for digital image correlation. Black rectangle outlines area of interest. Right, example deformation field obtained in plate blast testing.

size and spacing, held in the field of view of both cameras at a compound angle. At least 20 image pairs with the calibration pattern held at different angles are needed to reliably calibrate the positions of the cameras, though more may be used to reduce error. The VIC 3D package then accepts speckle image pairs of the deformed plate and uses a digital image correlation technique to locate the surface of the plate in 3-D space. The measurement error of this system was evaluated by correlating 50 image pairs of a stationary plate. The maximum error in plate location was found to be less than 0.1 mm. Actual plate deformations observed were, for comparison, up to 23 mm.

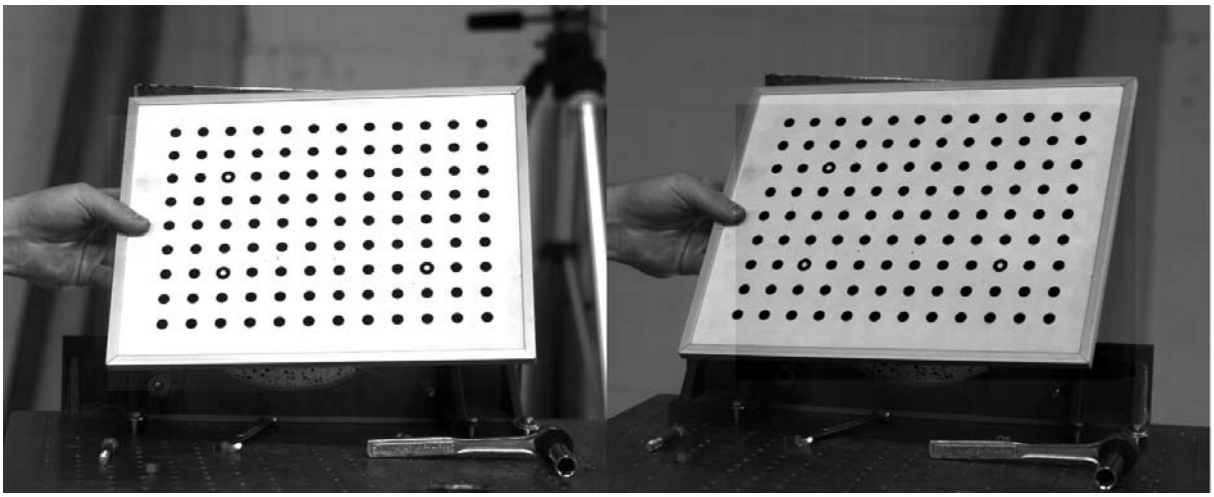

Figure 3.16: Typical pair of images of a calibration target with 25 mm spacing between dots.

4 Results and Discussion

4.1 Stress Wave Imaging

These techniques were initially qualified with exploding-bridge-wire (EBW)-induced stress waves. The EBW applies a relatively small impulse to the sample bar, producing a weak compression wave with $U_{p2} \cong 0$. These waves travel at the longitudinal sound speed in the material[54]. Stress wave speeds were observed in polycarbonate, polyurethane, and polyurea and compared with ultrasonically-measured c_l values. In all cases, the wave speeds measured by shadowgraph wave tracking were found to agree to within 1.5% of those obtained by ultrasonic measurements (Table 4.1). This serves to validate the present optical approach by comparison.

Table 4.1: Longitudinal sound speeds as observed by ultrasound and shadowgraph techniques, all values in m/s.

	Ultrasound	Shadowgraph
Polycarbonate	2189 ± 12	2160 ± 13
Polyurethane	2355 ± 16	2352 ± 3
Polyurea	1699 ± 15	1687 ± 4

4.2 Shock Wave Imaging and the Shock Hugoniot

4.2.1 Constant-Velocity Shock Waves

Constant-Velocity shock waves were induced in polymer samples by ballistic impact. After each shock experiment a pseudo-streak diagram, also known as an x-t diagram, was generated by cropping the same few rows of pixels from each frame of the high-speed shadowgraph record and assembling these vertically in order(Figure 4.1(a)). This allows the entire time history of the quasi-one dimensional wave propagation along the polymer sample to be viewed simultaneously. In this plot, slope represents the inverse of velocity; zero velocity corresponds to a vertical line, with velocity increasing as slope approaches the horizontal. An example ballistic impact experiment on polyurethane is shown in Figure 4.1(b). The ballistic projectile enters from the left and strikes the transparent polyurethane sample, producing the primary shock wave indicated by B. The projectile-sample interface is labeled as A. U_{fs} is measured in the linear portion of the free surface record, C. U_s is obtained by tracking the position of the primary shock as a function of time. U_{p2} in polyurethane samples may be obtained by tracking the projectile-sample interface or through U_{fs} and equation (3.4).

Figure 4.2(a) shows the pseudo-streak diagram for a polyurea sample. Since this sample is not transparent, internal features are not visible. Nevertheless, primary shock transit time can be measured by noting the time of impact, and the appearance of the transmitted shock (indicated by D).

The free surface velocity (C) in polyurea samples was observed to lack the significant linear portion observed in polyurethane tests, making accurate determination of U_{p2} from U_{fs} difficult. Microscopy of the polyurea samples after testing revealed the formation of voids or tears 4-5mm from the free surface of the sample, visible in Figure 4.3. This effect was not observed in the polyurethane samples. It is likely that

these voids are created by release waves reflected from free surface of the sample. The interaction of these waves produces a transient region of high tensile stress, leading to localized void production. The formation and collapse of these voids leads to the observed more complex motion of the free surface. This process and its interaction with the free surface is shown schematically in Figure 4.2(b), labeled as F.

These voids cannot have any influence on U_{fs} until pressure waves produced by their expansion reach the free surface. An estimate of the travel time for a pressure wave from the area of void formation to the free surface was made by assuming the pressure waves travel at c_l. This gives a result of approximately 2.35 x 10^{-6}s. At least two frames, or 2 x 10^{-6}s, are required to perform a velocity measurement. Therefore, a valid U_{fs} may be recorded before material failure influences the result, however, due to the fact that the event time is very close to the temporal resolution of the camera, the error bar associated with this measurement is very high (+/- 25 m/s). These polyurea experiments were then repeated with halogen front-lighting to reveal the projectile–sample interface. Since this interface is far from the voids, its velocity is unaffected by them for the duration of the test. Tracking the projectile–sample interface proved to be a more precise method of measuring U_{p2}, with error bars of 1–5 m/s.

4.2.2 Decelerating Shock Waves

Decelerating shock waves were induced in transparent polyurethane samples by detonating 1–2 g of a high-explosive (PETN) embedded in the sample, as shown in Figure 3.11. Detonation of the high-explosive produces an initially high pressure, driving a strong shock into the sample. The peak pressure applied to the sample may be estimated *a priori* from the detonation parameters of the high-explosive used and the packing density of the charge. In this work, the PETN explosive was packed to

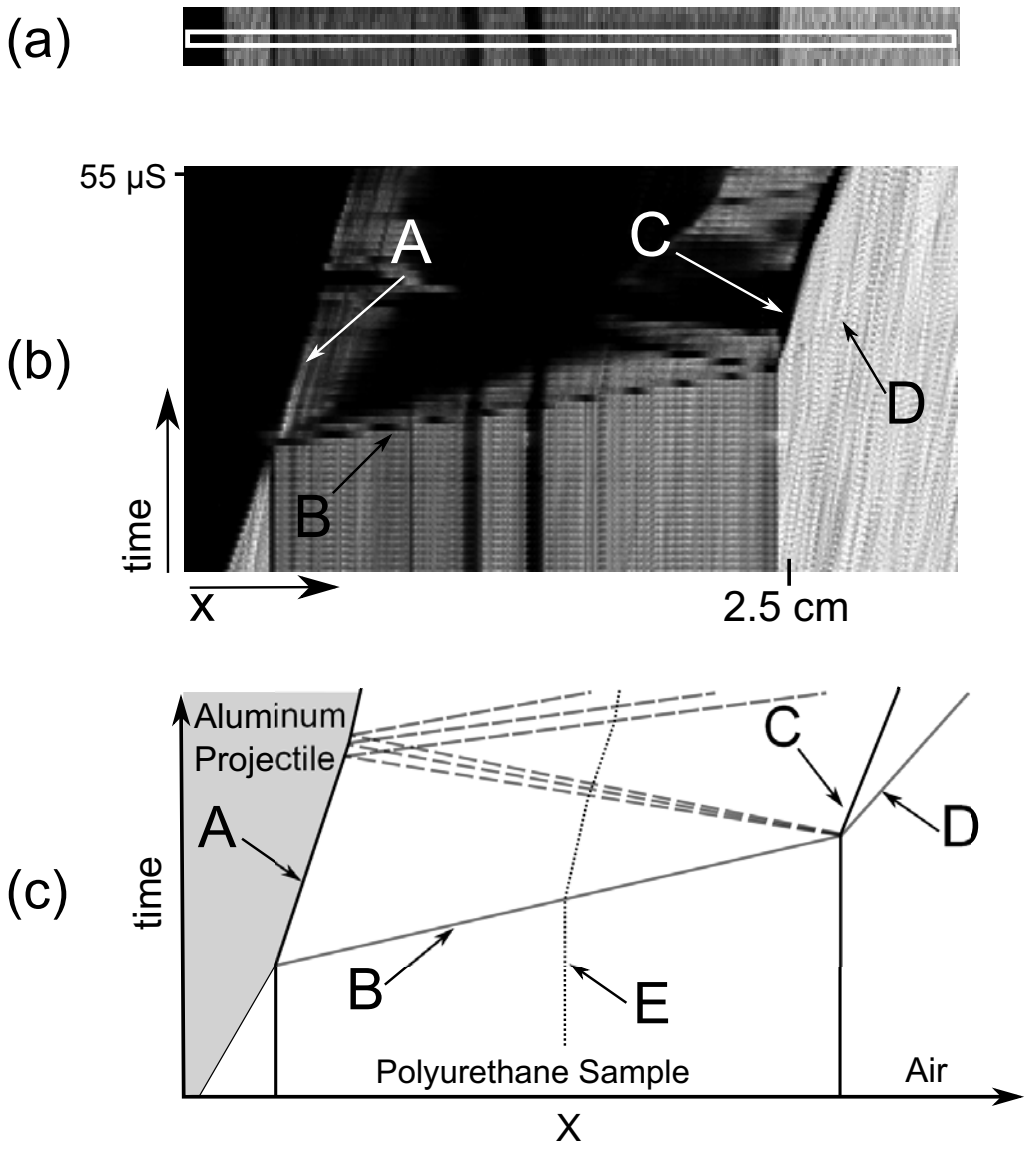

Figure 4.1: (a): Raw frame from the high-speed shadowgraph record, with cropped area bounded in white. (b): Streak diagram of a ballistic impact experiment in polyurethane, assembled from a temporal series of cropped images. The ballistic projectile enters from the left, striking the sample and producing a shock wave. The projectile-sample interface is indicated by A, and the primary shock is labeled as B. U_{fs} is measured in the linear portion of the free surface record, C. An air shock transmitted through the sample is labeled as D. (c): Wave diagram of the test shown in (b). Features are labeled as in (b), with the addition of a massless tracer particle, E. Solid lines represent shock waves, and dashed lines represent expansion waves.

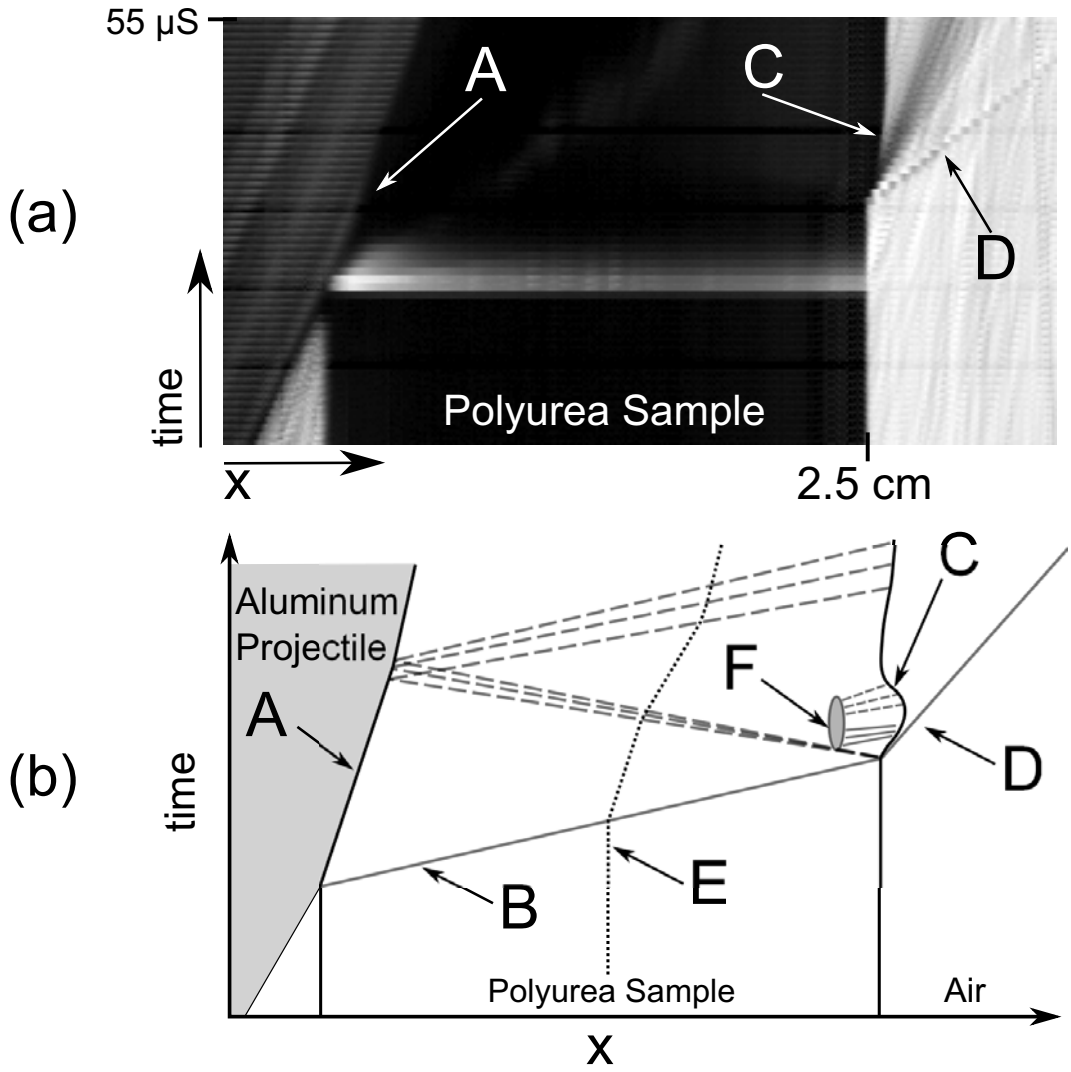

Figure 4.2: (a):Shadowgraph streak diagram of ballistic impact test in an opaque polyurea. Production of voids by the reflected rarefaction complicates motion of the free surface, C. U_{p2} is, instead, measured at the projectile–sample interface, A, to avoid this phenomena. D indicates the shock wave transmitted through the sample into the air. (b):Wave diagram of the test shown in (a). Features are labeled as in (a), with the addition of the primary shock, B, a massless tracer particle, E, and area of void formation/collapse, F. Solid lines represent shock waves, and dashed lines represent expansion waves.

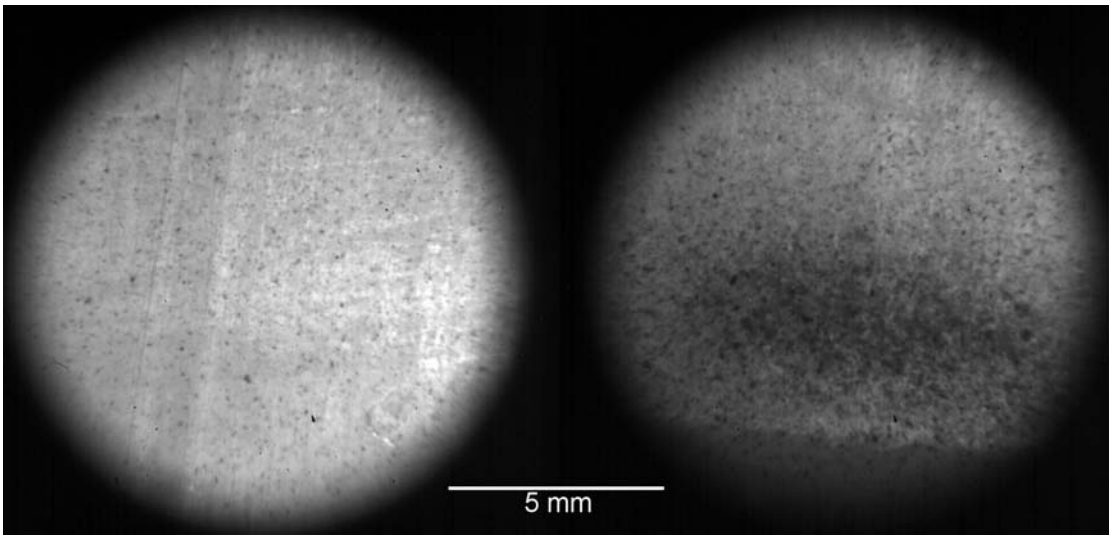

Figure 4.3: Micrographs, left, untested polyurea; right, polyurea with voids formed by tensile stress after shock wave reflection.

1 g/cc, which resulted in a peak pressure of 9.3 GPa [55]. By varying the packing density of PETN, this peak pressure could be varied from 4 GPa up to 30 GPa [55].

The rate at which the shock wave decelerates is controlled by the pressure-time profile at the interface between the explosive and sample, shown in Figure 4.4. This profile can be modified by changing the thickness of the high-explosive charge, the confinement of the gaseous products of detonation or both. Thicker high-explosive charges produce greater quantities of product gas, which expand more slowly and thus produce a longer pressure pulse. Radial confinement of the explosive charge will resist the expansion of the product gases, also contributing to a longer pressure pulse [55]. In these experiments, confinement and high-explosive thickness were chosen to allow observation of the shock for $0 \leq U_{p2} \leq 250$ m/s.

Previous efforts utilizing high explosives to generate shock Hugoniot data have required orders of magnitude more explosive than the technique presented here [14, 56]. In comparison the use of a 1–2 g lab-scale explosive charge has several advantages: the test may be more easily observed by delicate instruments, such as optics and

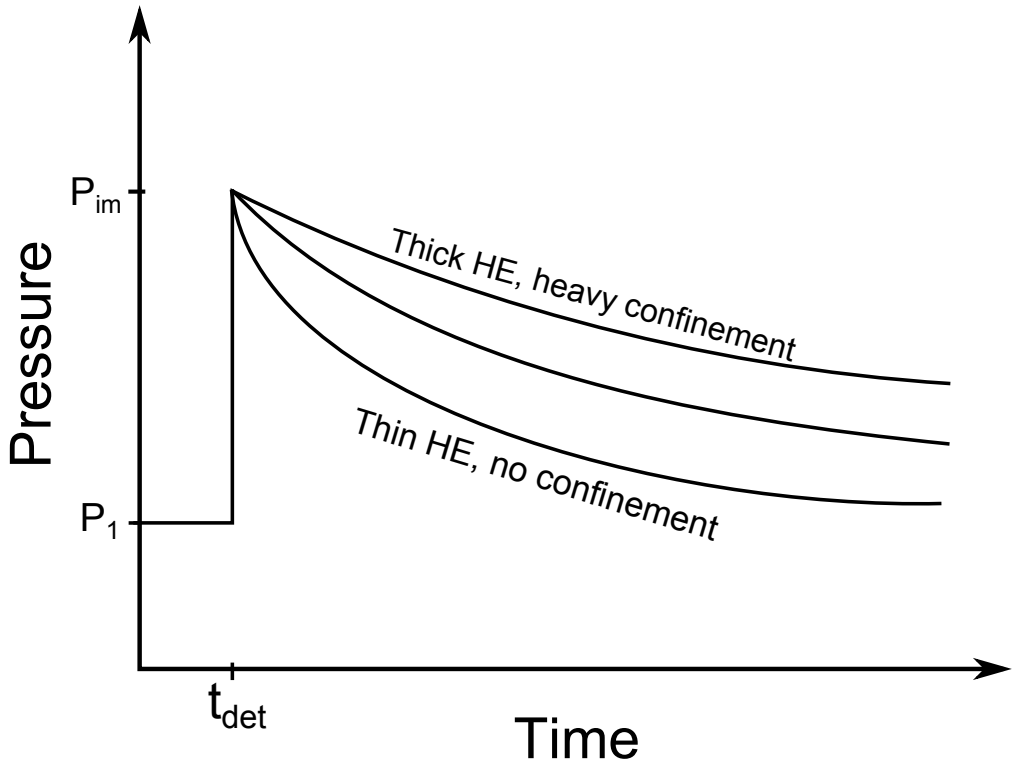

Figure 4.4: Schematic pressure-time plot at the high-explosive–polymer interface [55]. P_1 is the unshocked pressure of the sample, P_{im} is the pressure calculated by impedance matching between the explosive products and the sample, and t_{det} the time of detonation.

high speed cameras, cost is greatly reduced by eliminating the need for a full-sized explosives range or bunker, and risk to the investigators involved is much reduced.

A pseudo-streak diagram of a high-explosive test is shown in Figure 4.5. The white region, indicated by A, is the direct light generated by the detonation of the explosive. The primary shock wave, B, can be seen propagating from left to right. As it passes, bubbles present in the sample, C, are accelerated from rest and act as U_{p2} tracers. The shock then reflects at the far side of the sample, setting the free surface (C) into motion and providing another opportunity to measure U_{p2}. With optical access to the entire sample, the use of a decelerating shock wave allows multiple $U_s - U_{p2}$ combinations to be observed in a single experiment.

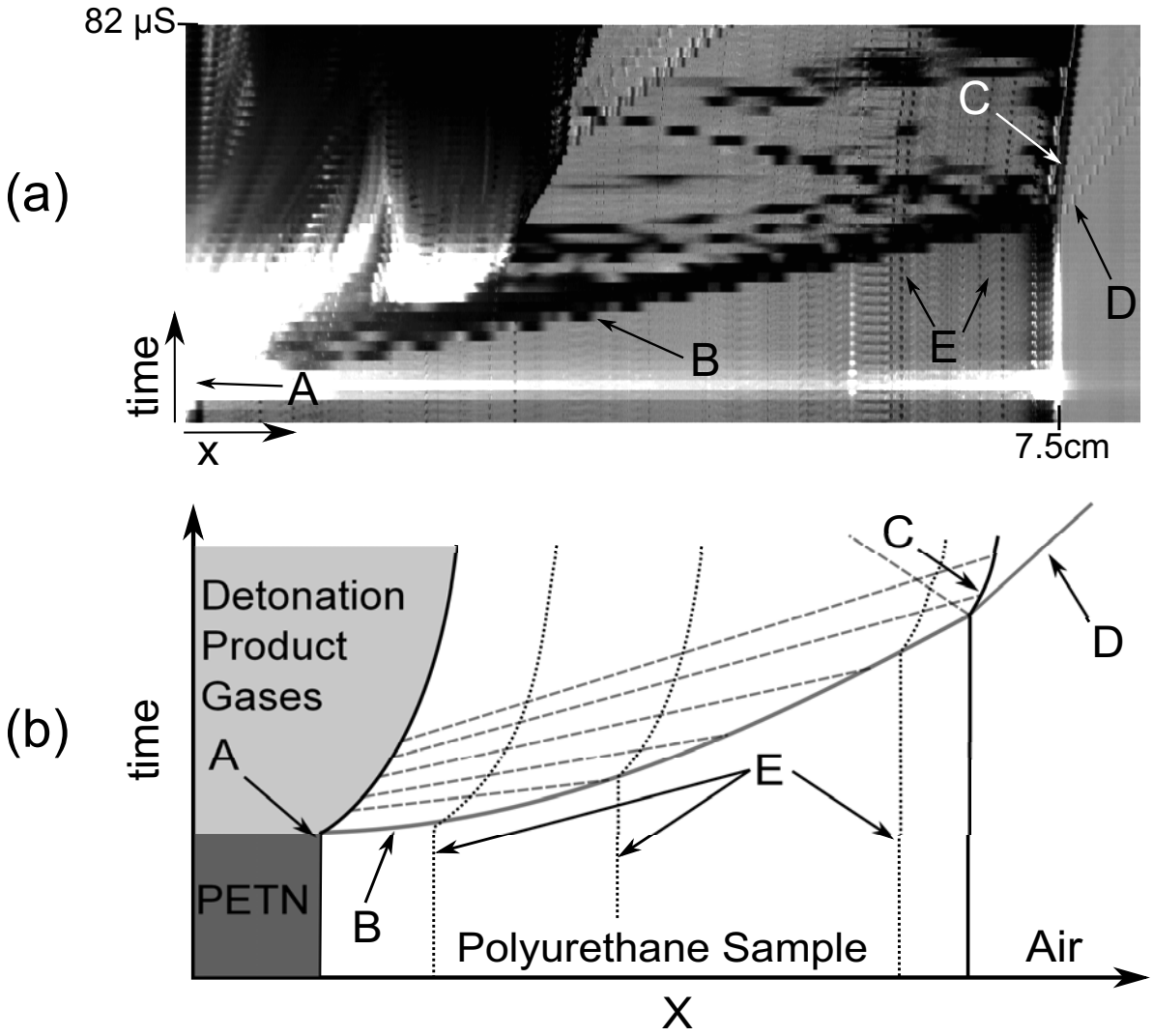

Figure 4.5: (a): Shadowgraph streak diagram of explosively-generated shock motion in polyurethane. A indicates direct light from the detonation of the explosive, B, the primary shock wave, C, the free surface motion , D, the transmitted air shock, and E, a few tracer bubbles. (b): Wave diagram of the test shown in (a), with primary shock curvature exaggerated for clarity. Solid lines represent shock waves, and dashed lines represent expansion waves.

4.2.3 Tracer particle development

Once the tracer concept was shown to work in a sample with a few fortuitously-located air bubbles, work began to develop a more controllable fiducial for the measurement of U_{p2}. Initially, a portion of the reacting polymer was dyed an opaque black and injected with a needle into the bar mold along the centerline. These dye lines revealed the presence of natural convection cells in the reacting polymer. This is not unexpected, since the polymerization reaction is mildly exothermic, and the aluminum mold is a good conductor of heat. Unfortunately, these convection cells moved the dye streaks far from their intended locations, which made placing tracer lines in the measurement region difficult or impossible. Next, 2 x 2 x 30 mm strips of dyed polymer were made and cured separately, then inserted into a bar before it had set up. The locations of these tracers were more controllable, but they still experienced some movement due to the convection cells. Also these strips were rather large, with each one taking up 10% of the field of view in a test. Finally, uniformly seeding the polymer with glass micro-spheres was tried. The micro-spheres used were nominally 150–210μm in diameter, which corresponds to 1.1–1.5 pixels per sphere in the shadowgram image. These glass micro-spheres act as strong lenses, appearing black with a central white dot when in focus, and completely black when out of focus (Figure 4.6). The micro-spheres were added so that nominally 25% of the pixels in the field of view would contain a microsphere, this leads to an addition of 0.7% to the wieght of the bar. Since the spheres are uniformly distributed, convective motion in the bar does not affect the expected seed particle distribution.

4.2.4 Surface Velocity Measurements

The velocity at the surface of the bar is fundamentally different from the velocity in the interior. The interior of the bar experiences a state of 1-D hydrostatic strain, which is critical for measuring a shock Hugoniot. At the surface of the bar, this state

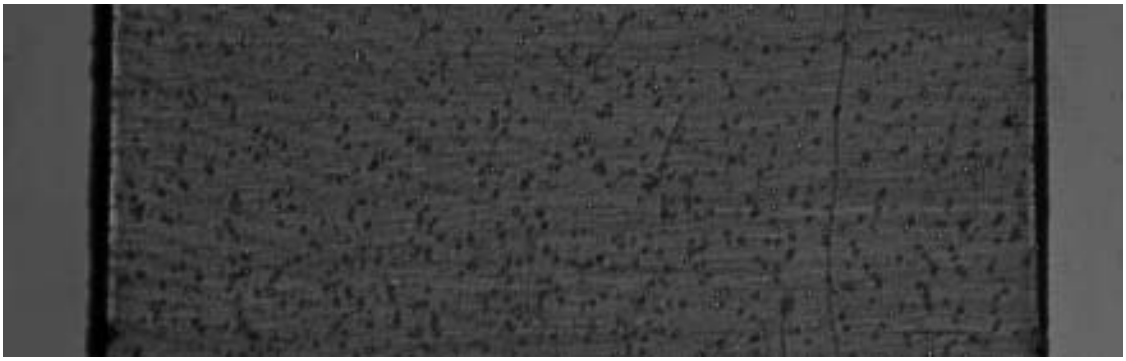

Figure 4.6: Shadowgraph image of glass micro-spheres in polyurethane. Sample width is approximately 20 mm.

of strain is rapidly relieved by lateral expansion of the shocked bar. This expansion deforms the optical surfaces of the bar, possibly deflecting the image of the velocity tracer particles. To determine the effect this has on U_{p2} measurements, it is important to first understand any shape changes of the optical surfaces of the bar during a shock event. Out-of-plane measurements of the surface motion were made by direct observation of the surface with a second high-speed digital camera during several gas-gun experiments. It was found that the optical surfaces do indeed expand laterally, forming a wedge shape of constant angle for 8–10 μs after the passage of the shock wave (Figure 4.7). This wedge causes the light rays passing through the bar to be shifted uniformly in the image plane, but not distorted. This shift was found to be on the order of 0.5 mm for the conditions in this work. Since the deflection of the tracer particle image is constant, it has no effect on the measurement of U_{p2}, and is henceforth ignored.

In addition to measurements of the out-of-plane surface velocity, the in-plane surface velocity was also measured. While this velocity is fundamentally different from the U_{p2} measured on centerline for a Hugoniot point, it can still provide some insight into the behavior of the material under shock loading. The in-plane measurements were made by tracking surface fiduciary marks in transparent samples, and by digital image correlation of a random speckle pattern painted on the surface of the bar

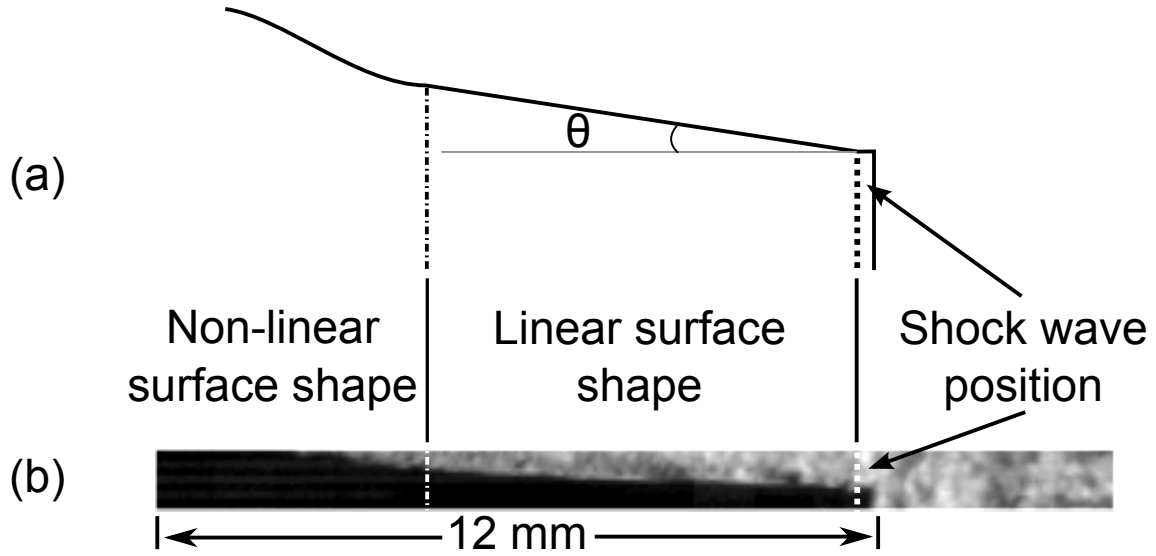

Figure 4.7: (a)Schematic representation of the deformation of the optical surfaces of the bar during a Hugoniot test, with vertical axis exaggerated for clarity. $\theta \approx 2$ degrees in actual testing. (b) Image of the surface deformation of a polyurethane sample during a Hugoniot test. All internal velocity measurements are made during the region of linear surface shape.

(Figure 4.8). A commercial software package (VIC-2D) and a MATLAB code provided by M. Hargather [57] were used to track the in-plane motion of the bar surface. Measurements of both polyurethane and polyurea showed that the in-plane surface velocity reached the central value of U_{p2} only after a significant rise time (Figure 4.9). In polyurethane samples, this rise rime was constant along the length of the bar, with a value of 3 μs. This is consistent with shock rise times in polyurethane measured by laser velocity interferometry by D. Tsukinovsky [33]. In polyurea bars, the rise time was found to increase from an initial value of 8 μs to a final value of 38 μs as the wave transits the bar.

This increase in rise time as a function of distance traveled in polyurea suggests that the material may have a dispersive effect on shock waves. Ballistic impact produces a step increase in pressure at the impact face of the sample, producing an initially sharp shock wave with a very short rise time. The shape of this shock wave is expected to remain relatively constant in materials with no dispersive effects, like the

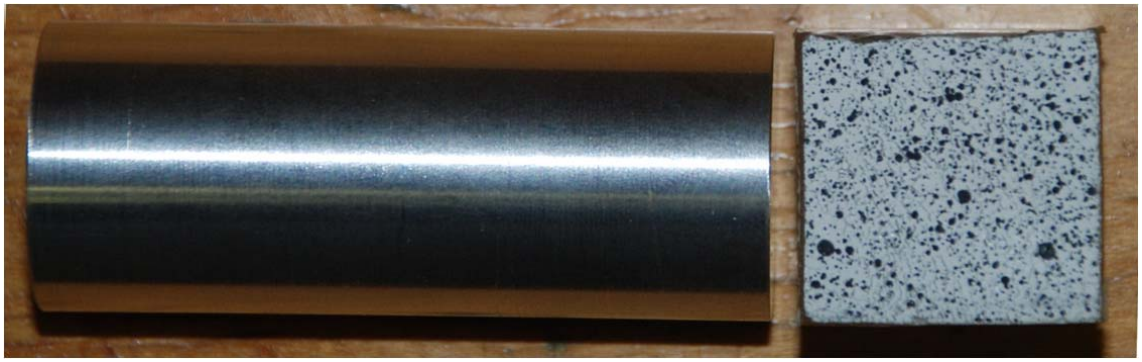

Figure 4.8: Image of a ballistic projectile and a polyurea sample with random speckle pattern for surface velocity measurements.

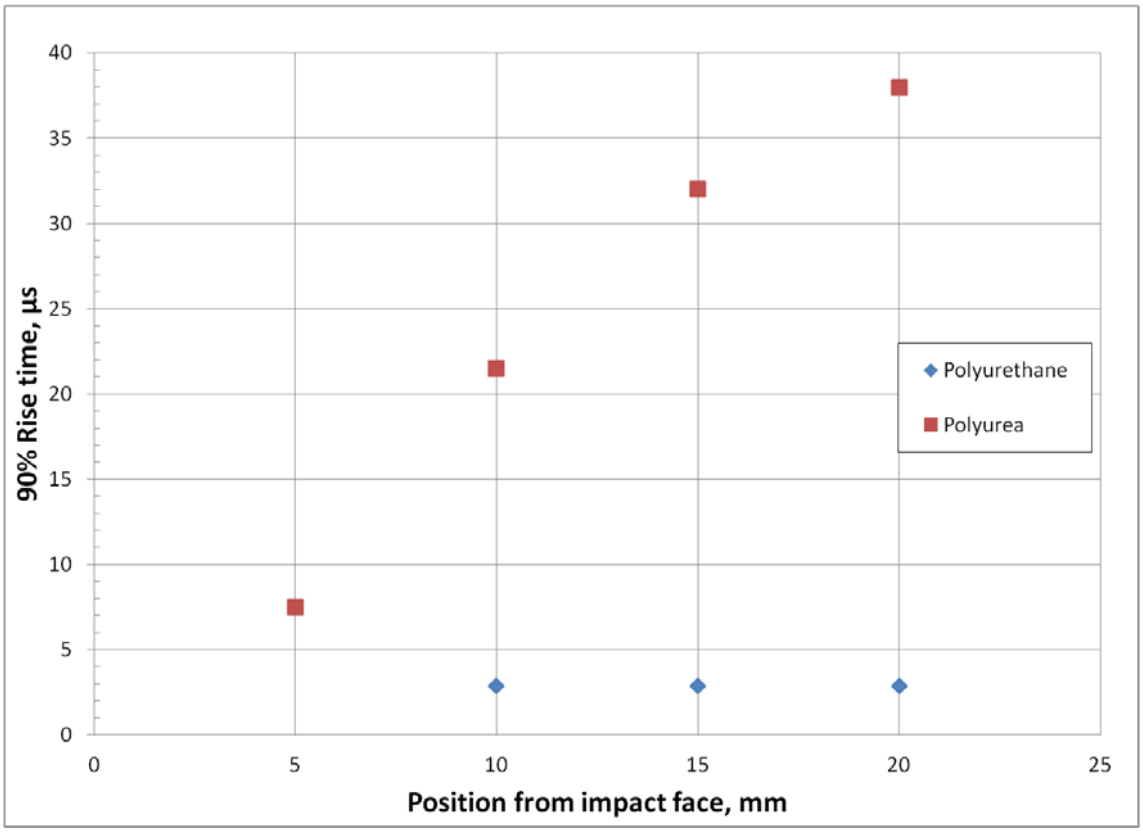

Figure 4.9: Plot of surface velocity rise time as a function of distance traveled in the sample for polyurethane and a P-1000 polyurea.

non-phase-segregated polyurethane tested here. In dispersive materials, however, the initially-sharp shock wave is gradually degraded into an extended series of compression waves, which widens with distance traveled in the dispersive medium. This effect has been observed in many heterogeneous materials, such as dusty He (Miura and Glass [58]), solid mixtures of Ni/Al (Yano and Horie [59]), polycrystalline metals (Horie and Case [60]) and the composite high-explosive PBX (Zhang [61]).

The root cause of the effect is a mismatch in sound speeds between the phases in a heterogeneous material. A schematic diagram of a shock passing through a heterogeneous material is shown in Figure 4.10. The primary phase (in gray) is assumed to have a low sound speed, while the secondary phase is assumed to have a high sound speed. In Figure 4.10a, the shock is sharp, having passed only through the primary phase. The shock has reached the secondary phase in Figure 4.10b. Some of the shock energy is reflected from the secondary phase due to the shock impedance mismatch between the phases, while the rest of the shock energy enters the second phase. Since the sound speed of the second phase is higher, this portion of the shock wave moves faster than the undisturbed shock wave in the primary phase. In Figure 4.10c, the shock wave has exited the secondary phase, while the undisturbed wave in the primary phase lags behind. Due to the impedance mismatch between the two phases, a portion of the shock wave is again reflected, this time as an expansion fan. As the shock wave passes through more and more heterogeneities, it will tend to become more and more spatially dispersed by repetition of this process.

The polyurea used in this work is a phase-segregated polymer, consisting of nano-scale hard domains distributed in a soft matrix. A tapping-mode atomic force microscope image of this polyurea system reveals this phase-segregation and morphology on the nano-scale (Figure 4.11) [46]. If there exists a significant mis-match in sound speeds between the hard phase and the soft phase, shock wave dispersion would be expected. While no direct measurements of the properties of the hard phase in polyurea

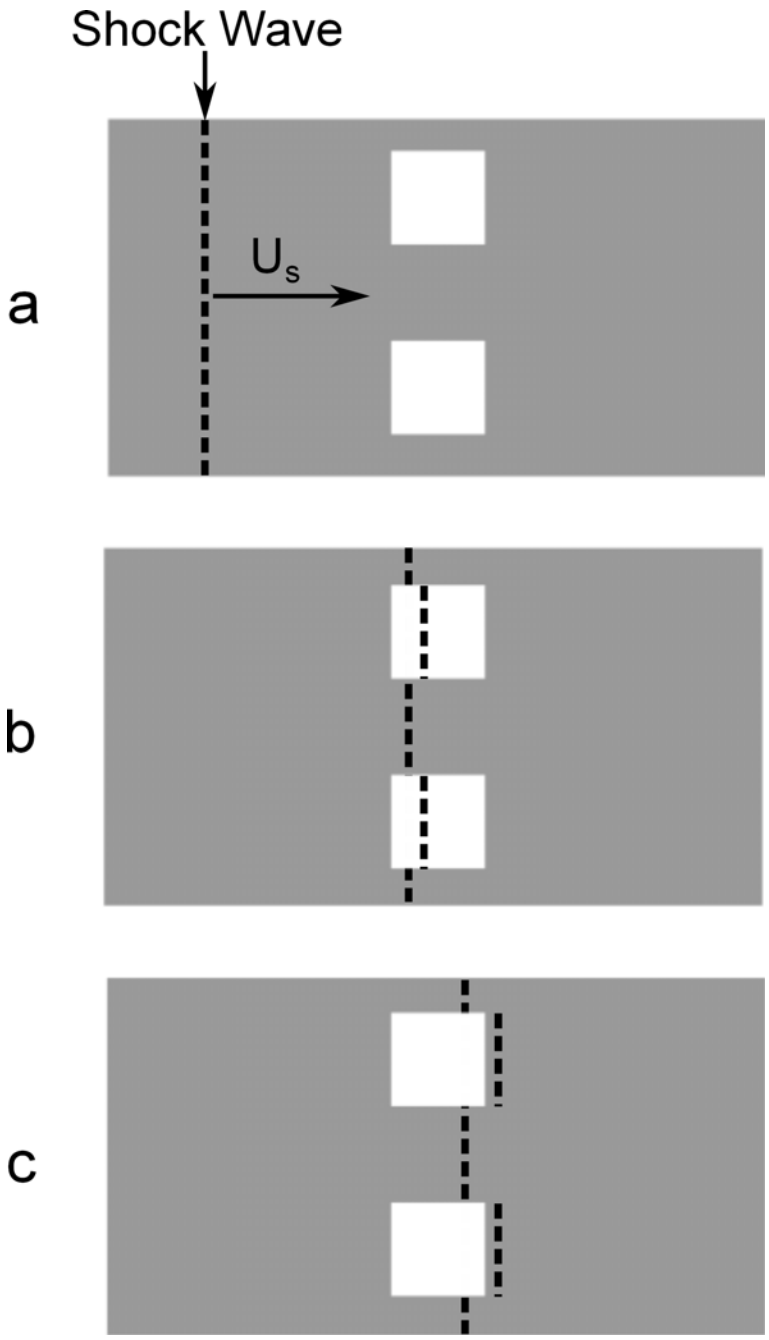

Figure 4.10: Schematic diagram of a shock wave moving through a heterogeneous material. The 'primary' phase with a low sound speed is shown in gray, and the 'secondary' phase with a high sound speed is shown in white. Shock wave reflections are omitted for clarity. Initially, the shock front is smooth and sharp as in (a). As the shock encounters a heterogeneity (b) a portion of the wave front enters the secondary phase. Due to the increased sound speed in the secondary phase, the shock wave travels more quickly, while the shock in the primary phase continues at U_s. After the shock has exited the secondary phase, (c), the shock front is spatially dispersed in the primary phase.

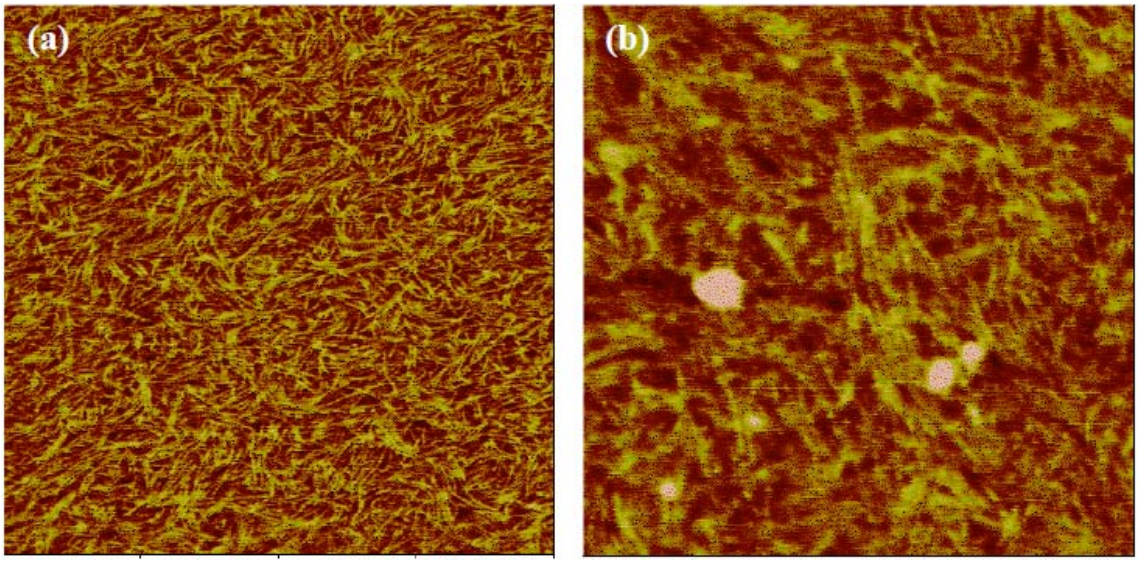

Figure 4.11: Tapping mode atomic force microscopy phase images (scale=5°) of a bulk-polymerized polyurea. (a) a 1x1 micrometer image, (b) a 0.5x0.5 micrometer image showing the ribbon-like, nano-scale hard domains in light orange. [46]

were found in the literature, the expectation is that they will be more stiff than the surrounding soft matrix [62]. The longitudinal sound speed in a solid can be related to the its stiffness (Young's modulus) through the following equation [51]:

$$C_l = \left(\frac{E(1-\nu)}{(\rho(1+\nu)(1-2\nu)} \right)^{1/2} \tag{4.1}$$

where E is Young's modulus, ν is Poisson's ratio, and ρ is the density. As Equation 4.1 shows, sound speed is proportional to the square root of Young's modulus, so a sound speed greater than that of the soft matrix could be expected in the hard domains.

Dispersion of the shock wave by polyurea could be a major reason for the anecdotally-favorable properties of polyurea under blast loading (i.e., the perception that polyurea is an exceptional mitigator of shock energy). Widening of the shock into a series of compression waves would significantly change the character of the blast loading on an object or person protected by polyurea. Instead of experiencing a step increase in pressure, as is the case with a shock wave, the protected object would now experi-

ence a more gradual, ramped rise in pressure. This change in loading character could be especially important in reducing mild traumatic brain injury (mTBI), where the sharp stress gradients associated with a shock wave may cause neurological injury [3]. The shock impedance mismatch between the hard and soft domains also leads to a reduction in shock energy and overpressure, since a portion of the shock energy passing through polyurea is presumably reflected at each soft-domain/hard-domain interface.

4.2.5 Shock Hugoniot Data

The shock Hugoniot data collected herein are shown on the U_s-U_{p2} plane for polyurethane and polyurea in Figures 4.12 and 4.13, respectively. The explosively-generated shock Hugoniot for transparent polyurethane is in good agreement with the ballistic projectile results. These results also agree with an extrapolation of a LANL shock Hugoniot for polyurethane, measured for $659 < U_{p2} < 5078$ m/s [63]. This indicates that polyurethane does not undergo any significant phase changes in the previously unobserved region of $U_{p2} < 250$ m/s.

The significant error band of the decelerating shock results is shown to increase with increasing shock velocity (Fig. 4.12). This is due to temporal resolution limitations of the high-speed camera used in this investigation. As shock speed increases, the wave front moves a greater distance between frames, increasing spatial averaging of the shock speed. To combat this, a faster framing camera or a high-speed streak camera could be used to provide increased temporal resolution. Unfortunately, these resources were unavailable for this investigation.

The shock Hugoniot of the semi-opaque polyureas were also successfully measured. Figure 4.13 shows the (U_s,U_{p2}) results for the hot-cured polyurea. Experiment set 1 was performed without front lighting, with U_{p2} calculated from the free-surface motion (Figure 4.2). Experiment set 2 was performed with front lighting, with U_{p2}

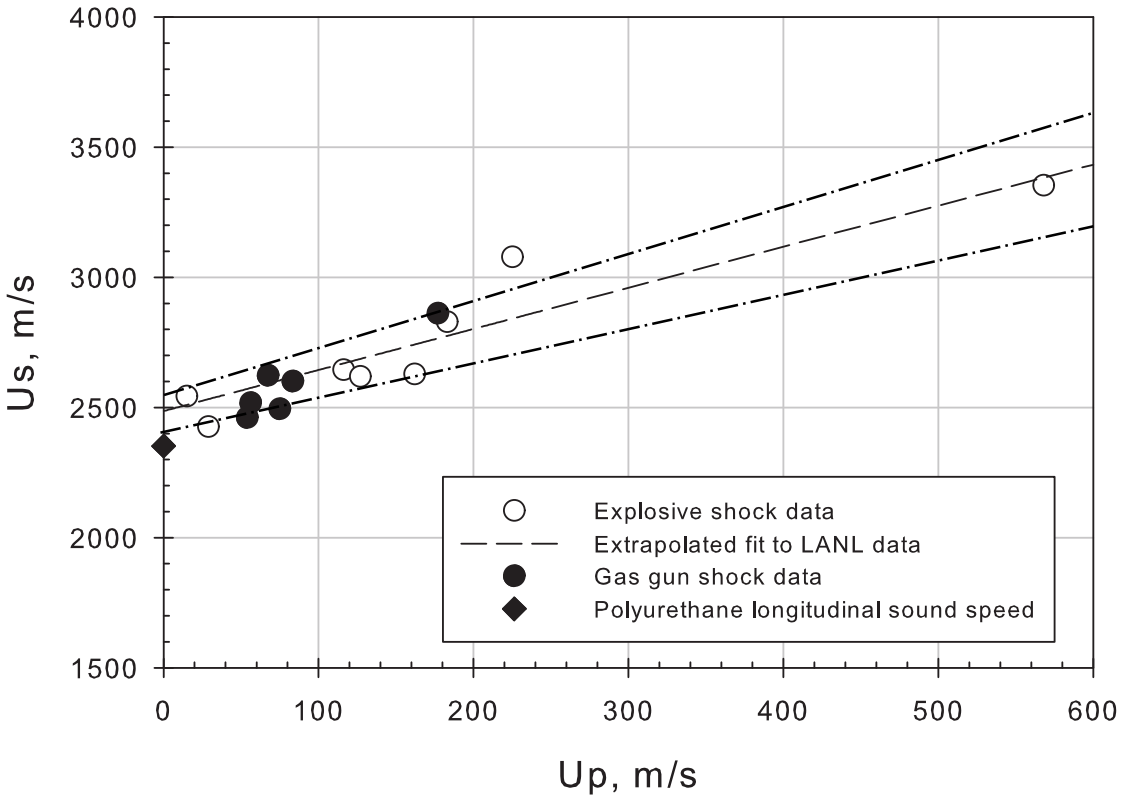

Figure 4.12: Shock Hugoniot data for Polyurethane. Empty circles represent explosively-generated data, with associated error band represented by dot-dot-dash lines. Filled circles represent ballistic projectile data, with sub-symbol-size error. The dashed line represents an extrapolated fit from LANL gas-gun data [55].

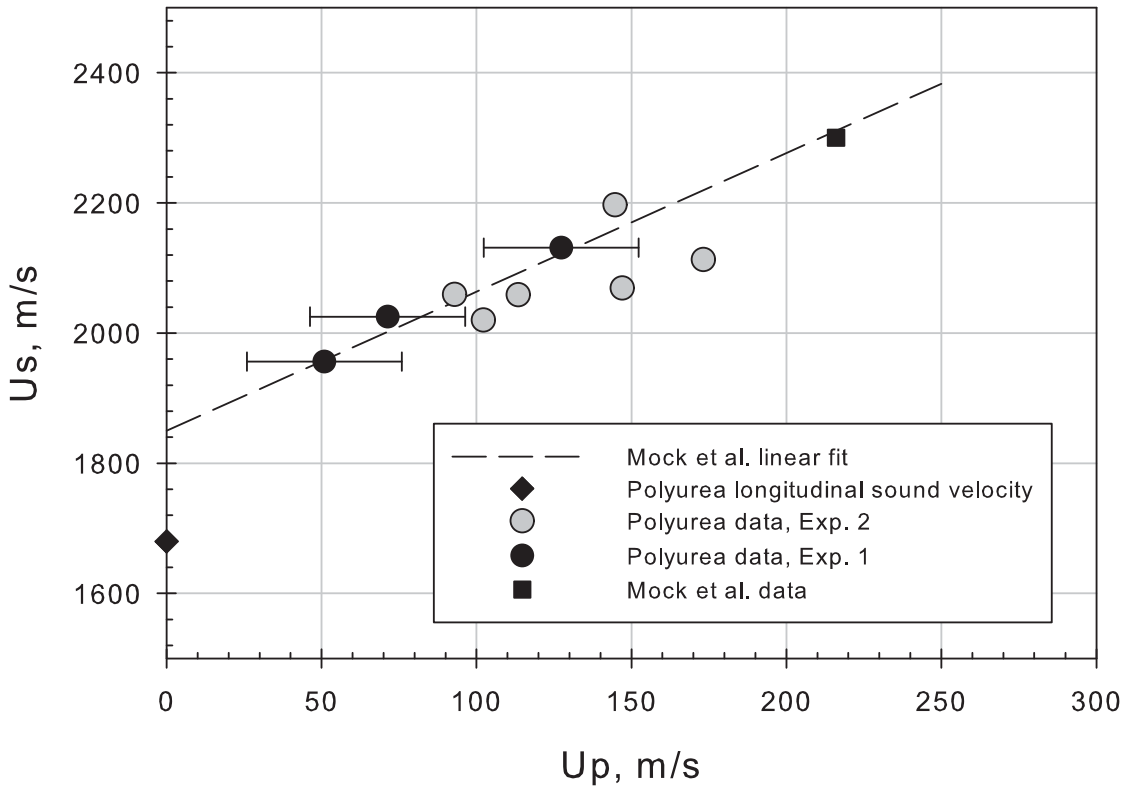

Figure 4.13: Shock Hugoniot data for Polyurea. Black circles represent data from experiment 1, with no front lighting. Gray circle represent data from experiment 2, with front lighting to reduce the measurement error in U_{p2}. Data and a linear fit proposed by Mock et al. are shown for comparison [19].

directly measured at the projectile-sample interface. These different approaches yield essentially-identical results. The measured Hugoniot was also found to be in substantial agreement with an extrapolation of an available Hugoniot for a similar hot-cured polyurea, measured for $216 < U_{p2} < 793$ [19]. The explosively-generated decelerating shock method could not be applied to these samples (represented in Figure 4.13) due to their poor transparency.

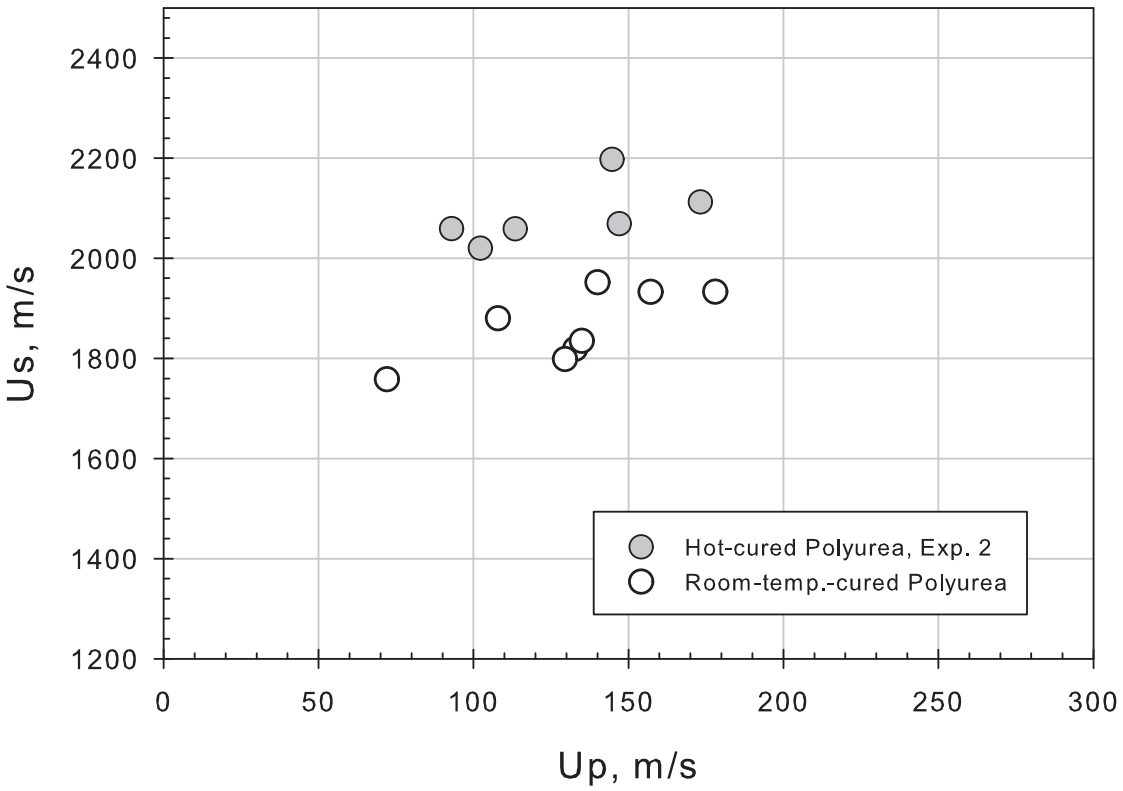

Figure 4.14: Comparison of shock Hugoniot data for room-tempertuare-cured and hot-cured polyurea.

The shock Hugoniot of a polyurea cured at room temperature was also measured, with U_{p2} evaluated at the projectile-sample interface (Figure 4.14). The (U_s,U_{p2}) data for the room-cured polyurea follow a slope similar to the hot-cured material, but with a uniform reduction in U_s of about 200 m/s. This difference may be attributed

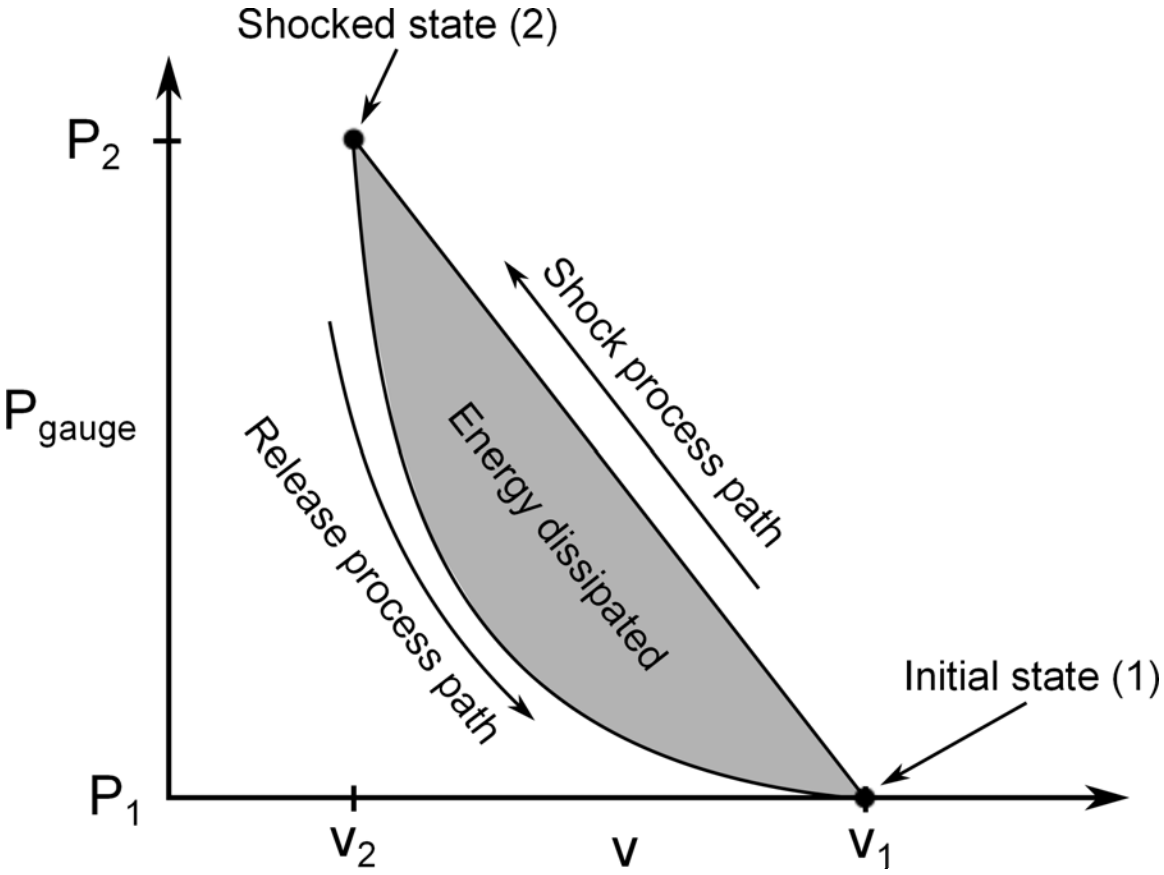

Figure 4.15: Plot of the shock-release cycle on pressure-specific volume coordinates. The material is shocked along the Rayleigh line from state 1-2, and released quasi-isentropically along the Hugoniot curve from 2-1. The area between the curves represents the shock energy dissipated as heat for one shock-release cycle.

to a possible change in the microstructure of the polymer due to the reduced cure temperature.

4.2.6 Energy Dissipation during the Shock-Release Cycle

Using the shock Hugoniot and basic thermodynamics, it is possible to define the amount of shock energy dissipated as heat for a given material under a given shock loading. For a system, the first law of thermodynamics can be expressed as: $dU = \partial Q - \partial W$, where U is the internal energy of the system, and Q and W are the heat and work transfered across the system boundaries, respectively. Figure 4.15 shows schematically the process paths of the shock compression, and the expansion back to

ambient conditions. Shock compression occurs along the Rayleigh line connecting the initial state to the shocked state in P-v space. The shocked material is then released to its initial state by a series of isentropic expansion waves along the shock Hugoniot. From the thermodynamic definition of work, $W_{1-2} = \int_{V_1}^{V_2} PdV$, it can be seen that the compression work done by the shock wave is simply equal to the area under the Rayleigh line from state 1–state 2. Similarly, the work recovered during the release process is equal to the area under the Hugoniot from state 2–state 1. Since more work is put into the system by the shock than is recovered by the expansion waves, there is a net work input to the shocked material over the shock-release cycle. By convention, this leads to a negative value for W_{cycle}. Examination of the first law shows that this net input of shock energy as work can only be converted to thermal energy, which then appears as an increase in temperature (and internal energy, U) that is dissipated to the environment through heat transfer, Q. The actual, quantitative, shock-release cycle is shown in Figure 4.16 for aluminum 2024, and for the polyurethane and polyurea investigated in this work. Polyurea was found to dissipate 1.4–1.8 times more shock energy than polyurethane for particle velocites from 50–250 m/s. Specific dissipation is plotted as a function of shock pressure for aluminum, polyurethane and polyurea in Figure 4.17.

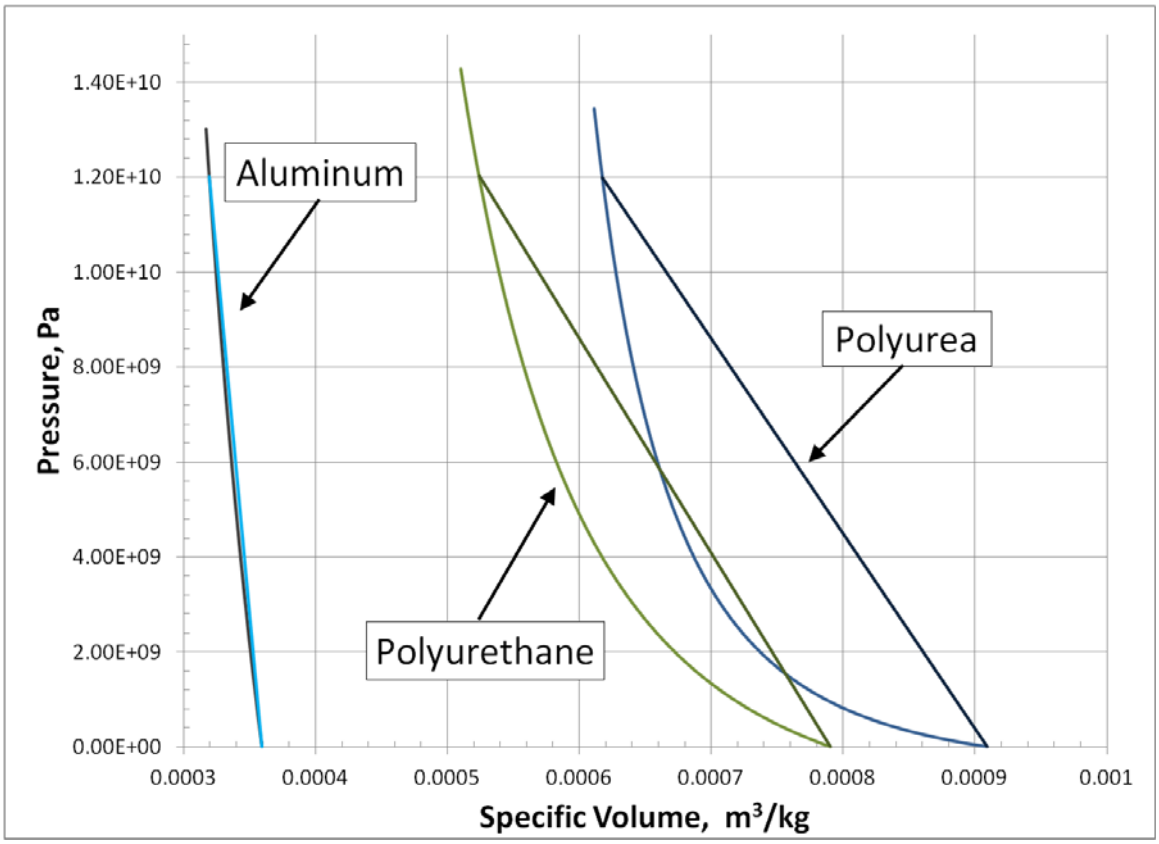

Figure 4.16: Plot of the shock-release cycle for aluminum, polyurethane and polyurea on Pressure-specific volume coordinates. The area between the curves represents the shock energy dissipated as heat for one shock-release cycle. Metals transmit shock waves efficiently, with with very little shock energy dissipated as heat. The two polymers studied here dissipate orders of magnitude more energy in the shock-release process than does aluminum.

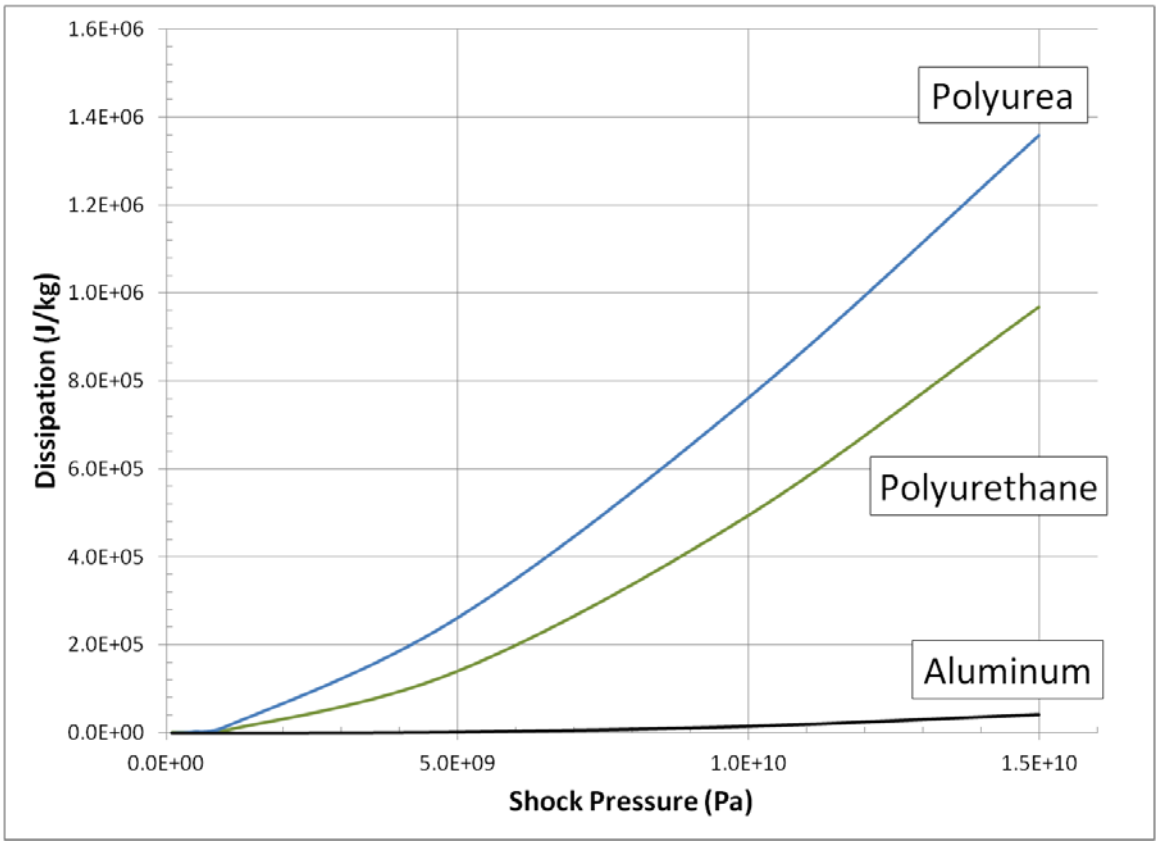

Figure 4.17: Plot of the shock energy dissipated by the shock-release process as a function of shock pressure for aluminum, polyurethane, and polyurea. Polyurea dissipates the most shock energy of these materials, with its advantage increasing with increasing shock pressure.

4.3 Dynamic Response of Plates Under Blast Loading

Polymer witness plates were subjected to air-shock loading from laboratory-scale explosive charges as described in section 3.4. The motion of the plate as a function of time was then recorded using two high-speed digital cameras in a stereoscopic arrangement. This results in a time-resolved 3-D representation of the plate surface throughout the event. Explosive impulse loading was calculated *a priori* as a function of charge mass and stand-off distance.

4.3.1 Blast Loading

The polymer witness plates in this investigation were exposed to explosive shock waves from 0.8–1.5 g PETN charges at stand-off distances of 0.025-0.25 m. The shock-wave-generating properties of PETN as a function of stand-off distance were well-characterized in previous work [64] [38]. The Mach number of the shock wave at the plate surface was calculated from the charge stand-off distance, and the following curve fit to a PETN characterization by Biss and Settles [64]:

$$M(r) = \begin{cases} 0.587402r^{-}0.779107 & : 0.025 \leq r < 0.075 \\ 0.332276r^{-}0.999280 & : 0.075 \leq r < 0.330 \end{cases} \tag{4.2}$$

where M is the shock wave Mach number and r is the distance from the charge to the plate. Shock overpressure as a function of time was calculated from the modified Friedlander equation [65]:

$$P(t) = P_{atm} + P^{+}(1 - \frac{t}{T^{+}})exp(\frac{-\alpha t}{T^{+}}) \tag{4.3}$$

where P_{atm} is the atmospheric pressure, P^{+} is the maximum gage overpressure at the plate surface, t is time, and α is the 'wave form parameter' which prescribes the decay shape of the P(t) curve after P^{+} is reached. The wave form parameter

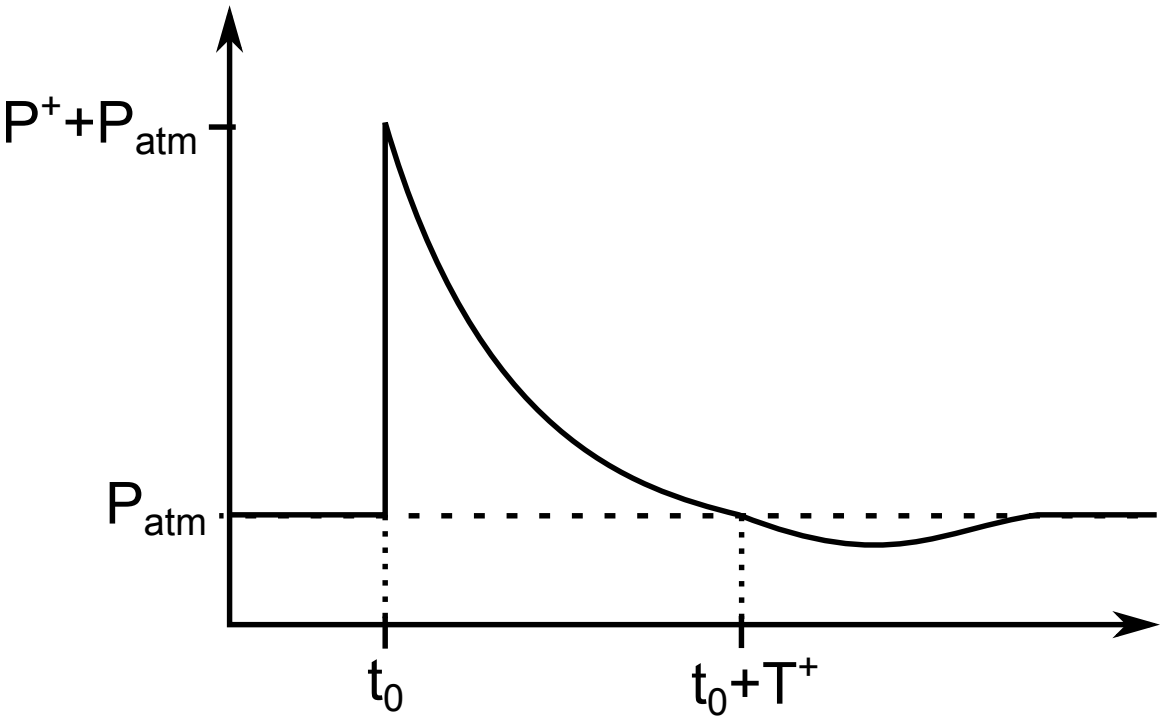

Figure 4.18: Schematic diagram of a typical pressure-time profile associated with an explosive blast wave. P^+ is the gauge overpressure immediately behind the shock wave, t_0 is the arrival time of the shock wave, and T^+ is the positive overpressure duration.

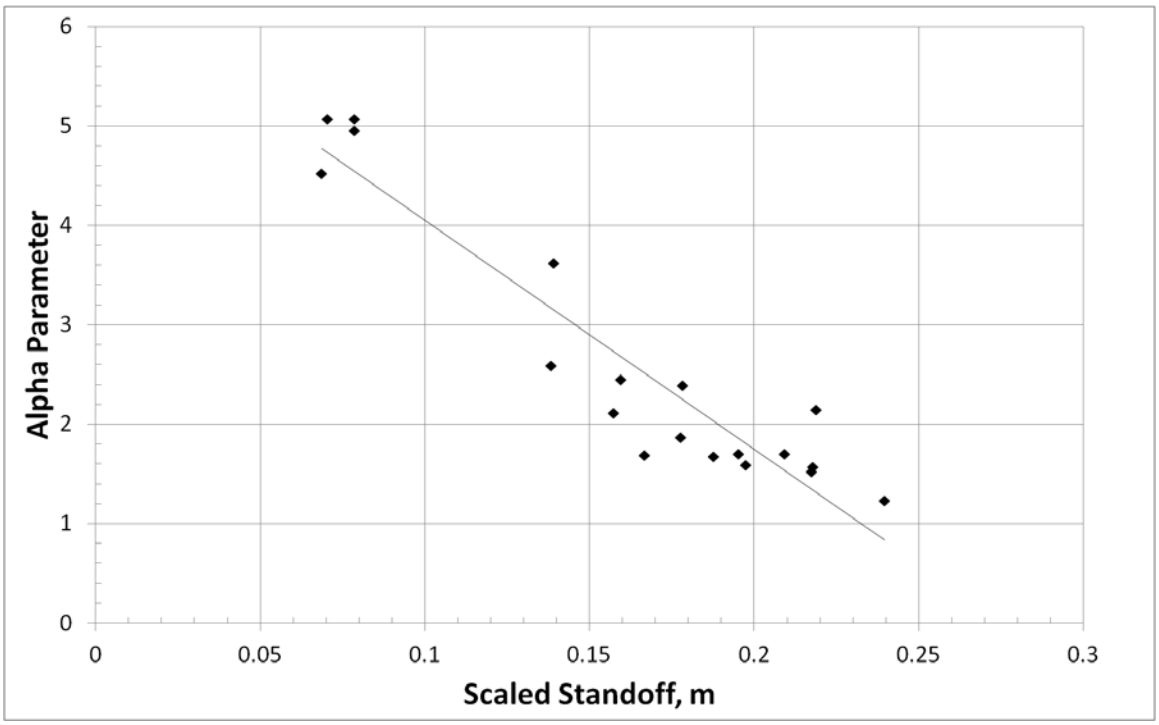

Figure 4.19: Plot of the experimentally measured waveform parameter (α) as a function of scaled charge stand-off, and linear fit to these data (equation 4.4). Pressure traces were measured by Biss [66], and alpha parameters were determined by the present author.

was determined as a function of charge stand-off distance by fitting the modified Friedlander equation to a series of pressure traces recorded by M. Biss [66]. The measured values of α and the resulting fit, equation 4.4, are shown in Figure 4.19.

$$\alpha = -36.64R_s + 9.68 \tag{4.4}$$

All charges used in this work were mathematically scaled to a one-gram standard to determine shock properties. These properties were then scaled back to the actual charge mass as appropriate. Details of this scaling procedure can be found in previous work by Biss and Settles [64]. Knowledge of these shock properties, charge mass, and charge stand-off distance allows the pressure and impulse loading on the plate to be calculated *a priori*. Only the positive overpressure on the plate is considered; the negative phase of the explosive loading is small and generally ignored [38]. At

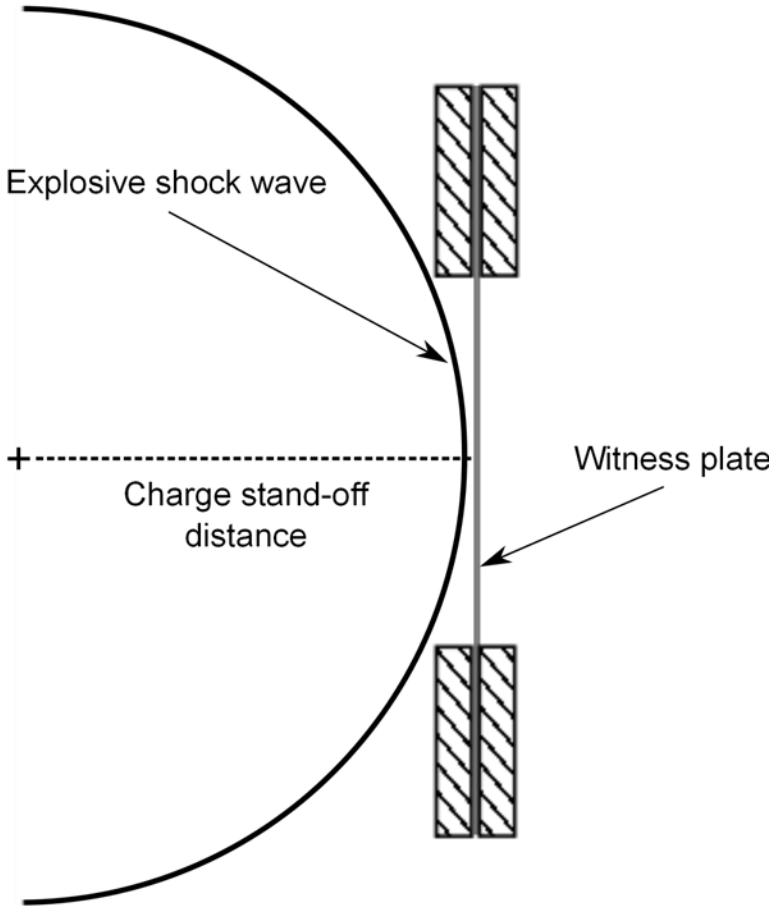

Figure 4.20: Diagram of a spherical shock wave impinging on a plate. At centerline, the shock reflects normally to the surface of the plate, but at all other locations the shock reflects at an oblique angle.

the centerline, the shock is normal to the surface of the plate, and the reflected overpressure can be directly calculated from following equation [67]:

$$\frac{P_{reflected}}{P_{atm}} = \frac{(4M^2 - 1)(7M^2 - 1)}{3(M^2 + 5)} \tag{4.5}$$

where M is the Mach number of the incident shock wave.

At locations away from the center of the plate, the shock wave arrives at an oblique angle to the surface of the plate (Figure 4.20). This results in a reduced reflected overpressure, which can be calculated as outlined in reference [67]. For angles of incidence (β) below 40 degrees, the steady flow counterpart of the oblique reflection

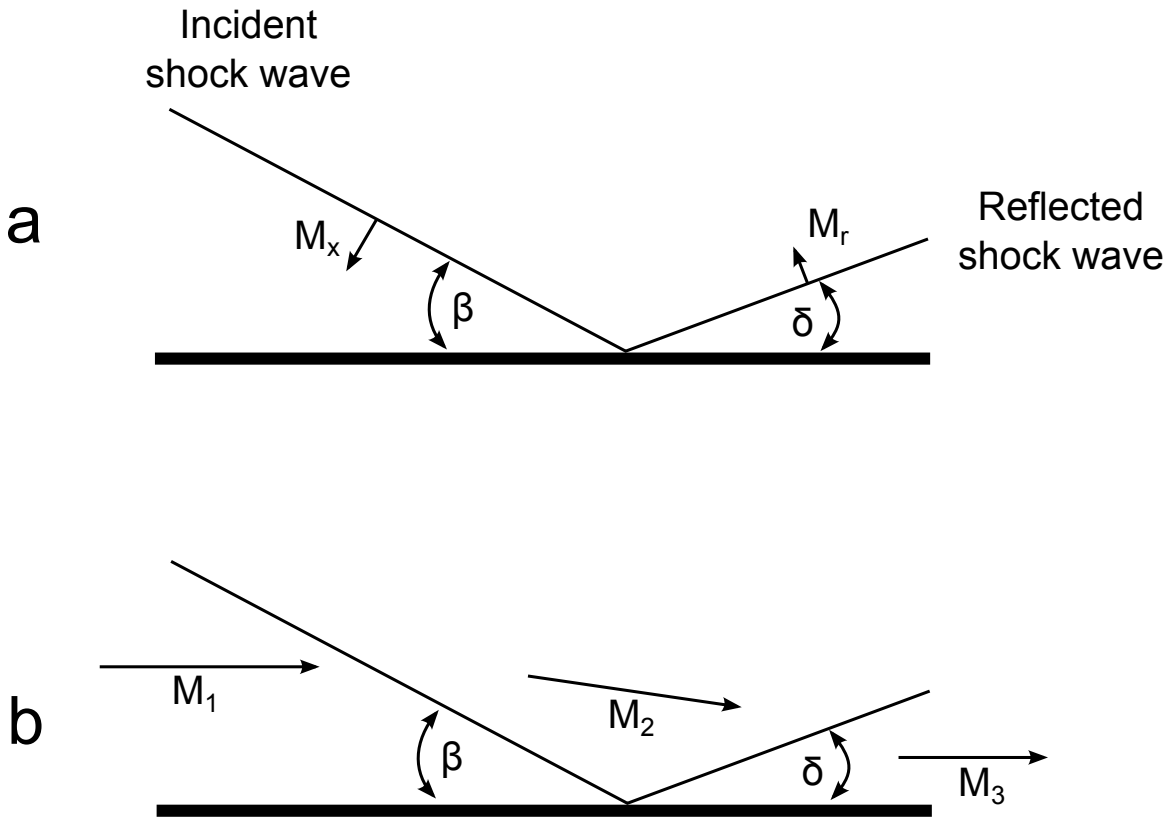

Figure 4.21: Schematic diagram of (a)an oblique shock reflection and (b)its steady flow counterpart.

is constructed (as in Figure 4.21), and the flow properties upstream of the reflected shock are calculated in this coordinate frame by the standard techniques outlined in any compressible gas dynamics text [68]. The angle of the reflected shock (δ) can then be determined graphically using a shock polar diagram, or by the iterative method outlined in Appendix 1. The flow properties are then transformed back to the coordinate frame of the shock reflection, and the maximum reflected overpressure acting on the plate surface is calculated by equation 4.6 [67]:

$$\frac{P_{reflected}}{P_{atm}} = \frac{(7M_r^2 - 1)(7M_x^2 - 1)}{36} \tag{4.6}$$

where M_r is the Mach number of the reflected shock wave, and M_x is the Mach number of the incident shock wave.

When the incident reflection angle of the shock wave is greater than 40 degrees, a Mach reflection occurs (Figure 4.22). The Mach number of this Mach stem can be determined from geometry as in equation 4.7 [67]:

$$M_S = \frac{M_x}{sin(\beta)} \tag{4.7}$$

where M_S is the Mach number of the Mach stem, and β is the angle of incidence of the shock wave. Once the Mach number of the stem is known, its overpressure can be calculated directly by the normal shock relation, equation 4.8 [67]:

$$\frac{P_s}{P_{atm}} = \frac{7M_x^2 - 1}{6} \tag{4.8}$$

A MATLAB script was written to calculate reflected shock overpressure on the plate as a function of time for a given charge mass and standoff, and is included as an appendix to this work. Figures 4.23 and 4.24 show the results of these calculations for a 0.947 g charge at a 12.5 cm stand-off distance.

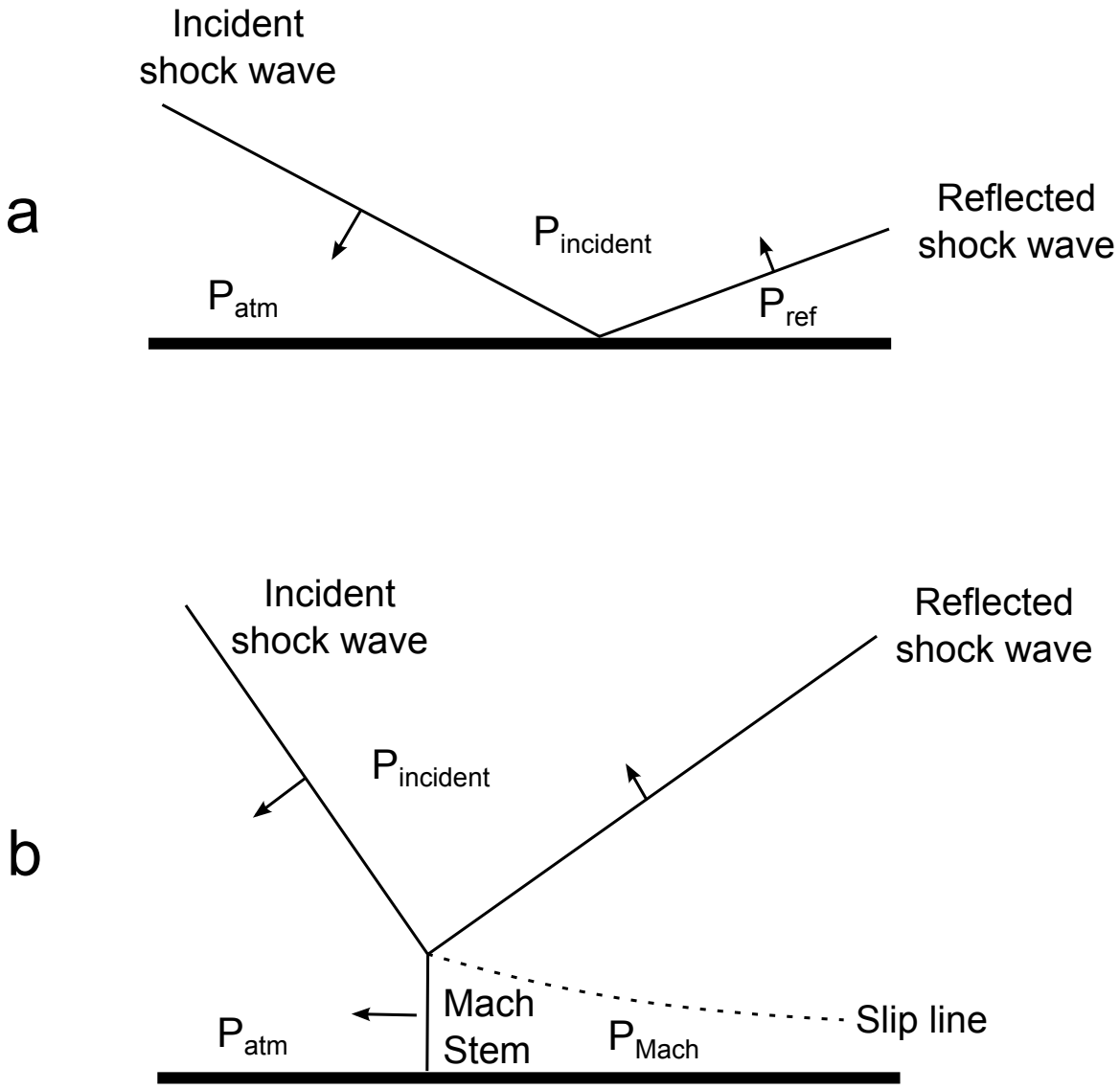

Figure 4.22: (a) Schematic diagram of a regular oblique shock wave reflection. Such a regular reflection occurs for angles of incidence below 40 degrees. (b) Schematic diagram of a Mach reflection, which occurs for angles of incidence greater than 40 degrees.

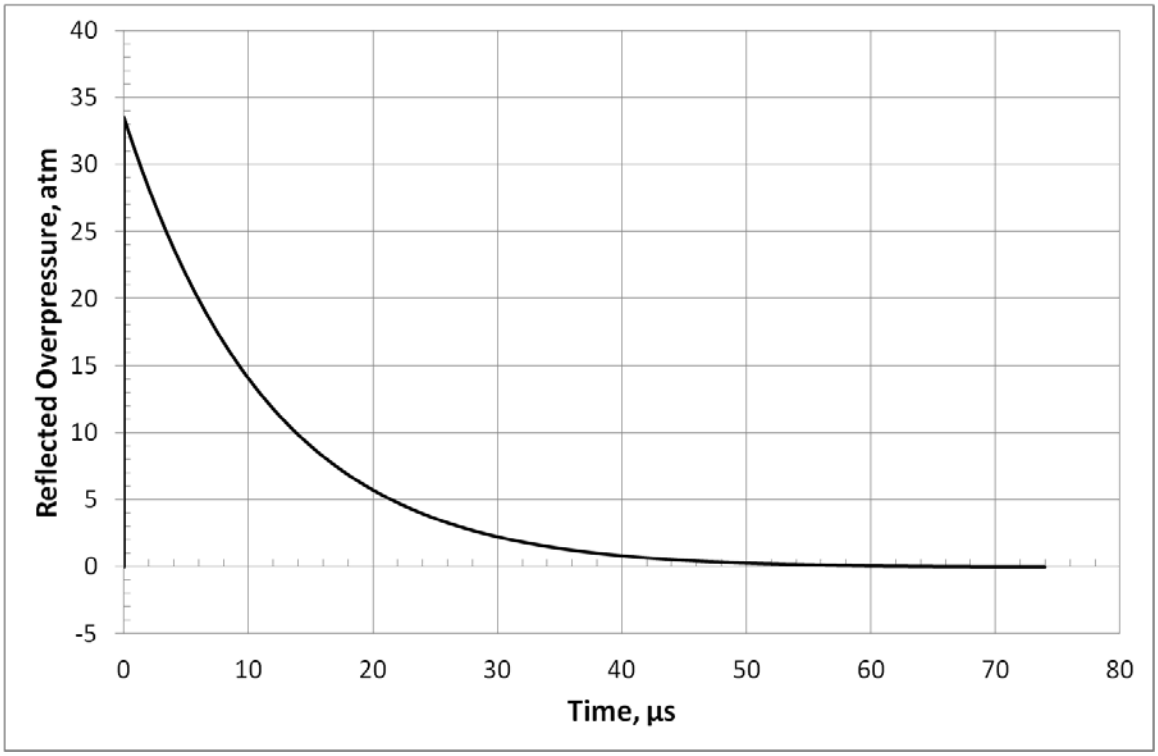

Figure 4.23: Plot of calculated reflected overpressure as a function of time at the center of a witness plate. Test conditions: 0.947g charge at a 12.5cm stand-off distance

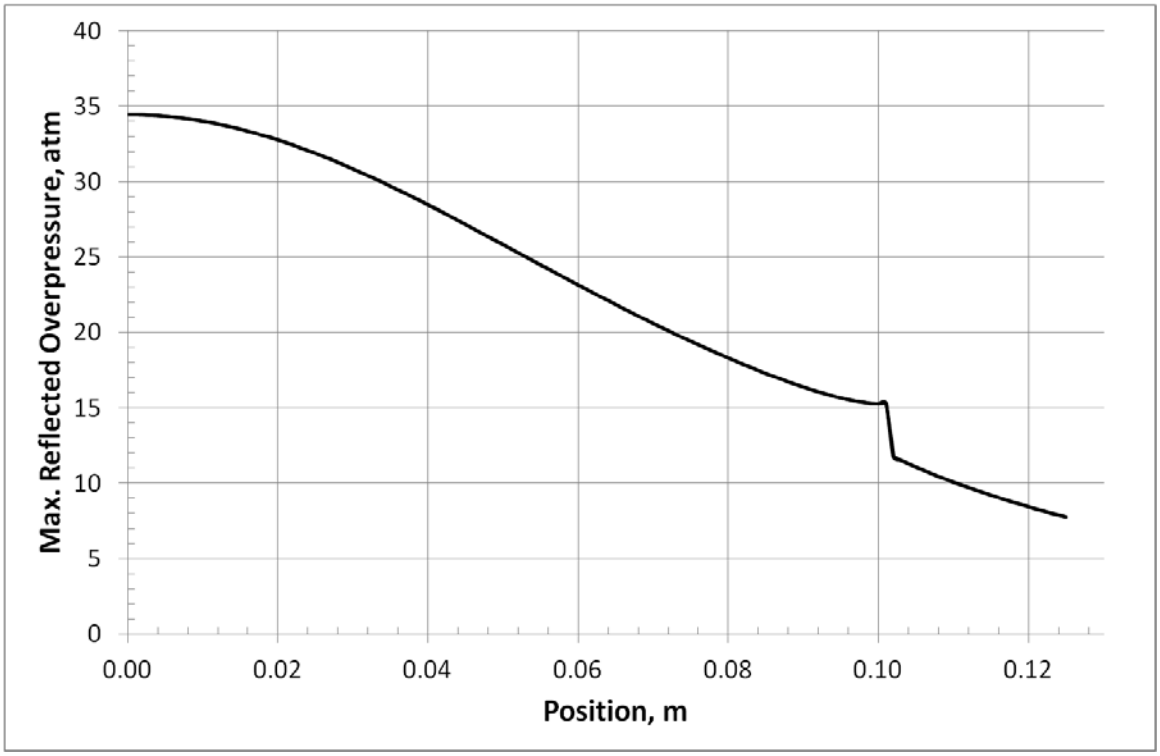

Figure 4.24: Plot of calculated maximum reflected overpressure as a function of radial location on a witness plate. Test conditions: 0.947g charge at a 12.5cm stand-off distance

4.3.2 Boundary Condition

Before dynamic deformation measurements were made on polyurea plates, some work was done to investigate the effect of the clamped circular edge boundary condition. Previous work by Hargather and Settles, and by Munday and Newitt, observed a deformation wave traveling towards the center of the plate from the clamped edge [38, 69]. This wave complicates the dynamics of the experiment, which may be undesirable (Figure 4.25a).

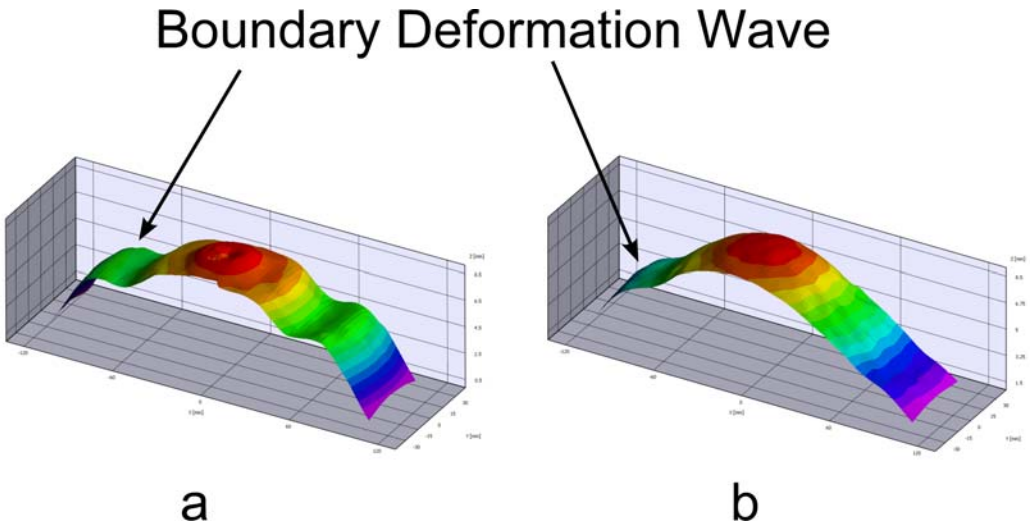

Figure 4.25: Polycarbonate plate deformation plots 0.5 ms after blast loading from a 1g charge at a 12.5 cm stand-off. A center-seeking deformation wave is observed for both boundary conditions tested: (a) Clamped boundary condition, (b) unclamped boundary condition.

Several experiments were run with polycarbonate plates to compare the dynamics of a clamped boundary with an unclamped-boundary condition. This boundary condition was created by eliminating one of the sides of the shock-hole fixture, and setting the plate in front of the remaining half of the fixture (Figure 4.26). This arrangement provides a point reaction load at the radius of the fixture opening, but does not resist plate bending or sliding at this boundary. Tests performed in this manner showed a center-seeking deformation wave (Figure 4.25b) similar to that seen in the clamped tests, but with a lower amplitude.

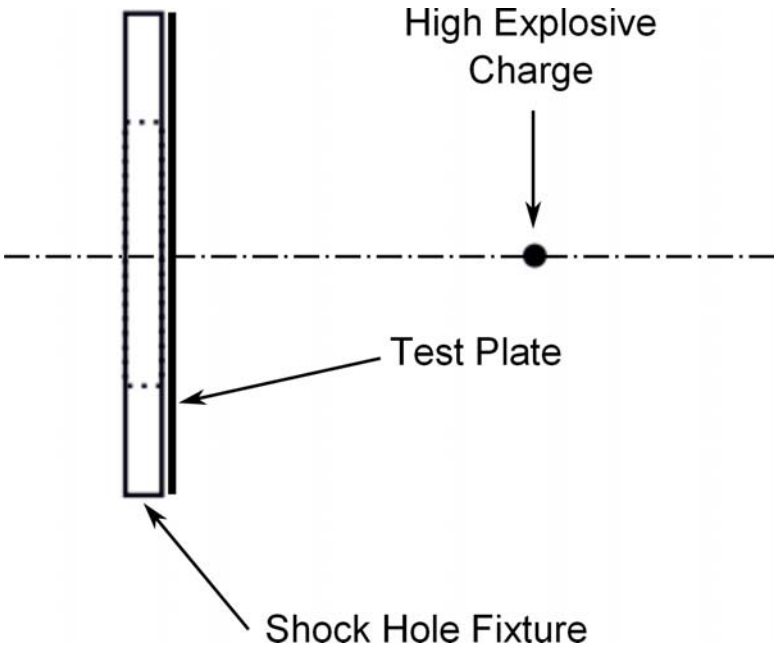

Figure 4.26: Schematic diagram of the unclamped boundary condition. In this configuration, the polymer test plate is placed in front of, and in contact with, the shock hole fixture, instead of being clamped into the fixture as in Figure 3.13.

Ultimately it was decided to return to the clamped boundary condition, since accurately representing the sliding friction of the unclamped boundary in a computational model would be quite difficult. While a free boundary condition, i.e. unsupported, would likely eliminate the observed deformation wave, this approach was not pursued due to practical and safety considerations.

4.3.3 Description of Dynamic Plate Deformation

The deformation behavior of all polymer witness plates tested in this work had several qualitative characteristics in common. In all cases, maximum deformation occurred at the center of the plate, and a deformation wave was observed to travel from the clamped boundary towards the center. Within these similarities, two main regimes of dynamic deformation were observed. The first, or small stand-off regime, occurred at scaled stand-off distances of less than 7 cm. In these cases, the maximum deformation occurred before the arrival of the boundary-induced deformation wave. The surface

(a)

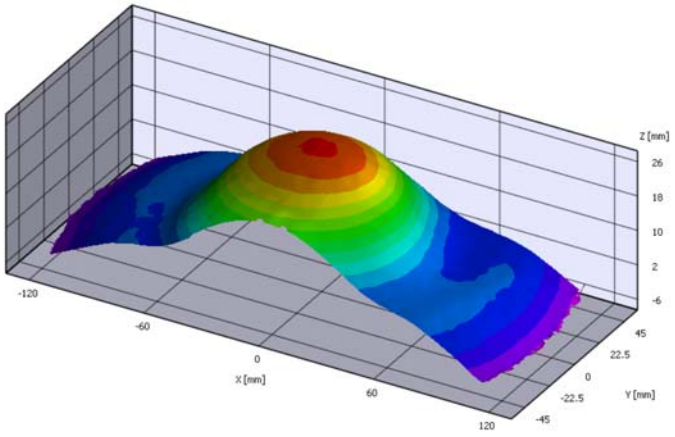

(b)

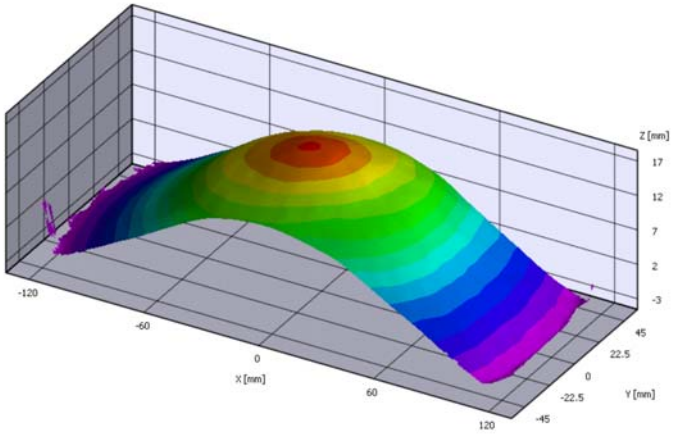

Figure 4.27: Deformation of polyurea plates in the (a) small stand-off regime, and (b) large stand-off regime. Both frames are taken at the time of maximum deformation, 0.62 ms and 2.1 ms, respectively.

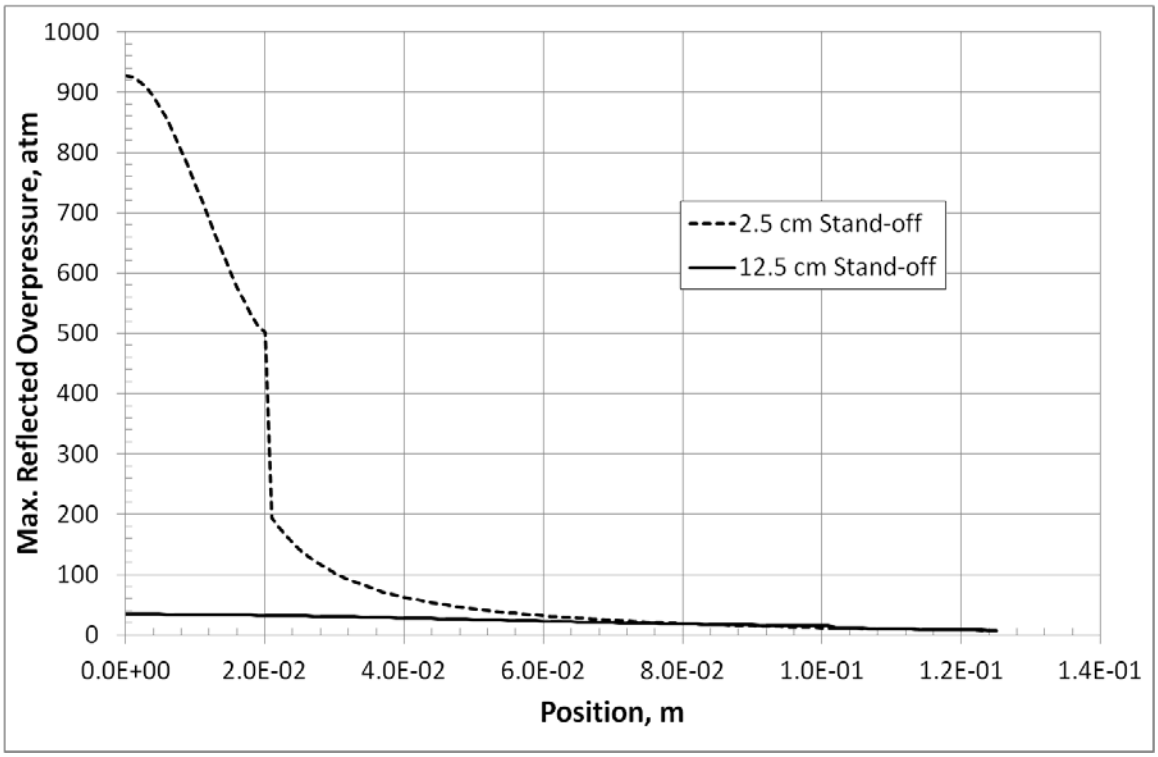

Figure 4.28: Plot of maximum reflected overpressure as a function of radial location on the witness plate. Short stand-off distances lead to a non-uniform centrally-weighted overpressure loading, while large stand off distances lead to more uniform overpressure loading. Test conditions: 0.947 g charge at a 12.5 cm stand-off distance and 0.935 g charge at a 2.5 cm stand-off distance

of the witness plate here takes on a steep, cone-like shape, and only a subset of the plate surface area is involved in the maximum deformation event (Figure 4.27a). The second, or large stand-off regime, occurred for scaled stand-off distances greater than or equal to 7 cm. In this loading regime, the maximum deformation occurs after the boundary-induced deformation wave reaches the center of the plate. The plate surface assumes a dome-like shape (Figure 4.27b), and all of the plate surface area is involved in the maximum deformation event.

These two regimes of deformation arise from the spherical nature of the blast loading. The curvature of the blast wave is inversely proportional to its radius from the charge. Therefore, at small stand-off distances a highly curved blast wave strikes the witness plate, producing a high central overpressure which is rapidly reduced away from the plate center. Conversely, large stand-off distances lead to a more-planar blast wave, with a more-uniform overpressure across the plate. Typical overpressure distributions on the witness plate for these two loading regimes are compared in Figure 4.28.

A plot of deformation and velocity at the center of a P-1000 polyurea test plate exposed to a 0.947 g charge at a 12.5 cm stand-off distance is shown in Figure 4.29. The out-of-plane deformation along a radius of the test plate at several times is also shown in Figure 4.30. The velocity of the plate center is seen to increase to 17 m/s with nearly constant acceleration until the pressure behind the plate has returned to P_{atm}, at approximately 0.1 ms (Figure 4.31). At this time, the plate has begun to take on the dome shape characteristic of large-deformation tests, even though the maximum deformation is less than 2 mm. After 0.1 ms has passed, the plate motion is driven by its own inertia and the motion of the boundary-produced deformation wave. At 0.3 ms, the center of the plate is observed to re-accelerate; this acceleration coincides with the first appearance of the boundary-produced deformation wave (Figure 4.32). After 0.8 ms has passed, the boundary-produced deformation wave has traveled inward from

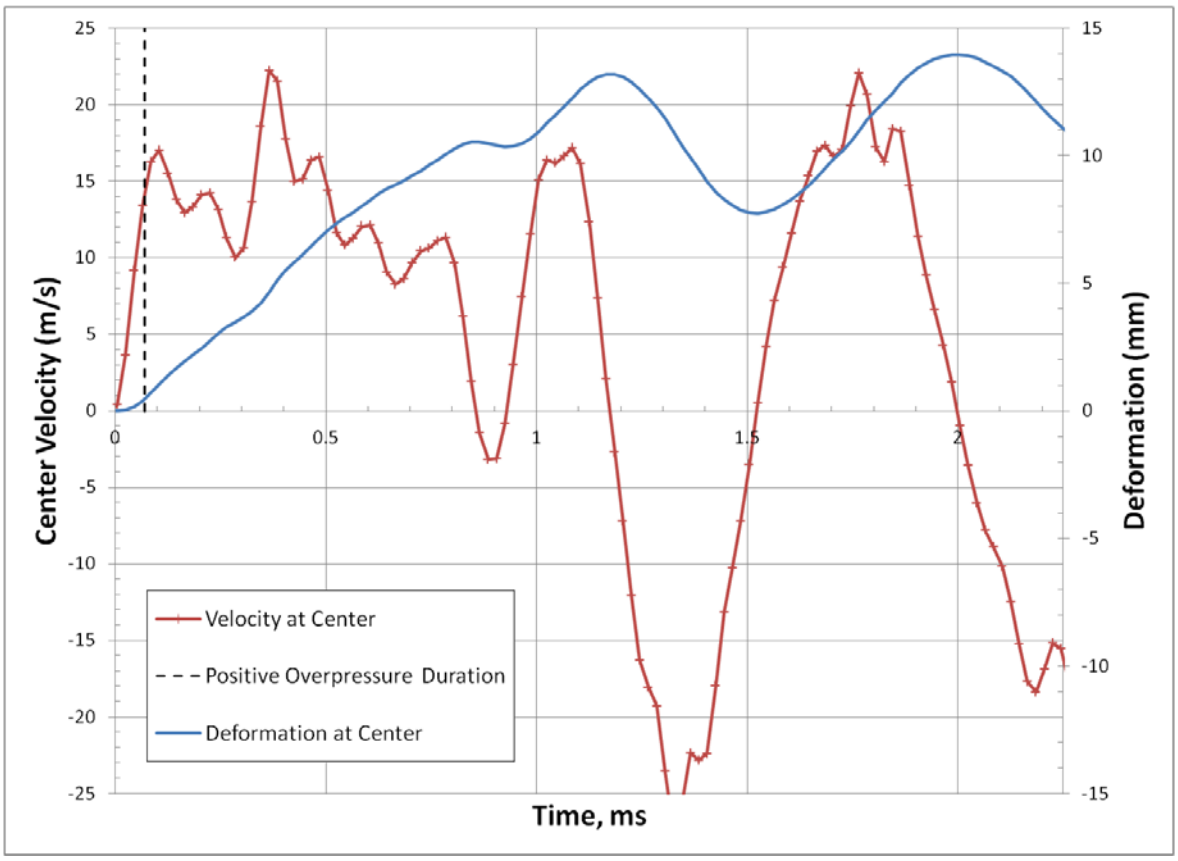

Figure 4.29: Plot of deformation and velocity as a function of time for a P-1000 polyurea witness plate exposed to a 0.947 g charge at a 12.5 cm stand-off distance.

the clamped edge approximately 6 cm toward the witness-plate center (Figure 4.33). The central surface area of the plate retains the slight dome shape formed by the blast loading, and has moved almost as a solid body. The outer edges of the plate have been influenced by the boundary-produced deformation wave, and take on a steeper, more cone-like shape. The symmetric reflection of the boundary-produced deformation wave at the plate center, produces a strong negative acceleration, seen in Figure 4.29 after 1.1 ms have passed. At 1.18 ms after blast loading, this negative acceleration brings the plate center to rest, and the maximum deformation of the plate is achieved, (Figure 4.34). After this point, the entire plate surface begins to recede back towards its equilibrium position. The plate oscillates between positive and negative deformation many times before returning to equilibrium.

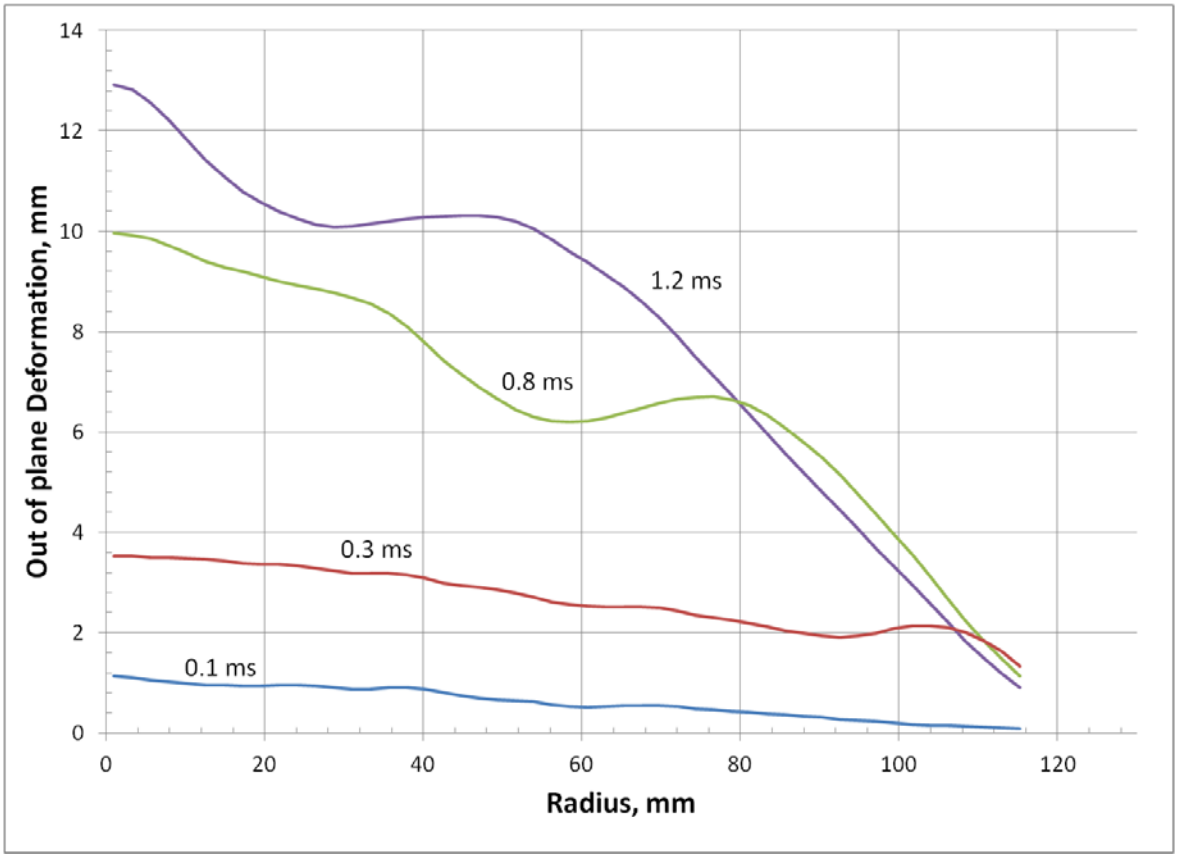

Figure 4.30: Plot of deformation as a function of radial location for a P-1000 polyurea witness plate exposed to a 0.947 g charge at a 12.5 cm stand-off distance.

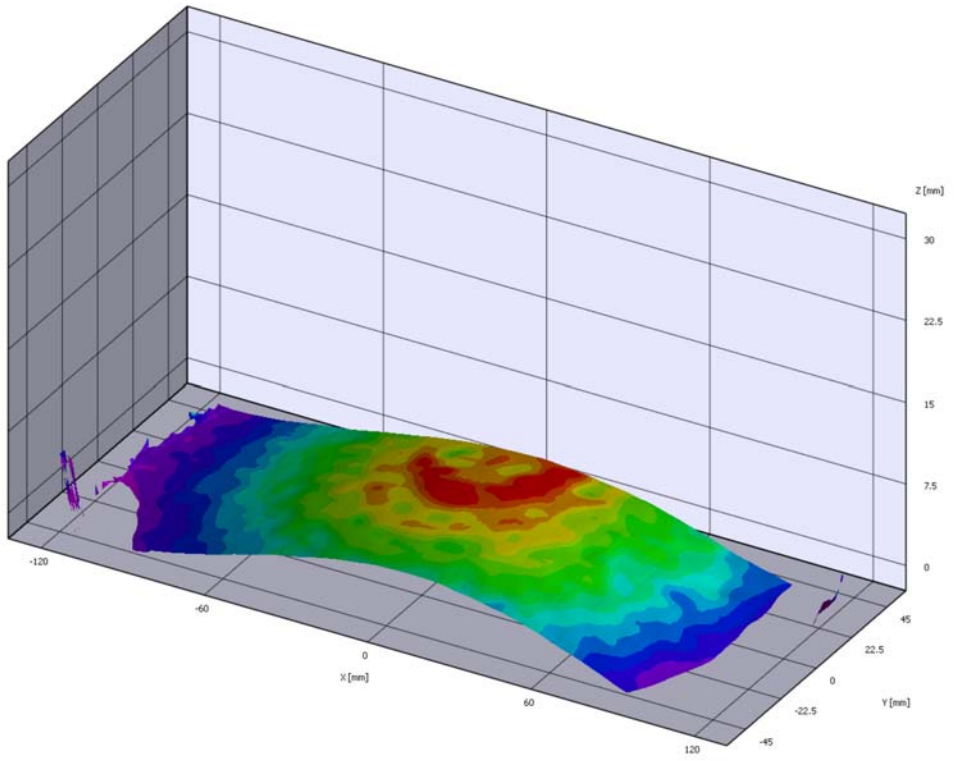

Figure 4.31: Plot of the surface shape of a P-1000 polyurea witness plate 0.1 ms after exposure to the blast wave produced by a 0.947 g charge at a 12.5 cm stand-off distance.

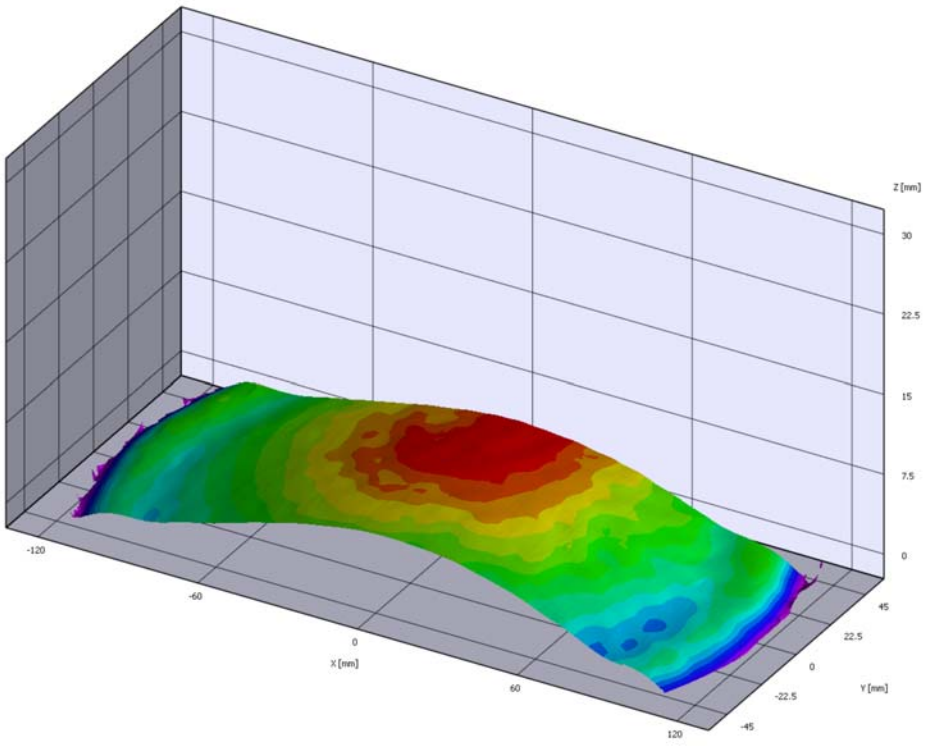

Figure 4.32: Plot of the surface shape of a P-1000 polyurea witness plate 0.3 ms after exposure to the blast wave produced by a 0.947 g charge at a 12.5 cm stand-off distance.

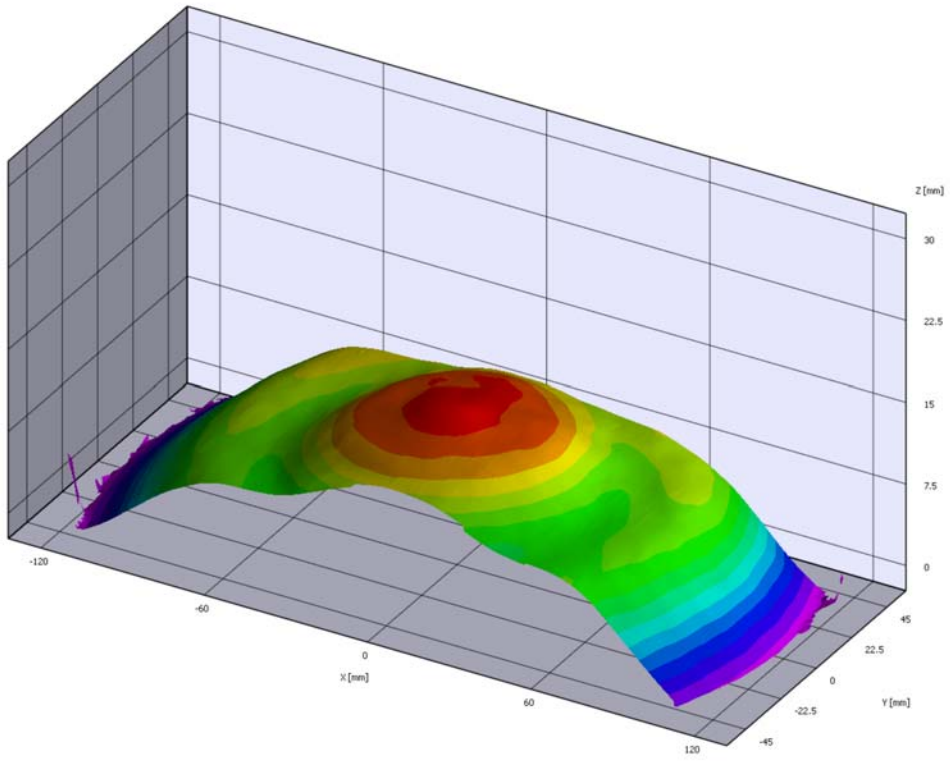

Figure 4.33: Plot of the surface shape of a P-1000 polyurea witness plate 0.8 ms after exposure to the blast wave produced by a 0.947 g charge at a 12.5 cm stand-off distance.

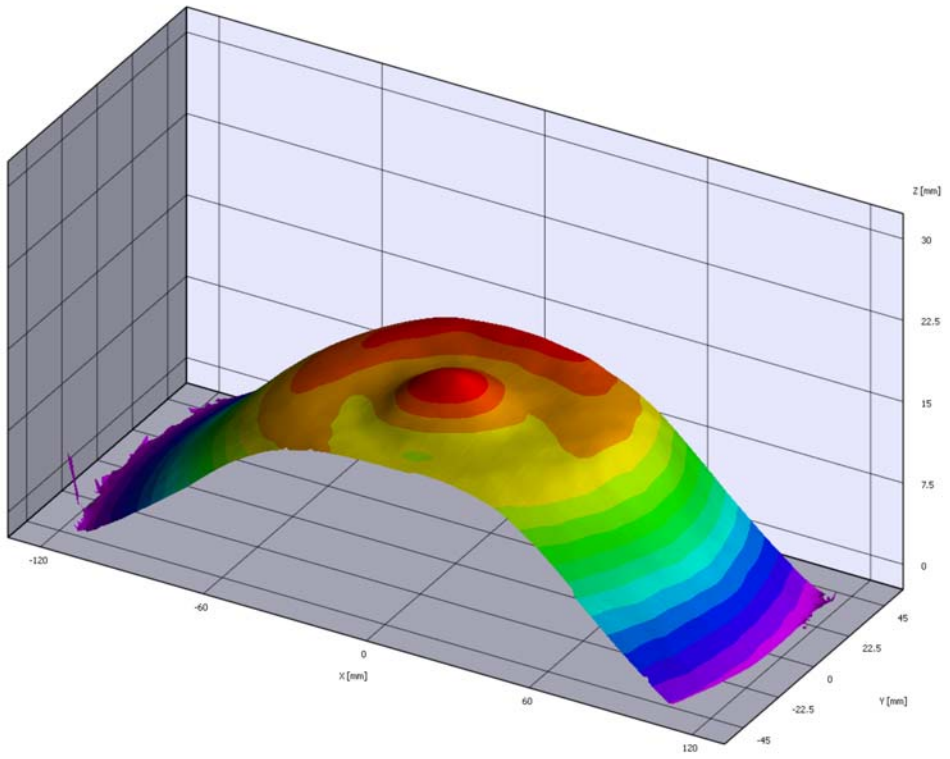

Figure 4.34: Plot of the surface shape of a P-1000 polyurea witness plate 1.2 ms after exposure to the blast wave produced by a 0.947 g charge at a 12.5 cm stand-off distance.

Quantitative, space- and time-resolved 3-D profiles of this type are available for position, velocity, strain, and strain rate for all the tests listed in Tables 4.2–4.5. This represents a sizable body of new data for polycarbonate, polyurethane, and polyurea plates under blast loading. This data set is of great value for the development and refinement of computational material models for these materials under blast loading. A collaborative effort with the Penn State Applied Research Lab is currently underway to use these data to benchmark and improve the computational material models available for polyurea under blast loading.

4.3.4 Maximum Deformation Results

Polymer witness plates of two nominal thicknesses (2 and 2.5 mm) were subjected to blast loading from 0.88–1.46 g PETN high-explosive charges at scaled stand-off distances of 2.5–45.7 cm. A summary of the results for P-1000 polyurea, P-650 polyurea, polyurethane, and polycarbonate plates can be found in Tables 4.2, 4.3, 4.4, and 4.5, respectively.

A plot of witness plate central maximum deformation vs. impulse loading for all cases is shown in Figure 4.35. A general trend towards higher maximum deformations is observed as charge stand-off distance is reduced,as expected, but to better compare with the literature some normalization is clearly called for. The maximum deformation results were therefore normalized following the procedure laid out by Nurick and Martin [37]. The loading is normalized to form the similarity variable ϕ_c given by equation 4.9

$$\phi_c = \frac{I}{\pi R t^2 (\rho \sigma_y)^{1/2}} \tag{4.9}$$

where I is the total reflected impulse, R the radius of the exposed portion of the witness plate, ρ the of the plate material density, and σ_y its static yield stress. Dynamic response is normalized by the plate thickness, t, as the deflection-thickness ratio: $\frac{W_{max}}{t}$ where W_{max} is the maximum central deflection of the witness plate.

Given this normalization, the polymer data are presented with the deflection-thickness prediction presented by Nurick and Martin for metal plates in Figure 4.36. The Nurick and Martin prediction was generated for metal plates under a uniform impulse loading, and therefore is not expected to match the polymer data presented here. A roughly linear divergence from the fit is observed as the impulse loading increases. This is believed to be primarily due to the mismatch in loading conditions between this work and that of Nurick and Martin. In this work, pressure loading is maximized at the center of the plate, which is also where the maximum deformation is observed. It is logical to postulate that the central deformation is most closely related to the pressure applied at the center. Since this central overpressure is greater than the overall average impulse acting on the plate would suggest, a greater central deformation than predicted by Nurick and Martin is expected.

Tests performed at a scaled stand-off greater than 35 cm load the plate with a Mach one shock wave, i.e., merely a loud sound wave. By definition, the overpressure across a sound wave is zero, therefore no impulse is predicted by the procedure outline above. Nonetheless, deflections of 3-4 mm were observed in experiments with scaled stand-offs of 35.7–45.7 cm (see Table 4.2). This is presumed to be a result of the inertia of the air accelerated by the blast wave before its decay to a loud sound wave. Although the wave itself can no longer apply an overpressure, this inertial 'wind' has a finite velocity which is stagnated by the witness plate. This produces a small overpressure, yielding the observed deformation. This overpressure could be measured with a sufficiently-sensitive pressure transducer, but such a transducer was unavailable for this work. Since impulse could not be defined for tests with a scaled stand-off greater than 35 cm, the Johnson damage number, ϕ_c, cannot be calculated and normalization is not possible.

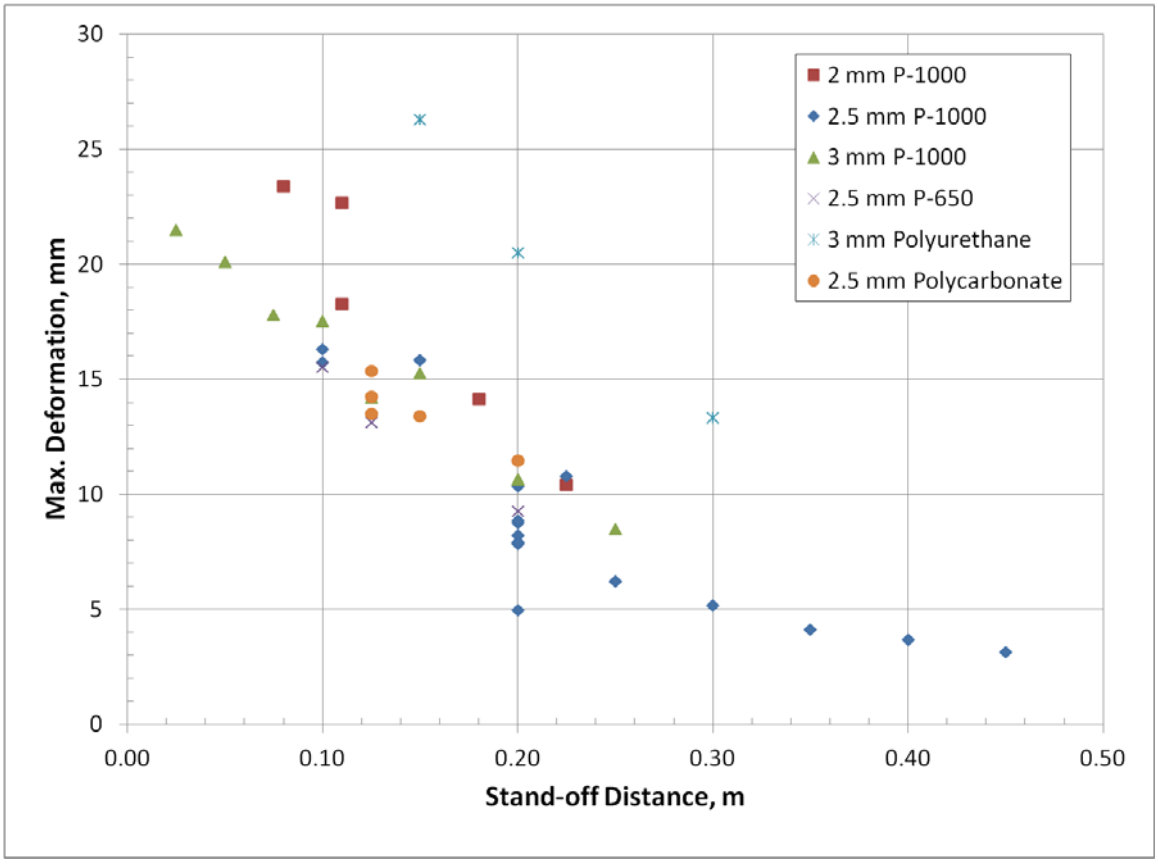

Figure 4.35: Plot of unnormalized plate deformation data. A general trend towards smaller deformations at large stand-off distances is observed.

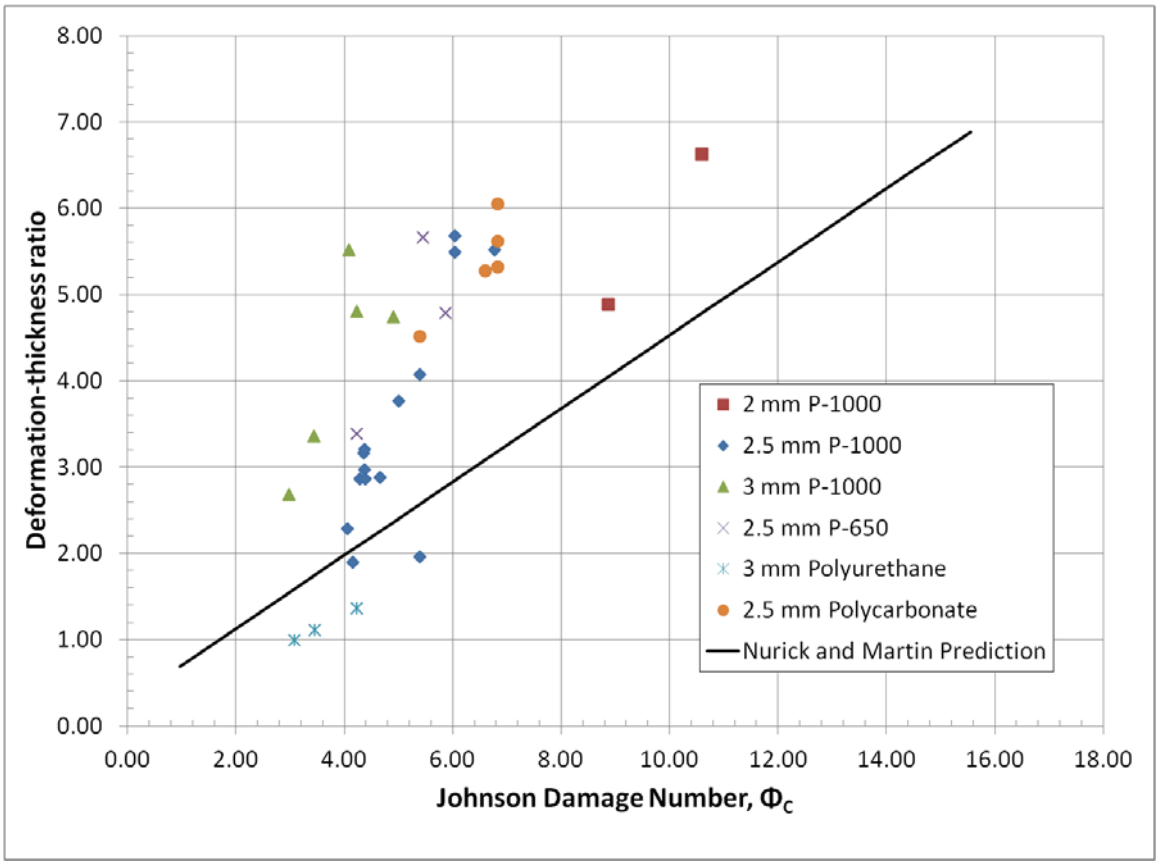

Figure 4.36: Plot of normalized plate deformation data. Only large stand-off ($R_{scaled} > 7cm$) experiments are included in this plot.

Table 4.2: Summary of the maximum deformation results for P-1000 polyurea plates

Plate Thickness (mm)	Charge Mass (g)	Scaled Stand-off (m)	Max. Def. (mm)	Def:t -	Impulse (N-s)	ϕ_c -
3.00	0.935	0.026	21.5	7.17	0.62	2.15
3.00	0.962	0.051	20.1	6.71	0.86	2.99
2.13	1.458	0.071	23.4	10.96	1.40	9.64
3.00	0.911	0.077	17.8	5.94	1.09	3.81
2.87	1.462	0.088	16.3	5.68	1.59	6.05
2.87	1.46	0.088	15.8	5.49	1.59	6.04
2.13	1.435	0.098	18.3	8.57	1.66	11.42
2.13	1.434	0.098	22.7	10.62	1.66	11.42
3.18	0.968	0.101	17.5	5.52	1.31	4.08
2.74	0.949	0.127	13.1	4.78	1.41	5.86
3.00	0.947	0.127	14.2	4.74	1.41	4.91
2.87	1.492	0.131	15.8	5.52	1.78	6.78
3.18	0.949	0.153	15.3	4.80	1.36	4.23
2.13	1.416	0.160	14.1	6.63	1.54	10.60
2.87	1.443	0.199	10.8	3.77	1.32	5.01
2.13	1.396	0.201	10.4	4.88	1.29	8.87
2.73	0.961	0.203	7.9	2.87	1.11	4.67
2.77	0.904	0.207	8.9	3.20	1.07	4.37
2.77	0.904	0.207	8.2	2.97	1.07	4.37
2.77	0.902	0.207	8.8	3.16	1.07	4.36
2.77	0.88	0.209	7.9	2.86	1.05	4.30
2.74	0.834	0.212	9.3	3.38	1.02	4.23
2.73	0.978	0.252	6.2	2.28	0.97	4.07
3.18	0.96	0.253	8.5	2.68	0.96	2.98
2.73	0.958	0.304	5.2	1.89	0.99	4.16
2.73	0.946	0.357	4.1	1.51	-	-
2.73	0.96	0.405	3.7	1.34	-	-
2.73	0.955	0.457	3.2	1.15	-	-

Table 4.3: Summary of the maximum deformation results for P-650 polyurea plates

Plate Thickness (mm)	Charge Mass (g)	Scaled Stand-off (m)	Max. Def. (mm)	Def:t -	Impulse (N-s)	ϕ_c -
2.74	0.96	0.101	15.5	5.66	1.31	5.45
2.74	0.953	0.203	10.7	3.36	1.10	3.43
2.74	0.909	0.206	7.9	2.86	1.07	4.38

Table 4.4: Summary of the maximum deformation results for polyurethane plates

Plate Thickness (mm)	Charge Mass (g)	Scaled Stand-off (m)	Max. Def. (mm)	Def:t -	Impulse (N-s)	ϕ_c -
3.175	0.959	0.304	13.4	4.20	0.99	3.08
3.175	0.954	0.203	20.5	6.46	1.11	3.45
3.175	0.957	0.152	26.3	8.28	1.36	4.23

Table 4.5: Summary of the maximum deformation results for polycarbonate plates

Plate Thickness (mm)	Charge Mass (g)	Scaled Stand-off (m)	Max. Def. (mm)	Def:t -	Impulse (N-s)	ϕ_c -
2.54	0.938	0.128	15.4	6.05	1.40	6.80
2.54	0.891	0.130	13.5	5.31	1.77	8.60
2.54	0.876	0.131	14.3	5.61	1.78	8.66
2.54	0.958	0.152	13.4	5.28	1.36	6.61
2.54	0.959	0.203	11.5	4.52	1.11	5.40

5 Summary and Conclusions

The present research has developed a suite of laboratory-scale, optically-based techniques which may be used to determine the response of both transparent and opaque materials to shock loading. These techniques fall under two main categories: measurements of shock wave transmission and dynamic plate deformation.

5.1 Shock Wave Transmission

Modern digital high-speed camera technology was combined with the time-honored shadowgraph technique to measure the shock Hugoniot of a transparent polyurethane and transparent to opaque polyureas. Waves were generated by exploding-bridge-wires, aluminum ballistic projectiles, and gram-scale high-explosive charges. The constant-velocity shock wave induced by a ballistic projectile allows observation of a single (U_s, U_{p2}) point per test in both transparent and opaque materials. In trans-

parent materials, the decelerating shock produced by a gram-scale explosive charge is observable throughout the sample plate, allowing multiple (U_s,U_{p2}) points to be measured in a single test, and thus reducing the number of tests required to fully define a shock Hugoniot. In all cases, Hugoniot data extrapolated from other investigations using stronger shock waves agree with data measured in this work, supporting the methods developed here and indicating that neither the polyurethane nor the polyurea examined here undergo a significant phase change in the region of $U_{p2} < 250$ m/s.

By using optical techniques and modern high-speed digital imaging, shock Hugoniot curves may be measured more readily than with traditional, non-optical point-by-point methodology. The approach presented in this work generates shock Hugoniot data with fewer experiments, without the use of costly consumables such as manganin pressure gages, and without cumbersome precision triggering. It also requires only an ordinary laboratory space, not an explosives test range or bunker. As presented, this method is appropriate for measuring shock velocites below approximately 3.5 km/s, limited only by the temporal resolution of the camera used.

5.2 Dynamic Plate Deformation

2-3 mm-thick polymer witness plates in a "shock hole" fixture were exposed to air blast loading by the detonation of 1-1.5 g high-explosive charges at stand-off distances of 2.5–50 cm. This produced a non-uniform pressure load on the plate surface. The magnitude and duration of this loading was determined *a priori* by combining existing explosive characterization data with gas dynamic theory. An analysis of the reflected blast overpressure data determined the blast loading on the witness plate as a function of radius.

The response of these polymer plates to the blast loading was observed by two high-speed-digital cameras in a stereoscopic arrangement. Through digital post-

processing, a quantitative, time-resolved, 3-D map of the deformation, strain, and velocity of the plate was constructed for each experiment.

These shock-hole tests produced a considerable body of data which are now available for the development and validation of computational constitutive models for the polycarbonate, polyurethane and polyurea formulations studied in this work. The shock-hole experiment is readily modeled, having both a well-defined boundary condition and a known overpressure load. Any significant differences between the FEA and experimental results may then be attributed to the computational material model. The model may then be adjusted until the computational and experimental results are in agreement. Polymer material modeling efforts using these data are currently underway at both the Penn State Applied Research lab and at Clemson University.

6 Future Work

6.1 Shock Wave Transmission

The experimental techniques presented here may be applied to the measurement of the shock Hugoniot of nearly any material, be it polymer or otherwise. The main restriction to applying this method to other materials is the temporal resolution of the high-speed camera used. Polymers have generally-low shock and sound velocities for solids ($C_l \leq 3000$ m/s), which makes accurate shock velocity measurements possible, given a high-speed camera with a frame rate of about 1 million frames per second (Such as the Photron SA-5 Camera used in this work). Application of these Hugoniot measurement techniques to solids with faster sound speeds would require a similarly-faster high speed camera. Several commercially-available framing cameras (such as the DRS ULTRA series) record at frame rates of up to 25 million frames per second. This frame rate would allow the application of this experimental technique to almost any conventional material.

Another important material property is the 'shock wave profile', that is, the functional character of the transition from unshocked to shocked state across a shock wave. In homogeneous fluids a shock wave is a nanometers-wide region of transition between material in the unshocked and shocked states, creating a step-function-like variation in properties across the shock wave. In more complex materials, shock-wave widths may increase due to factors such as heterogeneity or viscoelasticity. This leads to a more gradual or distributed change in properties across the shock wave. In transparent materials seeded with glass microspheres, the functional shape of this 'shock wave profile' can be observed by the techniques presented here, given a high-speed digital camera with a recording speed greater than 10 million frames per second. This would provide insight into the dispersive/dissipative mechanisms thought to be at work in some polymers, like polyurea.

6.2 Dynamic Plate Deformation

The development of accurate computational material models relies upon experiments, both to guide the correct form of the constitutive equation and to provide the correct numerical parameters to populate that equation. The latter portion of this process can be automated by employing a reverse parameter identification scheme. This scheme iteratively compares the full-field results of an experiment to a FE model with equivalent boundary conditions and loads. The differences between experiment and model are used to compute a cost function, which, in conjunction with a sensitivity analysis, allows iterative improvement of the model parameters. After a number of iterations, the proposed model either agrees with the experiment, in which case the model and parameters are correct, or else acceptable agreement is never achieved, which suggests that the constitutive equation chosen cannot accurately represent the material.

The 3-D, time resolved data sets produced by shock hole testing are ideal for use in such a reverse parameter identification scheme. The shock-hole experiment has well-defined boundary conditions and loading, so it can be accurately modeled. The strain field produced is also complex enough to contain sufficient information to fully parameterize a constitutive model. The primary challenges lie in developing the appropriate functional form of the constitutive equation for complex materials like polyurea, determining the sensitivity matrix for the problem, and integrating a scheme to iteratively update material model parameters with an appropriate FEA program. Once these obstacles are overcome, the shock hole test will become a fast and relatively-easy way to determine the appropriate model parameters for any material under blast loading.

7 Appendix 1: Matlab Blast Loading Calculator

```
%Plate overpressure calculator
%3/16/12 VERSION 1.0 -Initial Release
%4/9/2012 VERSION 2  - Correction to line 137 to remove an extra factor
%of Patm also added option to inculde negative phase of pressure
%profiles
%4/17/2012 VERSION 3 - Correction to impulse calculation to remove the
%atmosphereic pressure contribution

%Forrest Svingala, Gas Dynamics Lab PSU


%For a given mass of PETN and stand-off distance, this script
%calculates Pref(t) on the surface of a plate

%Shock Mach numbers come from a piecewise power law fit to Matt Biss'
%experimental data (Biss 2010, Propellants, exposives, pyrotechnics)

%The shape of the overpressure curve comes from Biss'
%reflected pressure traces (unpublished, personal communication 2012)

%Reflected overpressures are calculated for normal and oblique
%cases after "Explosions in Air" second ed. by Kinney and Graham

%%%%%%INSTRUCTIONS FOR USE%%%%%%%%
%1) Enter the charge mass and stand off distance
```

```
%2) Select the desired resolution of the calculation in time
%3) Select the length of time to output pressure data.
%4) Program returns a plot of Max overpressure as a function of plate
%radius and, optionally, a plot of all P(t) traces
%5) P(t) is saved as a comma delimited .txt file.The left-most
% column is the time vector, the top-most row is radial position on the

clear all
clc
%%%%%%%%%%%%%%%%%%%%%%%%%%%%%%%%%%%%%%%%%%%%%%%%%%%%%%%%%%%%%%%%%%%%%%%%%%%%%%%%%%%%%%
%User Inputs

%Name of P(t) output file
filename='P(t)_output.txt';
%Charge mass, grams
m=.427;

%Stand-off distance, meters
%(Valid range is 2.5-29cm for 1 gram charges.)
d=.1638;

%Length of time to output P(t) information, s
t_length=200e-6;

%Time step between P(t) values, s
t_step=5e-7;
```

```
%Would you like to see a plot of P(t)? 0=No, 1=Yes
pt_plot=1;

%Atmosphereic pressure, Pa
P_atm=101325;

%Include negative phase of pressure profile? 1=yes 0=No
neg_phase=1;
%%%%%%%%%%%%%%%%%%%%%%%%%%%%%%%%%%%%%%%%%%%%%%%%%%%%%%%%%%%%%%%%%%%%%%%%%%%%%%%%
%Calculation section, DO NOT MODIFY
%%

%Step size in plate radius, meters
r_step=0.001;
%initial guess on Beta, for r_step=0.001. Needs to be changed for
%other r_step values
betaguess=0.00109*d^(-1.0177);

t=[0:t_step:t_length];
k=size(t);

r_plate=[0:r_step:.125];
n=size(r_plate');

%P=P_atm*ones(n(1),k(2));
%Mass Scaling
S=m^(1/3);
```

```
c=1; %temperature scaling, not used
MFImpulse=0;
%Calculate shock impingement angle, and effective standoffs
for i=1:n
    d_eff(i)=(d^2+r_plate(i)^2)^.5;
    inc_angle(i)= asin(r_plate(i)/d_eff(i));
    d_eff_scaled(i)=d_eff(i)/S;
    td_scaled(i)=333.8541*d_eff_scaled(i)^5 - ...
        240.2028*d_eff_scaled(i)^4 + 48.09121*d_eff_scaled(i)^3 -...
        1.315445*d_eff_scaled(i)^2 + 0.3380876*d_eff_scaled(i)^1 +...
        0.002441429;
         %Pos overpressure duration after kinney and graham

    %Calculate Incident shock Mach number
    if d_eff_scaled(i) >= 0.0752 && d_eff_scaled(i)< 0.33
        M_shock(i)=0.332276*d_eff_scaled(i)^-0.99928;
    elseif d_eff_scaled(i) >= 0.02 && d_eff_scaled(i) < 0.0752
        M_shock(i)=0.587402*d_eff_scaled(i)^(-0.779107);
    else
        disp('Error, Effective stand-off falls '...
        'outside region of Mach number data')
        break
    end

    %Calculate Max Overpressure
    if i==1
        P_ref(i)=(4*M_shock(i)^2-1)*(7*M_shock(i)^2-1)/...
```

```
        (3*(M_shock(i)^2+5));
        %Normal reflected overpressure at center line
else
%Oblique reflection overpressure calculations
if inc_angle(i)<= 0.6807
    %Region where no mach stem forms
    M1=M_shock(i)/sin(inc_angle(i));
    theta=-atan(((5+M_shock(i)^2)/(6*M_shock(i)^2)*...
        tan(inc_angle(i))))+inc_angle(i);
    M2=((5+M_shock(i)^2)/((7*M_shock(i)^2-1)))^0.5/...
        sin(inc_angle(i)-theta);

    betafind=@(x)tan(x-theta)/tan(x)-(5+(M2*sin(x))^2)/...
        (6*(M2*sin(x))^2);
    [beta2(i) zero(i)]=fzero(betafind,betaguess);
    betaguess=beta2(i);
    %M3=((5+M2^2*sin(beta2(i))^2)/(7*M2^2*sin(beta2(i))^2-1))^0.5/
    %sin(beta2(i)-theta);
    Mref=M2*sin(beta2(i));
    P_ref(i)=((7*Mref^2-1)*(7*M_shock(i)^2-1))/36;
    if betaguess < 0
        disp('WARNING: Calculated reflection angle is negative.')
    end
else
   %Mach stem region
    M_stem=M_shock(i)/sin(inc_angle(i)); %Kinney & Graham ch5
    P_ref(i)=(7*M_stem^2-1)/6; %shock overpressure (4-20)
```

```
end
end

%Calculate td and impulses
td(i)=td_scaled(i)*S*10^-3; %actual overpressure duration, in s
alpha=-36.64*d_eff_scaled(i)+9.68; %Shape parameter for...
%Mod Friedlander eqn
Imp(i)=(P_ref(i)*P_atm-P_atm)*td(i)*((1/alpha)-(1/alpha^2)*...
    (1-exp(-alpha))); %Mod friedlander impulse for plate section i

if i<n(1)
area=pi()*(r_plate(i+1)^2-r_plate(i)^2);
else
area=0;
end
MFImpulse=MFImpulse+Imp(i)*area;
t_delay=(d_eff(i)-d_eff(1))/(.5*(M_shock(i)+M_shock(1))*347);
%Calculate P(t) for each location
for j=1:k(2)
    tmp=t(j)-t_delay;
    if t(j)<t_delay
        P(i,j)=P_atm;
    else
        %P(i,j)=P_atm+P_ref(i)*P_atm*(1-(tmp/td(i)))*...
        %exp(-alpha*tmp/td(i));% V1 calculation with error
        P(i,j)=P_atm+(P_ref(i)*P_atm-P_atm)*(1-(tmp/td(i)))*...
            exp(-alpha*tmp/td(i)); %Correction in V2
```

```
                if neg_phase==0
                 if P(i,j)<P_atm
                     P(i,j)=P_atm;
                 end
               end
            end
       end

end
%%
%%%%%%%%%%%%%%%%%%End Calculation Section%%%%%%%%%%%%%%%%%%%%%%%%%%%%%%%%%%%


MFImpulse


plot(r_plate,P_ref)
xlabel('Plate Radius, m')
ylabel('Pref, atm')
title('P(r)')



if pt_plot==1
     figure(2)
     plot(t,[P(1,:)-P_atm],t,[P(62,:)-P_atm],t,[P(125, :)-P_atm])
     xlabel('Time, s')
     ylabel('Pref, Pa')
     title('P(t)')
```

```
end


zero;


r_plate=[0 r_plate];
output=[t' P'];
output=[r_plate; output];
dlmwrite(filename,output);
```

8 Appendix 2: Dynamic Plate Deformation Data

The following is a collection of tables containing detailed, time-resolved data from selected plate deformation tests. The data below describe the out-of-plane deformation of each witness plate along a single radius, at increments of 10 mm. Time '0' denotes the frame immediately before bulk motion of the plate begins. Additional data are available as a digital attachment to the digital version of this thesis, available through the Penn State Library.

Table 8.1: Out-of-plane deformation of a 2.7 mm-thick P-650 Polyurea plate, exposed to a 0.949 g PETN charge at a 12.5 cm stand-off distance.

Time, ms	Radial position, mm												
	0	10	20	30	40	50	60	70	80	90	100	110	120
0	0.00	0.00	0.00	0.00	0.00	0.00	0.00	0.00	0.00	0.00	0.00	0.00	0.00
0.02	0.25	0.23	0.23	0.23	0.21	0.18	0.17	0.17	0.16	0.14	0.16	0.14	0.17
0.04	0.49	0.45	0.46	0.43	0.43	0.37	0.33	0.36	0.34	0.31	0.32	0.32	0.39
0.06	0.72	0.65	0.69	0.63	0.65	0.56	0.50	0.55	0.53	0.46	0.52	0.53	0.61
0.08	0.95	0.84	0.90	0.81	0.85	0.75	0.67	0.73	0.70	0.64	0.73	0.80	0.76
0.1	1.18	1.03	1.10	1.00	1.03	0.92	0.83	0.89	0.88	0.82	0.93	1.10	0.88
0.12	1.40	1.23	1.30	1.19	1.19	1.11	1.01	1.05	1.06	1.03	1.14	1.40	0.97
0.14	1.64	1.43	1.49	1.41	1.39	1.28	1.20	1.23	1.24	1.25	1.35	1.68	1.05
0.16	1.88	1.66	1.69	1.61	1.59	1.48	1.41	1.40	1.43	1.44	1.59	1.93	1.13
0.18	2.13	1.91	1.89	1.85	1.81	1.68	1.61	1.57	1.61	1.63	1.87	2.14	1.16
0.2	2.37	2.17	2.09	2.07	2.04	1.89	1.81	1.73	1.79	1.80	2.17	2.33	1.18
0.22	2.62	2.42	2.30	2.31	2.25	2.08	2.00	1.90	1.97	2.00	2.47	2.47	1.21
0.24	2.90	2.68	2.54	2.51	2.47	2.27	2.17	2.08	2.13	2.19	2.72	2.58	1.21
0.26	3.17	2.95	2.79	2.70	2.70	2.47	2.31	2.27	2.25	2.38	2.94	2.66	1.21
0.28	3.47	3.21	3.04	2.90	2.92	2.65	2.47	2.45	2.38	2.60	3.17	2.73	1.19
0.3	3.78	3.49	3.28	3.11	3.10	2.82	2.61	2.60	2.50	2.85	3.40	2.78	1.18
0.32	4.10	3.79	3.54	3.35	3.29	2.98	2.79	2.72	2.63	3.13	3.59	2.81	1.18
0.34	4.44	4.09	3.78	3.58	3.46	3.15	2.98	2.81	2.77	3.36	3.74	2.83	1.16
0.36	4.73	4.37	4.03	3.81	3.65	3.34	3.19	2.89	2.91	3.59	3.88	2.84	1.15
0.38	5.01	4.60	4.26	4.02	3.83	3.54	3.36	2.96	3.08	3.83	3.99	2.85	1.13
0.4	5.27	4.82	4.48	4.20	4.03	3.74	3.50	3.06	3.29	4.05	4.10	2.85	1.12
0.42	5.52	5.05	4.70	4.38	4.21	3.93	3.60	3.17	3.50	4.29	4.20	2.85	1.11
0.44	5.77	5.29	4.90	4.53	4.35	4.10	3.70	3.28	3.75	4.48	4.29	2.86	1.12
0.46	6.01	5.52	5.09	4.67	4.48	4.25	3.78	3.42	3.99	4.67	4.36	2.85	1.10
0.48	6.24	5.76	5.29	4.82	4.61	4.40	3.88	3.60	4.22	4.82	4.41	2.85	1.10
0.5	6.45	5.99	5.48	4.96	4.74	4.53	3.96	3.78	4.42	4.98	4.44	2.85	1.10

Table 8.1a: Continuation of table 8.1

Time, ms	Radial position, mm												
	0	10	20	30	40	50	60	70	80	90	100	110	120
0.52	6.63	6.20	5.65	5.09	4.87	4.65	4.05	3.97	4.62	5.08	4.47	2.84	1.09
0.54	6.80	6.39	5.83	5.21	5.00	4.74	4.15	4.18	4.83	5.19	4.48	2.85	1.08
0.56	6.94	6.57	5.98	5.35	5.15	4.82	4.26	4.37	5.05	5.27	4.49	2.83	1.06
0.58	7.09	6.76	6.14	5.51	5.27	4.92	4.37	4.57	5.25	5.34	4.46	2.80	1.04
0.6	7.25	6.92	6.28	5.68	5.42	4.99	4.49	4.77	5.45	5.40	4.44	2.78	1.03
0.62	7.43	7.09	6.42	5.88	5.56	5.04	4.60	4.97	5.61	5.44	4.40	2.74	1.01
0.64	7.65	7.26	6.60	6.08	5.73	5.11	4.73	5.18	5.74	5.47	4.35	2.69	1.00
0.66	7.90	7.44	6.79	6.28	5.89	5.19	4.89	5.40	5.87	5.49	4.30	2.63	0.97
0.68	8.16	7.61	6.99	6.50	6.04	5.28	5.07	5.63	5.99	5.50	4.26	2.59	0.97
0.7	8.40	7.77	7.20	6.74	6.14	5.38	5.27	5.84	6.11	5.50	4.21	2.54	0.95
0.72	8.57	7.94	7.42	6.97	6.22	5.50	5.47	6.07	6.22	5.50	4.16	2.49	0.94
0.74	8.71	8.11	7.65	7.18	6.31	5.63	5.68	6.29	6.34	5.51	4.12	2.45	0.92
0.76	8.80	8.27	7.91	7.34	6.40	5.78	5.88	6.50	6.46	5.50	4.06	2.41	0.92
0.78	8.84	8.43	8.14	7.48	6.48	5.93	6.10	6.70	6.56	5.50	4.02	2.38	0.90
0.8	8.87	8.59	8.37	7.60	6.57	6.09	6.33	6.86	6.65	5.49	3.97	2.33	0.90
0.82	8.89	8.74	8.59	7.70	6.68	6.28	6.58	7.04	6.71	5.47	3.93	2.30	0.89
0.84	8.92	8.92	8.76	7.80	6.78	6.47	6.82	7.20	6.76	5.45	3.88	2.27	0.88
0.86	8.99	9.07	8.93	7.88	6.91	6.70	7.05	7.37	6.80	5.43	3.83	2.23	0.87
0.88	9.11	9.24	9.06	7.94	7.05	6.94	7.26	7.50	6.82	5.40	3.80	2.21	0.87
0.9	9.25	9.40	9.17	8.01	7.23	7.20	7.47	7.61	6.83	5.37	3.76	2.19	0.85
0.92	9.44	9.57	9.26	8.07	7.40	7.43	7.68	7.70	6.84	5.33	3.70	2.16	0.85
0.94	9.68	9.72	9.30	8.15	7.60	7.66	7.89	7.78	6.83	5.29	3.67	2.14	0.83
0.96	9.95	9.88	9.31	8.22	7.80	7.89	8.09	7.87	6.82	5.24	3.62	2.12	0.82
0.98	10.25	9.99	9.29	8.28	7.99	8.14	8.26	7.94	6.82	5.19	3.58	2.08	0.81
1	10.53	10.08	9.26	8.36	8.17	8.38	8.42	8.00	6.78	5.15	3.54	2.05	0.80

Table 8.1b: Continuation of table 8.1

Time, ms	Radial position, mm												
	0	10	20	30	40	50	60	70	80	90	100	110	120
1.02	10.79	10.15	9.22	8.42	8.34	8.59	8.58	8.07	6.76	5.09	3.50	2.02	0.78
1.04	11.02	10.20	9.16	8.48	8.54	8.81	8.71	8.13	6.71	5.04	3.46	1.99	0.76
1.06	11.19	10.24	9.10	8.53	8.75	9.00	8.84	8.14	6.68	4.97	3.40	1.94	0.74
1.08	11.31	10.26	9.06	8.59	8.96	9.20	8.96	8.15	6.61	4.95	3.36	1.91	0.73
1.1	11.36	10.26	9.04	8.65	9.15	9.40	9.06	8.15	6.55	4.89	3.33	1.88	0.71
1.12	11.33	10.23	9.03	8.73	9.31	9.59	9.15	8.16	6.49	4.84	3.29	1.85	0.69
1.14	11.23	10.19	9.05	8.84	9.46	9.76	9.23	8.13	6.43	4.77	3.22	1.82	0.68
1.16	11.08	10.12	9.08	8.96	9.60	9.94	9.30	8.10	6.37	4.72	3.18	1.78	0.69
1.18	10.85	10.03	9.13	9.11	9.77	10.08	9.34	8.07	6.32	4.66	3.13	1.74	0.67
1.2	10.57	9.91	9.18	9.29	9.96	10.21	9.38	8.03	6.29	4.62	3.07	1.70	0.65
1.22	10.21	9.75	9.23	9.48	10.16	10.33	9.40	8.00	6.25	4.57	3.02	1.66	0.64
1.24	9.86	9.53	9.30	9.63	10.36	10.43	9.40	7.94	6.21	4.52	2.96	1.62	0.62
1.26	9.51	9.34	9.37	9.77	10.50	10.49	9.40	7.88	6.17	4.47	2.91	1.60	0.61
1.28	9.16	9.16	9.42	9.91	10.60	10.54	9.39	7.82	6.11	4.41	2.86	1.57	0.62
1.3	8.77	9.00	9.49	10.05	10.69	10.57	9.37	7.77	6.05	4.35	2.80	1.56	0.62
1.32	8.36	8.82	9.56	10.19	10.77	10.58	9.33	7.70	5.99	4.28	2.76	1.54	0.63
1.34	8.00	8.61	9.62	10.35	10.83	10.57	9.27	7.62	5.91	4.22	2.71	1.54	0.62
1.36	7.67	8.41	9.68	10.52	10.90	10.55	9.21	7.55	5.82	4.16	2.69	1.51	0.63
1.38	7.41	8.25	9.72	10.67	10.97	10.50	9.15	7.49	5.73	4.08	2.65	1.52	0.64
1.4	7.20	8.13	9.77	10.82	11.05	10.46	9.06	7.42	5.64	4.02	2.60	1.51	0.64
1.42	7.04	8.04	9.81	10.93	11.09	10.41	8.97	7.36	5.55	3.95	2.57	1.50	0.63
1.44	6.95	7.99	9.84	11.03	11.12	10.34	8.87	7.28	5.48	3.89	2.54	1.48	0.61
1.46	6.93	7.98	9.86	11.08	11.14	10.26	8.76	7.21	5.42	3.83	2.51	1.47	0.59
1.48	6.98	8.00	9.89	11.13	11.13	10.18	8.63	7.12	5.35	3.77	2.48	1.46	0.57
1.5	7.06	8.06	9.92	11.16	11.12	10.11	8.53	7.00	5.27	3.74	2.46	1.44	0.55

Table 8.1c: Continuation of table 8.1

Time, ms	Radial position, mm												
	0	10	20	30	40	50	60	70	80	90	100	110	120
1.52	7.20	8.16	9.94	11.14	11.09	10.04	8.41	6.88	5.22	3.67	2.44	1.42	0.54
1.54	7.37	8.29	9.97	11.13	11.01	9.95	8.30	6.75	5.15	3.63	2.41	1.42	0.55
1.56	7.59	8.46	10.01	11.07	10.94	9.85	8.19	6.63	5.08	3.60	2.39	1.39	0.56
1.58	7.86	8.68	10.04	11.01	10.85	9.74	8.06	6.51	5.03	3.58	2.39	1.38	0.56
1.6	8.16	8.90	10.09	10.90	10.74	9.63	7.95	6.40	4.96	3.57	2.37	1.38	0.56
1.62	8.49	9.12	10.14	10.79	10.63	9.51	7.84	6.30	4.90	3.56	2.36	1.39	0.59
1.64	8.83	9.33	10.21	10.67	10.50	9.38	7.74	6.21	4.84	3.54	2.37	1.39	0.59
1.66	9.16	9.56	10.27	10.57	10.35	9.24	7.63	6.11	4.78	3.54	2.36	1.39	0.61
1.68	9.48	9.82	10.33	10.45	10.21	9.09	7.52	6.02	4.74	3.53	2.36	1.40	0.62
1.7	9.82	10.11	10.39	10.36	10.07	8.95	7.41	5.93	4.67	3.53	2.37	1.40	0.62
1.72	10.18	10.39	10.43	10.25	9.90	8.80	7.31	5.83	4.61	3.50	2.37	1.44	0.63
1.74	10.57	10.60	10.45	10.15	9.75	8.64	7.19	5.75	4.55	3.48	2.40	1.45	0.64
1.76	10.91	10.80	10.48	10.05	9.59	8.49	7.06	5.67	4.51	3.46	2.41	1.48	0.63
1.78	11.25	11.03	10.52	9.94	9.43	8.32	6.94	5.59	4.46	3.45	2.43	1.50	0.63
1.8	11.60	11.28	10.56	9.81	9.22	8.14	6.81	5.51	4.39	3.44	2.47	1.51	0.62
1.82	11.93	11.52	10.58	9.69	8.98	7.93	6.68	5.44	4.33	3.40	2.48	1.54	0.62
1.84	12.23	11.71	10.61	9.57	8.73	7.73	6.56	5.34	4.28	3.38	2.51	1.56	0.63
1.86	12.50	11.87	10.63	9.45	8.50	7.52	6.42	5.26	4.23	3.38	2.53	1.57	0.63
1.88	12.72	11.99	10.64	9.32	8.35	7.32	6.26	5.17	4.18	3.36	2.55	1.57	0.62
1.9	12.89	12.09	10.64	9.20	8.19	7.11	6.09	5.09	4.14	3.34	2.54	1.58	0.61
1.92	13.01	12.18	10.64	9.10	8.00	6.90	5.92	5.01	4.10	3.31	2.54	1.57	0.62
1.94	13.09	12.23	10.63	8.99	7.77	6.70	5.79	4.93	4.06	3.29	2.53	1.56	0.61
1.96	13.11	12.25	10.61	8.89	7.55	6.50	5.65	4.85	4.01	3.29	2.51	1.57	0.62
1.98	13.08	12.23	10.59	8.77	7.38	6.33	5.52	4.79	3.97	3.28	2.49	1.56	0.63
2	13.01	12.18	10.52	8.65	7.23	6.15	5.36	4.70	3.93	3.27	2.49	1.56	0.63

Table 8.1d: Continuation of table 8.1

Time, ms	Radial position, mm												
	0	10	20	30	40	50	60	70	80	90	100	110	120
2.02	12.90	12.10	10.47	8.53	7.06	5.95	5.18	4.62	3.89	3.24	2.46	1.57	0.64
2.04	12.76	12.01	10.37	8.41	6.89	5.76	5.00	4.51	3.89	3.24	2.44	1.54	0.66
2.06	12.61	11.89	10.27	8.31	6.70	5.56	4.86	4.40	3.86	3.24	2.43	1.55	0.66
2.08	12.41	11.75	10.15	8.18	6.52	5.38	4.71	4.28	3.84	3.23	2.42	1.55	0.67
2.1	12.15	11.56	10.02	8.07	6.36	5.21	4.57	4.17	3.80	3.23	2.40	1.56	0.67
2.12	11.90	11.33	9.86	7.94	6.21	5.04	4.43	4.07	3.77	3.21	2.39	1.55	0.70
2.14	11.63	11.08	9.70	7.81	6.06	4.87	4.27	3.99	3.73	3.20	2.38	1.55	0.70
2.16	11.37	10.83	9.52	7.66	5.92	4.72	4.11	3.90	3.69	3.17	2.36	1.54	0.68
2.18	11.10	10.58	9.36	7.52	5.78	4.56	3.95	3.82	3.65	3.16	2.34	1.52	0.70
2.2	10.80	10.34	9.16	7.38	5.65	4.41	3.80	3.75	3.60	3.14	2.33	1.52	0.67
2.22	10.48	10.08	8.93	7.22	5.53	4.29	3.64	3.66	3.56	3.12	2.33	1.51	0.67
2.24	10.17	9.75	8.69	7.08	5.44	4.18	3.51	3.56	3.51	3.11	2.33	1.49	0.66
2.26	9.85	9.41	8.43	6.91	5.32	4.08	3.41	3.48	3.44	3.08	2.34	1.50	0.64
2.28	9.54	9.08	8.20	6.74	5.24	3.99	3.32	3.41	3.39	3.05	2.34	1.50	0.63
2.3	9.23	8.77	7.95	6.57	5.13	3.90	3.22	3.31	3.34	3.04	2.32	1.48	0.62
2.32	8.92	8.49	7.70	6.39	5.04	3.82	3.14	3.22	3.28	3.01	2.34	1.46	0.59
2.34	8.55	8.18	7.43	6.22	4.94	3.75	3.06	3.12	3.20	3.00	2.34	1.47	0.58
2.36	8.17	7.83	7.14	6.03	4.85	3.67	2.99	3.02	3.15	2.96	2.36	1.46	0.59
2.38	7.80	7.47	6.88	5.85	4.75	3.61	2.94	2.93	3.08	2.93	2.35	1.47	0.58
2.4	7.45	7.17	6.60	5.67	4.66	3.55	2.88	2.83	3.00	2.90	2.35	1.45	0.58
2.42	7.11	6.88	6.35	5.47	4.55	3.50	2.83	2.74	2.94	2.88	2.34	1.43	0.57
2.44	6.73	6.58	6.07	5.27	4.44	3.45	2.77	2.67	2.88	2.84	2.34	1.43	0.56
2.46	6.37	6.21	5.76	5.07	4.34	3.39	2.74	2.58	2.80	2.81	2.32	1.43	0.56
2.48	6.01	5.84	5.48	4.86	4.20	3.34	2.69	2.50	2.72	2.76	2.31	1.43	0.56
2.5	5.67	5.50	5.22	4.65	4.07	3.29	2.65	2.42	2.66	2.72	2.30	1.43	0.54

Table 8.1e: Continuation of table 8.1

Time, ms	Radial position, mm												
	0	10	20	30	40	50	60	70	80	90	100	110	120
2.52	5.35	5.18	4.95	4.46	3.94	3.24	2.61	2.36	2.57	2.68	2.30	1.43	0.56
2.54	5.00	4.86	4.66	4.28	3.80	3.18	2.57	2.29	2.50	2.62	2.27	1.44	0.58
2.56	4.66	4.52	4.37	4.09	3.68	3.12	2.52	2.23	2.45	2.57	2.23	1.43	0.58
2.58	4.29	4.18	4.08	3.88	3.58	3.06	2.49	2.17	2.38	2.53	2.22	1.43	0.58
2.6	3.93	3.84	3.81	3.66	3.46	3.00	2.46	2.12	2.30	2.47	2.21	1.43	0.57
2.62	3.61	3.53	3.53	3.46	3.37	2.94	2.42	2.10	2.25	2.41	2.18	1.45	0.58
2.64	3.31	3.26	3.28	3.25	3.27	2.87	2.38	2.05	2.19	2.37	2.14	1.46	0.62
2.66	3.02	2.99	3.02	3.07	3.16	2.80	2.33	2.02	2.13	2.31	2.11	1.45	0.61
2.68	2.72	2.70	2.73	2.89	3.05	2.73	2.30	1.98	2.08	2.25	2.08	1.46	0.61
2.7	2.41	2.36	2.44	2.71	2.91	2.67	2.28	1.95	2.02	2.20	2.06	1.47	0.64
2.72	2.07	1.99	2.14	2.52	2.77	2.60	2.24	1.94	1.97	2.13	2.01	1.46	0.64
2.74	1.72	1.63	1.88	2.30	2.62	2.51	2.21	1.92	1.94	2.07	1.96	1.46	0.66
2.76	1.37	1.31	1.61	2.05	2.49	2.44	2.17	1.90	1.90	2.01	1.92	1.44	0.66
2.78	1.06	1.02	1.35	1.81	2.34	2.36	2.15	1.89	1.86	1.98	1.89	1.45	0.66
2.8	0.75	0.75	1.10	1.57	2.20	2.28	2.12	1.88	1.83	1.93	1.87	1.43	0.66
2.82	0.44	0.47	0.83	1.37	2.05	2.19	2.08	1.85	1.80	1.88	1.81	1.41	0.65
2.84	0.12	0.16	0.56	1.19	1.90	2.11	2.04	1.83	1.75	1.83	1.77	1.37	0.65
2.86	-0.19	-0.15	0.30	1.02	1.75	2.02	2.01	1.80	1.71	1.77	1.72	1.35	0.65
2.88	-0.49	-0.44	0.06	0.84	1.60	1.95	1.98	1.78	1.68	1.72	1.67	1.31	0.63
2.9	-0.80	-0.71	-0.18	0.62	1.42	1.85	1.96	1.79	1.65	1.67	1.64	1.28	0.63
2.92	-1.13	-0.98	-0.40	0.38	1.26	1.79	1.92	1.76	1.63	1.63	1.59	1.25	0.62
2.94	-1.46	-1.27	-0.65	0.14	1.10	1.70	1.88	1.76	1.64	1.61	1.55	1.21	0.61
2.96	-1.81	-1.58	-0.91	-0.11	0.97	1.61	1.85	1.74	1.63	1.58	1.52	1.17	0.58
2.98	-2.13	-1.91	-1.19	-0.34	0.86	1.57	1.81	1.72	1.59	1.55	1.47	1.13	0.57
3	-2.46	-2.22	-1.43	-0.49	0.72	1.47	1.79	1.69	1.56	1.50	1.45	1.09	0.54

Table 8.1f: Continuation of table 8.1

Time, ms	Radial position, mm												
	0	10	20	30	40	50	60	70	80	90	100	110	120
3.02	-2.76	-2.52	-1.67	-0.65	0.59	1.37	1.72	1.68	1.55	1.46	1.38	1.05	0.53
3.04	-3.04	-2.79	-1.91	-0.81	0.39	1.28	1.66	1.65	1.56	1.45	1.34	0.99	0.49
3.06	-3.31	-3.05	-2.16	-1.00	0.22	1.18	1.62	1.65	1.54	1.43	1.29	0.92	0.45
3.08	-3.57	-3.31	-2.39	-1.21	0.02	1.10	1.58	1.62	1.50	1.36	1.25	0.88	0.42
3.1	-3.84	-3.56	-2.69	-1.46	-0.12	1.00	1.52	1.60	1.48	1.33	1.19	0.85	0.41
3.12	-4.12	-3.85	-2.92	-1.71	-0.28	0.91	1.46	1.60	1.49	1.32	1.12	0.76	0.37
3.14	-4.42	-4.14	-3.21	-1.90	-0.41	0.82	1.41	1.57	1.48	1.29	1.09	0.69	0.32
3.16	-4.72	-4.46	-3.48	-2.07	-0.48	0.73	1.36	1.54	1.48	1.28	1.04	0.67	0.30
3.18	-5.01	-4.73	-3.73	-2.24	-0.60	0.67	1.29	1.54	1.46	1.25	0.99	0.61	0.25
3.2	-5.28	-4.98	-3.99	-2.43	-0.74	0.56	1.29	1.53	1.46	1.22	0.92	0.54	0.22
3.22	-5.56	-5.25	-4.22	-2.61	-0.93	0.45	1.21	1.54	1.47	1.19	0.86	0.48	0.19
3.24	-5.85	-5.50	-4.45	-2.83	-1.12	0.31	1.11	1.48	1.46	1.20	0.82	0.43	0.16
3.26	-6.12	-5.79	-4.69	-3.04	-1.32	0.19	1.05	1.42	1.43	1.15	0.81	0.40	0.15
3.28	-6.37	-6.06	-4.94	-3.30	-1.51	0.08	1.01	1.40	1.40	1.11	0.73	0.37	0.14
3.3	-6.62	-6.33	-5.20	-3.53	-1.66	-0.03	0.97	1.40	1.40	1.07	0.66	0.29	0.13
3.32	-6.87	-6.60	-5.42	-3.71	-1.80	-0.16	0.91	1.39	1.42	1.05	0.60	0.23	0.09
3.34	-7.12	-6.82	-5.63	-3.87	-1.90	-0.27	0.84	1.34	1.40	1.03	0.57	0.19	0.06
3.36	-7.34	-7.02	-5.83	-4.03	-2.01	-0.36	0.79	1.32	1.39	1.02	0.55	0.16	0.04
3.38	-7.57	-7.21	-6.02	-4.20	-2.13	-0.47	0.73	1.30	1.37	0.99	0.52	0.13	0.01
3.4	-7.81	-7.43	-6.23	-4.37	-2.27	-0.58	0.65	1.30	1.38	0.95	0.45	0.09	0.01
3.42	-8.06	-7.66	-6.46	-4.59	-2.45	-0.67	0.58	1.25	1.37	0.94	0.42	0.05	0.00
3.44	-8.30	-7.89	-6.66	-4.81	-2.66	-0.80	0.50	1.23	1.34	0.91	0.39	0.02	-0.01
3.46	-8.55	-8.12	-6.87	-5.03	-2.88	-0.92	0.41	1.18	1.31	0.86	0.37	0.00	-0.02
3.48	-8.78	-8.33	-7.07	-5.25	-3.08	-1.07	0.32	1.15	1.30	0.84	0.33	-0.03	-0.03
3.5	-9.01	-8.55	-7.27	-5.46	-3.26	-1.22	0.22	1.12	1.27	0.81	0.30	-0.04	-0.05

Table 8.2: Out-of-plane deformation of a 3 mm-thick P-1000 Polyurea plate, exposed to a 0.935 g PETN charge at a 2.5 cm stand-off distance.

Time, ms	Radial position, mm												
	0	10	20	30	40	50	60	70	80	90	100	110	120
	0	10	20	30	40	50	60	70	80	90	100	110	120
0	0.00	0.00	0.00	0.00	0.00	0.00	0.00	0.00	0.00	0.00	0.00	0.00	0.00
0.02	0.00	2.24	0.99	0.63	0.37	0.73	0.39	0.00	0.34	0.00	0.22	0.06	0.09
0.04	7.02	3.65	1.68	1.08	0.86	0.51	0.65	0.47	0.45	0.39	0.33	0.13	0.15
0.06	9.05	5.28	2.37	1.42	1.14	0.82	0.84	0.72	0.68	0.53	0.42	0.26	0.37
0.08	10.99	6.62	3.19	1.84	1.41	1.17	1.06	0.96	0.89	0.72	0.57	0.47	0.60
0.1	12.38	7.94	4.02	2.36	1.69	1.44	1.32	1.18	1.09	0.92	0.79	0.74	0.84
0.12	0.00	9.39	5.16	2.87	2.09	1.66	1.56	1.39	1.30	1.18	1.01	1.16	0.98
0.14	0.00	0.00	0.00	3.37	2.39	2.01	1.74	1.61	1.52	1.44	1.22	1.61	1.05
0.16	0.00	0.00	6.94	0.00	2.85	2.32	1.99	1.74	1.72	1.65	1.44	1.90	1.08
0.18	31.39	0.00	8.54	4.82	3.31	2.46	2.32	1.97	1.95	1.83	1.69	2.26	1.07
0.2	0.00	0.00	10.16	5.77	3.67	2.79	2.49	2.27	2.17	1.99	1.98	2.56	1.06
0.22	18.27	15.75	11.45	6.63	4.14	3.23	2.76	2.45	2.36	2.17	2.36	2.68	1.06
0.24	18.69	16.54	12.66	7.67	4.78	3.48	3.13	2.64	2.57	2.33	2.76	2.79	1.06
0.26	19.23	17.61	13.78	8.74	5.43	3.84	3.39	2.95	2.77	2.49	3.11	2.86	1.08
0.28	19.70	18.17	14.78	9.75	5.98	4.31	3.60	3.27	2.97	2.77	3.46	2.91	1.10
0.3	20.04	18.67	15.78	10.80	6.70	4.67	3.87	3.49	3.10	3.16	3.76	2.97	1.16
0.32	20.32	19.25	16.58	11.82	7.41	5.04	4.26	3.67	3.23	3.52	4.02	3.06	1.19
0.34	20.55	19.76	17.30	12.77	8.19	5.39	4.53	3.85	3.39	3.85	4.19	3.11	1.23
0.36	20.73	20.10	17.88	13.64	9.01	5.71	4.75	4.05	3.65	4.18	4.34	3.17	1.22
0.38	20.89	20.33	18.34	14.44	9.82	6.33	4.98	4.26	3.94	4.52	4.44	3.24	1.23
0.4	20.99	20.50	18.79	15.18	10.64	6.72	5.23	4.43	4.27	4.82	4.53	3.26	1.22
0.42	21.15	20.62	19.17	15.95	11.43	7.40	5.51	4.59	4.58	5.07	4.59	3.27	1.21
0.44	21.25	20.74	19.51	16.46	12.19	8.03	5.80	4.76	4.90	5.31	4.63	3.24	1.21
0.46	21.31	20.82	19.79	17.06	12.92	8.70	6.05	4.92	5.28	5.47	4.68	3.19	1.19
0.48	21.38	20.86	19.98	17.58	13.60	9.25	6.29	5.16	5.67	5.59	4.72	3.13	1.18
0.5	21.39	20.88	20.09	17.83	14.23	9.96	6.62	5.44	5.96	5.72	4.74	3.08	1.17

Table 8.2a: Continuation of table 8.2

Time, ms	Radial position, mm												
	0	10	20	30	40	50	60	70	80	90	100	110	120
	0	10	20	30	40	50	60	70	80	90	100	110	120
0.52	21.36	20.88	20.16	18.07	14.86	10.73	7.00	5.73	6.22	5.90	4.74	3.02	1.17
0.54	21.28	20.82	20.16	18.29	15.40	11.26	7.46	6.10	6.50	6.08	4.73	2.98	1.13
0.56	21.24	20.76	20.16	18.45	15.85	11.70	7.96	6.53	6.72	6.21	4.69	2.95	1.12
0.58	21.14	20.68	20.12	18.53	16.28	12.35	8.60	6.91	6.86	6.30	4.66	2.90	1.09
0.6	21.02	20.57	20.01	18.59	16.63	12.81	9.20	7.25	6.96	6.32	4.65	2.87	1.09
0.62	20.87	20.42	19.89	18.65	16.93	13.36	9.93	7.76	7.08	6.30	4.64	2.84	1.09
0.64	20.70	20.20	19.66	18.73	17.14	13.83	10.76	8.25	7.20	6.28	4.66	2.83	1.08
0.66	20.52	19.99	19.43	18.80	17.27	14.26	11.45	8.78	7.39	6.25	4.66	2.81	1.06
0.68	20.31	19.82	19.29	18.80	17.34	14.66	12.08	9.26	7.57	6.21	4.65	2.80	1.03
0.7	20.08	19.69	19.20	18.76	17.38	15.23	12.78	9.79	7.65	6.16	4.60	2.78	0.98
0.72	19.88	19.47	19.05	18.64	17.42	15.65	13.48	10.44	7.87	6.08	4.56	2.77	0.97
0.74	19.70	19.05	18.87	18.50	17.45	15.97	14.07	10.89	8.08	6.04	4.49	2.75	0.95
0.76	19.52	18.70	18.69	18.32	17.43	16.27	14.63	11.40	8.22	6.00	4.41	2.72	0.94
0.78	19.28	18.46	18.53	18.10	17.40	16.59	15.06	11.90	8.51	5.99	4.34	2.70	0.93
0.8	18.92	18.29	18.34	17.85	17.35	16.88	15.44	12.37	8.90	6.02	4.32	2.67	0.95
0.82	18.44	18.11	18.14	17.61	17.32	17.04	15.74	12.82	9.18	6.07	4.26	2.65	0.99
0.84	18.05	17.91	17.92	17.40	17.28	17.17	16.07	13.24	9.43	6.16	4.15	2.68	1.02
0.86	17.69	17.66	17.67	17.18	17.24	17.24	16.31	13.50	9.77	6.28	4.04	2.66	1.07
0.88	17.29	17.41	17.38	16.97	17.21	17.32	16.46	13.81	10.12	6.44	3.94	2.60	1.11
0.9	16.93	17.18	17.03	16.75	17.18	17.36	16.57	14.08	10.35	6.59	3.89	2.53	1.16
0.92	16.68	16.91	16.64	16.54	17.15	17.41	16.67	14.24	10.60	6.69	3.85	2.47	1.17
0.94	16.50	16.64	16.32	16.37	17.13	17.42	16.71	14.33	10.91	6.84	3.88	2.41	1.18
0.96	16.33	16.31	16.10	16.26	17.09	17.43	16.72	14.38	11.09	7.19	3.98	2.33	1.15
0.98	16.21	15.84	15.84	16.13	17.03	17.35	16.66	14.38	11.21	7.42	4.10	2.29	1.08
1	16.09	15.30	15.47	15.99	16.92	17.17	16.48	14.33	11.33	7.53	4.22	2.23	1.01

Table 8.2b: Continuation of table 8.2

Time, ms	Radial position, mm												
	0	10	20	30	40	50	60	70	80	90	100	110	120
	0	10	20	30	40	50	60	70	80	90	100	110	120
1.02	15.93	14.90	15.21	15.83	16.78	16.91	16.23	14.29	11.49	7.78	4.38	2.21	0.93
1.04	15.68	14.65	15.01	15.68	16.64	16.70	16.01	14.20	11.62	8.12	4.73	2.22	0.84
1.06	15.27	14.34	14.68	15.59	16.49	16.53	15.78	14.07	11.69	8.29	4.99	2.26	0.76
1.08	14.76	13.87	14.37	15.48	16.32	16.27	15.46	13.92	11.68	8.44	5.12	2.36	0.68
1.1	14.22	13.59	14.18	15.38	16.14	15.94	15.18	13.77	11.57	8.67	5.38	2.48	0.27
1.12	13.68	13.34	14.00	15.23	15.91	15.65	14.95	13.60	11.52	8.87	5.60	2.61	0.27
1.14	13.09	13.02	13.83	15.03	15.68	15.36	14.67	13.36	11.47	8.97	5.81	2.73	0.26
1.16	12.61	12.64	13.64	14.81	15.41	15.00	14.30	13.06	11.41	9.09	6.15	2.88	0.37
1.18	12.01	12.33	13.46	14.62	15.14	14.63	13.97	12.78	11.33	9.20	6.36	3.06	0.45
1.2	11.43	12.06	13.29	14.42	14.85	14.31	13.65	12.52	11.21	9.28	6.47	3.22	0.52
1.22	11.01	11.76	13.14	14.20	14.54	13.98	13.22	12.19	11.08	9.33	6.64	3.47	0.66
1.24	10.65	11.47	12.99	13.97	14.21	13.60	12.83	11.86	10.92	9.35	6.83	3.84	1.11
1.26	10.32	11.19	12.85	13.68	13.84	13.22	12.47	11.55	10.77	9.36	6.98	4.09	1.31
1.28	10.03	10.98	12.69	13.41	13.44	12.87	12.04	11.26	10.62	9.34	7.09	4.36	1.49
1.3	9.81	10.79	12.52	13.14	13.05	12.49	11.61	10.94	10.48	9.31	7.19	4.63	1.68
1.32	9.63	10.62	12.33	12.89	12.67	12.05	11.24	10.64	10.30	9.26	7.35	4.79	1.79
1.34	9.52	10.46	12.10	12.62	12.28	11.64	10.85	10.35	10.11	9.19	7.51	5.01	1.92
1.36	9.42	10.31	11.84	12.30	11.84	11.23	10.41	10.06	9.92	9.12	7.67	5.28	2.07
1.38	9.37	10.17	11.57	11.95	11.40	10.76	10.04	9.77	9.72	9.02	7.78	5.51	2.14
1.4	9.35	10.05	11.28	11.61	11.03	10.30	9.71	9.50	9.51	8.93	7.88	5.71	2.19
1.42	9.33	9.91	10.99	11.27	10.67	9.85	9.26	9.24	9.27	8.85	7.98	5.88	2.27
1.44	9.34	9.77	10.70	10.91	10.27	9.34	8.85	8.98	9.02	8.77	8.06	6.02	2.36
1.46	9.38	9.65	10.45	10.53	9.83	8.81	8.55	8.69	8.79	8.69	8.14	6.11	2.42
1.48	9.41	9.56	10.20	10.13	9.40	8.37	8.24	8.41	8.57	8.62	8.20	6.18	2.45
1.5	9.47	9.49	9.94	9.76	8.97	7.95	7.84	8.14	8.36	8.52	8.25	6.20	2.48

Table 8.2c: Continuation of table 8.2

Time, ms	Radial position, mm												
	0	10	20	30	40	50	60	70	80	90	100	110	120
	0	10	20	30	40	50	60	70	80	90	100	110	120
1.52	9.55	9.44	9.64	9.38	8.49	7.51	7.46	7.85	8.14	8.43	8.26	6.21	2.49
1.54	9.63	9.39	9.32	8.96	7.97	7.11	7.16	7.56	7.92	8.34	8.25	6.18	2.49
1.56	9.74	9.32	8.99	8.49	7.50	6.77	6.92	7.23	7.68	8.24	8.22	6.14	2.46
1.58	9.84	9.26	8.70	8.02	7.09	6.47	6.62	6.86	7.45	8.16	8.17	6.09	2.41
1.6	9.91	9.18	8.45	7.56	6.65	6.13	6.25	6.50	7.24	8.05	8.10	6.03	2.35
1.62	9.95	9.09	8.20	7.09	6.18	5.75	5.81	6.14	7.05	7.94	8.01	5.94	2.28
1.64	9.98	9.00	7.93	6.63	5.77	5.36	5.43	5.82	6.87	7.85	7.91	5.83	2.20
1.66	9.99	8.90	7.61	6.21	5.37	5.03	5.11	5.51	6.68	7.74	7.81	5.70	2.12
1.68	9.99	8.79	7.27	5.78	4.93	4.69	4.79	5.18	6.47	7.64	7.67	5.55	2.07
1.7	9.95	8.68	6.92	5.30	4.53	4.27	4.36	4.86	6.26	7.51	7.53	5.40	2.01
1.72	9.92	8.56	6.62	4.90	4.15	3.86	3.96	4.59	6.10	7.40	7.36	5.28	1.96
1.74	9.85	8.42	6.29	4.54	3.74	3.51	3.66	4.34	5.94	7.26	7.22	5.16	1.91
1.76	9.77	8.26	5.96	4.11	3.33	3.14	3.35	4.08	5.78	7.13	7.06	4.99	1.85
1.78	9.65	8.07	5.67	3.68	2.97	2.67	2.91	3.84	5.59	7.00	6.91	4.77	1.76
1.8	9.50	7.84	5.39	3.35	2.59	2.28	2.58	3.62	5.40	6.84	6.68	4.55	1.38
1.82	9.31	7.57	5.09	3.04	2.16	1.91	2.33	3.42	5.23	6.67	6.41	4.35	1.31
1.84	9.11	7.25	4.78	2.67	1.75	1.45	1.95	3.23	5.09	6.48	6.19	4.18	1.25
1.86	8.88	6.94	4.45	2.30	1.37	1.02	1.59	3.02	4.94	6.28	5.97	3.97	1.43
1.88	8.62	6.65	4.15	1.95	0.96	0.67	1.35	2.79	4.74	6.08	5.71	3.73	1.39
1.9	8.31	6.36	3.84	1.66	0.52	0.24	1.06	2.60	4.57	5.86	5.39	3.51	1.31
1.92	7.88	6.08	3.53	1.38	0.13	-0.20	0.69	2.42	4.40	5.60	5.10	3.31	1.25
1.94	7.41	5.74	3.23	1.11	-0.24	-0.54	0.39	2.27	4.25	5.36	4.86	3.11	1.19
1.96	6.99	5.36	2.96	0.83	-0.61	-0.89	0.16	2.09	4.10	5.13	4.56	2.90	1.12
1.98	6.60	4.93	2.70	0.52	-0.99	-1.31	-0.11	1.89	3.94	4.86	4.23	2.72	1.06

Table 8.2d: Continuation of table 8.2

Time, ms	Radial position, mm												
	0	10	20	30	40	50	60	70	80	90	100	110	120
	0	10	20	30	40	50	60	70	80	90	100	110	120
2	6.09	4.56	2.45	0.17	-1.36	-1.68	-0.43	1.71	3.74	4.55	3.94	2.54	1.00
2.02	5.51	4.20	2.17	-0.19	-1.76	-1.98	-0.72	1.53	3.54	4.27	3.68	2.34	0.92
2.04	5.04	3.80	1.85	-0.55	-2.16	-2.29	-0.95	1.39	3.34	4.01	3.37	2.14	0.86
2.06	4.61	3.34	1.53	-0.90	-2.55	-2.64	-1.16	1.25	3.14	3.76	3.03	1.93	0.80
2.08	4.06	2.92	1.19	-1.20	-2.93	-3.05	-1.36	1.10	2.94	3.45	2.73	1.76	0.73
2.1	3.49	2.56	0.84	-1.49	-3.24	-3.42	-1.62	0.96	2.74	3.13	2.46	1.57	0.68
2.12	3.05	2.20	0.51	-1.80	-3.58	-3.73	-1.86	0.78	2.53	2.83	2.19	1.37	0.61
2.14	2.54	1.72	0.16	-2.15	-3.93	-4.01	-2.07	0.58	2.31	2.56	1.87	1.16	0.56
2.16	1.93	1.23	-0.21	-2.53	-4.26	-4.30	-2.27	0.37	2.07	2.28	1.56	0.96	0.50
2.18	1.42	0.81	-0.60	-2.90	-4.60	-4.57	-2.48	0.17	1.82	1.96	1.30	0.78	0.43
2.2	1.05	0.37	-0.99	-3.25	-4.92	-4.85	-2.66	-0.02	1.57	1.62	1.04	0.60	0.35
2.22	0.67	-0.14	-1.39	-3.62	-5.24	-5.10	-2.87	-0.20	1.30	1.32	0.75	0.42	0.26
2.24	0.15	-0.65	-1.85	-4.05	-5.55	-5.30	-3.09	-0.40	1.06	1.04	0.45	0.22	0.20
2.26	-0.38	-1.04	-2.33	-4.46	-5.86	-5.49	-3.31	-0.61	0.81	0.79	0.18	0.00	0.13
2.28	-0.82	-1.40	-2.79	-4.79	-6.14	-5.69	-3.49	-0.84	0.54	0.48	-0.04	-0.20	0.07
2.3	-1.20	-1.85	-3.22	-5.11	-6.44	-5.88	-3.67	-1.11	0.26	0.15	-0.28	-0.37	0.01
2.32	-1.58	-2.33	-3.67	-5.56	-6.71	-6.09	-3.86	-1.37	-0.04	-0.15	-0.54	-0.52	-0.04
2.34	-2.02	-2.77	-4.12	-5.96	-7.00	-6.29	-4.04	-1.66	-0.35	-0.40	-0.80	-0.69	-0.10
2.36	-2.44	-3.19	-4.53	-6.28	-7.25	-6.49	-4.21	-1.93	-0.65	-0.66	-1.06	-0.84	-0.17
2.38	-2.78	-3.64	-4.95	-6.62	-7.51	-6.65	-4.39	-2.20	-0.95	-0.92	-1.30	-1.00	-0.21
2.4	-3.12	-4.09	-5.39	-7.07	-7.76	-6.82	-4.57	-2.45	-1.24	-1.22	-1.52	-1.19	-0.26
2.42	-3.52	-4.50	-5.85	-7.49	-8.03	-6.98	-4.78	-2.69	-1.53	-1.52	-1.72	-1.37	-0.31
2.44	-4.02	-4.84	-6.32	-7.83	-8.29	-7.17	-4.98	-2.93	-1.82	-1.79	-1.93	-1.54	-0.35
2.46	-4.48	-5.20	-6.79	-8.19	-8.56	-7.34	-5.20	-3.21	-2.13	-2.04	-2.14	-1.70	-0.40
2.48	-4.81	-5.63	-7.29	-8.64	-8.82	-7.54	-5.41	-3.45	-2.44	-2.28	-2.37	-1.83	-0.44

Table 8.2e: Continuation of table 8.2

Time, ms	Radial position, mm												
	0	10	20	30	40	50	60	70	80	90	100	110	120
	0	10	20	30	40	50	60	70	80	90	100	110	120
2.5	-5.08	-6.11	-7.76	-9.07	-9.05	-7.75	-5.62	-3.70	-2.73	-2.56	-2.59	-1.94	-0.47
2.52	-5.41	-6.55	-8.17	-9.41	-9.31	-7.96	-5.84	-3.94	-3.00	-2.86	-2.81	-2.04	-0.48
2.54	-5.86	-6.98	-8.61	-9.75	-9.60	-8.17	-6.05	-4.21	-3.28	-3.18	-3.01	-2.17	-0.50
2.56	-6.31	-7.37	-9.02	-10.17	-9.87	-8.35	-6.25	-4.52	-3.61	-3.48	-3.20	-2.27	-0.53
2.58	-6.67	-7.81	-9.42	-10.57	-10.11	-8.53	-6.46	-4.85	-3.95	-3.76	-3.39	-2.35	-0.55
2.6	-7.05	-8.24	-9.83	-10.89	-10.35	-8.72	-6.68	-5.17	-4.27	-4.04	-3.60	-2.46	-0.58
2.62	-7.51	-8.62	-10.29	-11.21	-10.58	-8.92	-6.91	-5.44	-4.58	-4.33	-3.80	-2.58	-0.60
2.64	-8.06	-9.06	-10.76	-11.58	-10.84	-9.12	-7.13	-5.70	-4.87	-4.65	-4.00	-2.69	-0.62
2.66	-8.50	-9.60	-11.22	-11.96	-11.12	-9.32	-7.35	-5.96	-5.18	-4.96	-4.21	-2.79	-0.63
2.68	-8.84	-10.14	-11.69	-12.29	-11.38	-9.53	-7.54	-6.19	-5.52	-5.25	-4.40	-2.90	-0.66
2.7	-9.28	-10.59	-12.12	-12.61	-11.62	-9.72	-7.72	-6.47	-5.85	-5.51	-4.62	-2.97	-0.68
2.72	-9.87	-11.06	-12.54	-12.94	-11.83	-9.91	-7.91	-6.76	-6.15	-5.76	-4.84	-3.06	-0.69
2.74	-10.35	-11.59	-12.98	-13.28	-12.05	-10.11	-8.10	-7.03	-6.43	-6.01	-5.03	-3.13	-0.70
2.76	-10.79	-12.03	-13.39	-13.62	-12.27	-10.32	-8.32	-7.28	-6.72	-6.32	-5.19	-3.18	-0.71
2.78	-11.38	-12.47	-13.79	-13.97	-12.51	-10.51	-8.57	-7.54	-7.02	-6.60	-5.36	-3.21	-0.71
2.8	-12.02	-12.98	-14.20	-14.28	-12.77	-10.74	-8.85	-7.81	-7.33	-6.85	-5.51	-3.26	-0.71
2.82	-12.47	-13.57	-14.65	-14.59	-13.02	-10.96	-9.14	-8.11	-7.65	-7.07	-5.65	-3.30	-0.73
2.84	-12.92	-14.10	-15.09	-14.88	-13.24	-11.19	-9.44	-8.45	-7.96	-7.32	-5.79	-3.35	-0.76
2.86	-13.62	-14.63	-15.52	-15.16	-13.48	-11.40	-9.72	-8.79	-8.27	-7.56	-5.95	-3.39	-0.75
2.88	-14.17	-15.21	-15.93	-15.42	-13.71	-11.65	-9.94	-9.10	-8.59	-7.82	-6.10	-3.44	-0.77
2.9	-14.69	-15.70	-16.35	-15.71	-13.95	-11.90	-10.17	-9.36	-8.89	-8.10	-6.25	-3.48	-0.77
2.92	-15.47	-16.13	-16.74	-16.00	-14.19	-12.15	-10.37	-9.61	-9.21	-8.37	-6.40	-3.51	-0.79
2.94	-16.07	-16.68	-17.10	-16.28	-14.45	-12.39	-10.58	-9.87	-9.52	-8.61	-6.53	-3.56	-0.79
2.96	-16.50	-17.23	-17.47	-16.54	-14.71	-12.67	-10.84	-10.14	-9.82	-8.84	-6.66	-3.60	-0.80
2.98	-17.19	-17.71	-17.80	-16.81	-14.96	-12.91	-11.16	-10.49	-10.11	-9.04	-6.77	-3.64	-0.81
3	-17.80	-18.29	-18.15	-17.08	-15.21	-13.15	-11.50	-10.88	-10.39	-9.24	-6.88	-3.68	-0.82

Table 8.2f: Continuation of table 8.2

Time, ms	Radial position, mm												
	0	10	20	30	40	50	60	70	80	90	100	110	120
	0	10	20	30	40	50	60	70	80	90	100	110	120
3.02	-18.43	-18.94	-18.51	-17.33	-15.43	-13.41	-11.88	-11.24	-10.65	-9.44	-6.97	-3.74	-0.85
3.04	-19.18	-19.42	-18.89	-17.59	-15.64	-13.67	-12.25	-11.60	-10.92	-9.63	-7.06	-3.78	-0.86
3.06	-19.78	-19.91	-19.22	-17.86	-15.87	-13.95	-12.56	-11.93	-11.25	-9.80	-7.14	-3.81	-0.86
3.08	-20.25	-20.46	-19.53	-18.10	-16.09	-14.25	-12.84	-12.26	-11.56	-9.98	-7.20	-3.86	-0.88
3.1	-20.77	-20.90	-19.87	-18.33	-16.31	-14.54	-13.15	-12.59	-11.83	-10.16	-7.31	-3.88	-0.90
3.12	-21.38	-21.32	-20.21	-18.54	-16.54	-14.82	-13.51	-12.97	-12.11	-10.34	-7.38	-3.95	-0.89
3.14	-22.01	-21.83	-20.53	-18.72	-16.76	-15.16	-13.94	-13.33	-12.37	-10.50	-7.45	-4.01	-0.94
3.16	-22.59	-22.29	-20.81	-18.95	-16.99	-15.47	-14.32	-13.66	-12.63	-10.66	-7.54	-4.07	-0.98
3.18	-23.08	-22.72	-21.09	-19.17	-17.25	-15.79	-14.67	-13.99	-12.92	-10.81	-7.62	-4.10	-1.00
3.2	-23.54	-23.14	-21.45	-19.40	-17.48	-16.15	-15.06	-14.38	-13.19	-10.94	-7.67	-4.15	-1.02
3.22	-23.93	-23.54	-21.74	-19.63	-17.72	-16.49	-15.52	-14.79	-13.42	-11.06	-7.73	-4.18	-1.06
3.24	-24.28	-23.93	-22.02	-19.83	-17.97	-16.80	-16.00	-15.19	-13.64	-11.19	-7.80	-4.25	-1.09
3.26	-24.63	-24.26	-22.27	-20.02	-18.20	-17.13	-16.41	-15.52	-13.87	-11.30	-7.87	-4.29	-1.13
3.28	-25.00	-24.58	-22.51	-20.23	-18.45	-17.44	-16.74	-15.87	-14.10	-11.41	-7.92	-4.31	-1.16
3.3	-25.38	-24.84	-22.78	-20.46	-18.75	-17.87	-17.07	-16.24	-14.35	-11.52	-8.00	-4.34	-1.17
3.32	-25.70	-25.09	-23.05	-20.73	-19.07	-18.33	-17.52	-16.58	-14.58	-11.63	-8.06	-4.40	-1.20
3.34	-25.97	-25.32	-23.33	-21.00	-19.41	-18.75	-18.03	-16.92	-14.79	-11.71	-8.15	-4.43	-1.23
3.36	-26.18	-25.54	-23.56	-21.25	-19.74	-19.14	-18.50	-17.21	-14.98	-11.82	-8.20	-4.49	-1.25
3.38	-26.32	-25.70	-23.77	-21.50	-20.05	-19.46	-18.87	-17.53	-15.14	-11.91	-8.26	-4.53	-1.31
3.4	-26.43	-25.87	-23.96	-21.75	-20.36	-19.80	-19.21	-17.82	-15.30	-12.00	-8.31	-4.58	-1.17
3.42	-26.53	-26.03	-24.14	-22.07	-20.70	-20.20	-19.56	-18.12	-15.46	-12.11	-8.37	-4.61	-1.34
3.44	-26.59	-26.15	-24.33	-22.38	-21.08	-20.67	-19.95	-18.42	-15.63	-12.20	-8.41	-4.64	-1.34
3.46	-26.67	-26.26	-24.50	-22.67	-21.52	-21.13	-20.34	-18.69	-15.77	-12.28	-8.46	-4.67	-1.37
3.48	-26.69	-26.35	-24.71	-22.94	-21.93	-21.52	-20.71	-18.93	-15.90	-12.35	-8.51	-4.71	-1.40
3.5	-26.72	-26.42	-24.90	-23.26	-22.32	-21.87	-21.06	-19.15	-16.04	-12.43	-8.56	-4.75	-1.42

Table 8.3: Out-of-plane deformation of a 3 mm-thick P-1000 Polyurea plate, exposed to a 0.947 g PETN charge at a 12.5 cm stand-off distance.

Time, ms	Radial position, mm												
	0	10	20	30	40	50	60	70	80	90	100	110	120
	0	10	20	30	40	50	60	70	80	90	100	110	120
-0.04	0.01	0.00	0.02	0.01	0.01	0.02	0.01	0.01	0.03	0.01	0.01	0.02	0.03
-0.02	0.01	0.00	0.01	0.00	0.01	0.01	0.01	0.00	0.01	0.01	0.01	0.00	0.01
0	0.03	0.03	0.04	0.01	0.01	0.01	0.01	0.00	0.01	0.00	0.00	0.01	0.00
0.02	0.17	0.16	0.19	0.16	0.14	0.08	0.05	0.04	0.01	0.00	0.00	0.00	-0.01
0.04	0.43	0.37	0.44	0.38	0.36	0.25	0.18	0.18	0.11	0.06	0.03	0.00	0.00
0.06	0.76	0.65	0.71	0.62	0.61	0.44	0.34	0.36	0.28	0.19	0.10	0.06	0.02
0.08	1.12	0.96	0.96	0.88	0.86	0.67	0.53	0.55	0.45	0.34	0.23	0.14	0.09
0.1	1.44	1.28	1.21	1.14	1.06	0.91	0.76	0.74	0.63	0.50	0.38	0.27	0.24
0.12	1.73	1.57	1.50	1.41	1.27	1.14	1.01	0.93	0.81	0.67	0.54	0.41	0.43
0.14	1.99	1.85	1.83	1.67	1.51	1.38	1.23	1.13	1.00	0.84	0.72	0.59	0.64
0.16	2.25	2.12	2.16	1.94	1.76	1.60	1.43	1.32	1.17	1.02	0.92	0.82	0.81
0.18	2.55	2.40	2.46	2.19	2.04	1.83	1.62	1.54	1.36	1.21	1.11	1.10	0.97
0.2	2.86	2.70	2.73	2.44	2.31	2.08	1.81	1.77	1.57	1.42	1.30	1.42	1.07
0.22	3.13	2.99	2.95	2.70	2.58	2.35	2.05	2.03	1.79	1.62	1.50	1.68	1.14
0.24	3.35	3.26	3.17	2.94	2.84	2.61	2.30	2.28	2.02	1.80	1.72	1.88	1.17
0.26	3.52	3.46	3.37	3.19	3.07	2.86	2.55	2.50	2.26	1.98	1.99	2.08	1.20
0.28	3.69	3.68	3.59	3.44	3.27	3.08	2.81	2.70	2.46	2.13	2.29	2.28	1.22
0.3	3.92	3.90	3.86	3.69	3.50	3.30	3.07	2.88	2.63	2.32	2.56	2.44	1.22
0.32	4.25	4.17	4.16	3.94	3.74	3.52	3.30	3.08	2.79	2.52	2.80	2.55	1.22
0.34	4.74	4.54	4.47	4.20	4.02	3.74	3.50	3.31	2.92	2.73	3.03	2.63	1.22
0.36	5.19	4.93	4.74	4.46	4.27	3.94	3.67	3.53	3.05	2.98	3.25	2.69	1.21
0.38	5.56	5.27	5.02	4.76	4.49	4.18	3.83	3.71	3.18	3.21	3.46	2.75	1.19
0.4	5.84	5.58	5.35	5.04	4.70	4.40	4.03	3.84	3.33	3.45	3.62	2.79	1.17
0.42	6.13	5.91	5.70	5.29	4.94	4.61	4.29	3.95	3.49	3.68	3.79	2.82	1.16
0.44	6.47	6.28	6.00	5.53	5.21	4.81	4.53	4.04	3.67	3.92	3.93	2.84	1.16
0.46	6.83	6.64	6.27	5.76	5.44	5.00	4.69	4.14	3.86	4.17	4.05	2.85	1.15
0.48	7.12	6.94	6.52	5.99	5.63	5.18	4.81	4.24	4.08	4.39	4.14	2.85	1.14
0.5	7.34	7.18	6.79	6.24	5.78	5.36	4.93	4.37	4.33	4.59	4.24	2.86	1.13

Table 8.3a: Continuation of table 8.3

Time, ms	Radial position, mm												
	0	10	20	30	40	50	60	70	80	90	100	110	120
	0	10	20	30	40	50	60	70	80	90	100	110	120
0.52	7.53	7.38	7.05	6.47	5.92	5.55	5.05	4.51	4.58	4.79	4.33	2.87	1.13
0.54	7.75	7.56	7.31	6.67	6.06	5.74	5.17	4.68	4.83	4.99	4.41	2.88	1.12
0.56	7.99	7.75	7.55	6.84	6.21	5.91	5.28	4.84	5.07	5.17	4.46	2.87	1.11
0.58	8.25	7.95	7.76	6.98	6.39	6.06	5.37	5.02	5.29	5.32	4.50	2.87	1.12
0.6	8.51	8.17	7.93	7.13	6.59	6.19	5.45	5.18	5.48	5.45	4.52	2.86	1.12
0.62	8.75	8.38	8.06	7.29	6.81	6.28	5.51	5.34	5.69	5.54	4.52	2.85	1.10
0.64	8.95	8.59	8.19	7.46	7.03	6.35	5.58	5.49	5.88	5.64	4.52	2.82	1.11
0.66	9.14	8.78	8.30	7.63	7.22	6.40	5.64	5.65	6.06	5.71	4.51	2.79	1.09
0.68	9.31	8.97	8.42	7.82	7.37	6.43	5.71	5.81	6.22	5.75	4.48	2.76	1.07
0.7	9.47	9.12	8.53	8.03	7.48	6.46	5.79	5.97	6.34	5.79	4.45	2.71	1.05
0.72	9.63	9.25	8.67	8.25	7.58	6.50	5.89	6.15	6.46	5.82	4.40	2.66	1.02
0.74	9.80	9.37	8.83	8.48	7.67	6.55	6.02	6.33	6.57	5.82	4.36	2.60	0.99
0.76	9.99	9.50	9.04	8.69	7.76	6.61	6.19	6.53	6.66	5.81	4.31	2.54	0.96
0.78	10.19	9.65	9.29	8.89	7.84	6.70	6.38	6.72	6.74	5.78	4.26	2.47	0.94
0.8	10.36	9.81	9.54	9.07	7.92	6.80	6.55	6.90	6.81	5.76	4.22	2.41	0.91
0.82	10.48	10.00	9.77	9.23	8.00	6.96	6.72	7.06	6.89	5.73	4.16	2.36	0.89
0.84	10.53	10.19	9.97	9.37	8.07	7.12	6.90	7.21	6.95	5.70	4.11	2.32	0.88
0.86	10.53	10.40	10.16	9.49	8.16	7.31	7.10	7.36	7.01	5.67	4.06	2.29	0.86
0.88	10.52	10.57	10.37	9.58	8.25	7.51	7.33	7.52	7.05	5.65	4.02	2.26	0.87
0.9	10.53	10.72	10.56	9.64	8.34	7.71	7.60	7.70	7.09	5.62	3.97	2.25	0.87
0.92	10.60	10.87	10.74	9.66	8.45	7.92	7.87	7.85	7.12	5.59	3.92	2.23	0.87
0.94	10.72	11.02	10.89	9.68	8.56	8.15	8.06	8.00	7.14	5.56	3.89	2.22	0.88
0.96	10.94	11.17	10.99	9.68	8.66	8.36	8.23	8.09	7.16	5.52	3.83	2.22	0.88
0.98	11.18	11.31	11.04	9.69	8.77	8.57	8.39	8.19	7.16	5.48	3.80	2.21	0.89
1	11.45	11.42	11.05	9.71	8.88	8.77	8.58	8.27	7.17	5.44	3.77	2.21	0.89

Table 8.3b: Continuation of table 8.3

Time, ms	Radial position, mm												
	0	10	20	30	40	50	60	70	80	90	100	110	120
	0	10	20	30	40	50	60	70	80	90	100	110	120
1.02	11.70	11.51	11.03	9.74	9.01	8.95	8.79	8.34	7.16	5.41	3.74	2.22	0.88
1.04	11.96	11.59	10.97	9.75	9.16	9.14	8.98	8.39	7.15	5.39	3.72	2.21	0.87
1.06	12.27	11.67	10.90	9.76	9.31	9.35	9.14	8.43	7.13	5.38	3.71	2.20	0.87
1.08	12.61	11.75	10.81	9.78	9.45	9.54	9.24	8.46	7.11	5.35	3.69	2.19	0.86
1.1	12.87	11.80	10.72	9.81	9.60	9.71	9.33	8.47	7.07	5.34	3.69	2.18	0.84
1.12	13.01	11.81	10.65	9.85	9.75	9.86	9.38	8.48	7.02	5.32	3.68	2.16	0.82
1.14	13.08	11.79	10.57	9.91	9.92	9.99	9.43	8.46	6.99	5.29	3.65	2.15	0.81
1.16	13.06	11.74	10.50	9.98	10.08	10.13	9.46	8.44	6.92	5.27	3.64	2.12	0.80
1.18	12.97	11.66	10.47	10.06	10.25	10.26	9.50	8.40	6.83	5.22	3.62	2.09	0.78
1.2	12.80	11.57	10.45	10.15	10.42	10.38	9.51	8.37	6.76	5.15	3.58	2.08	0.76
1.22	12.53	11.44	10.45	10.25	10.59	10.52	9.54	8.31	6.66	5.07	3.53	2.03	0.77
1.24	12.17	11.29	10.47	10.37	10.74	10.62	9.53	8.25	6.57	4.98	3.49	1.99	0.76
1.26	11.85	11.14	10.50	10.48	10.89	10.71	9.51	8.16	6.48	4.88	3.45	1.94	0.73
1.28	11.53	10.98	10.53	10.60	11.01	10.77	9.48	8.06	6.40	4.80	3.38	1.90	0.72
1.3	11.07	10.78	10.58	10.73	11.10	10.81	9.44	7.95	6.31	4.73	3.32	1.86	0.72
1.32	10.48	10.50	10.61	10.86	11.17	10.84	9.39	7.83	6.23	4.66	3.25	1.84	0.70
1.34	10.01	10.23	10.65	11.00	11.22	10.82	9.33	7.72	6.15	4.61	3.18	1.80	0.72
1.36	9.66	9.99	10.67	11.13	11.24	10.80	9.26	7.61	6.05	4.54	3.10	1.78	0.72
1.38	9.25	9.77	10.69	11.25	11.27	10.75	9.19	7.53	5.97	4.49	3.02	1.76	0.73
1.4	8.85	9.56	10.72	11.36	11.28	10.67	9.12	7.45	5.88	4.43	2.96	1.74	0.73
1.42	8.56	9.38	10.75	11.46	11.28	10.56	9.04	7.38	5.80	4.36	2.89	1.71	0.72
1.44	8.36	9.20	10.79	11.54	11.28	10.45	8.94	7.32	5.72	4.29	2.83	1.68	0.72
1.46	8.19	9.06	10.80	11.60	11.28	10.32	8.82	7.24	5.64	4.22	2.79	1.66	0.70
1.48	8.10	8.96	10.81	11.63	11.27	10.19	8.67	7.17	5.56	4.14	2.76	1.64	0.69
1.5	8.06	8.91	10.79	11.64	11.23	10.07	8.53	7.08	5.48	4.05	2.71	1.62	0.67

Table 8.3c: Continuation of table 8.3

Time, ms	Radial position, mm												
	0	10	20	30	40	50	60	70	80	90	100	110	120
	0	10	20	30	40	50	60	70	80	90	100	110	120
1.52	8.11	8.90	10.77	11.64	11.18	9.95	8.43	6.98	5.39	3.96	2.67	1.61	0.66
1.54	8.19	8.93	10.73	11.61	11.12	9.83	8.30	6.88	5.31	3.86	2.63	1.58	0.65
1.56	8.33	9.00	10.70	11.55	11.05	9.71	8.21	6.74	5.23	3.77	2.60	1.58	0.63
1.58	8.52	9.10	10.66	11.48	10.96	9.59	8.06	6.62	5.14	3.70	2.55	1.54	0.61
1.6	8.79	9.24	10.62	11.40	10.85	9.47	7.91	6.49	5.05	3.62	2.53	1.55	0.60
1.62	9.05	9.41	10.59	11.28	10.73	9.35	7.74	6.40	4.96	3.57	2.49	1.53	0.60
1.64	9.36	9.61	10.59	11.14	10.59	9.22	7.57	6.28	4.88	3.54	2.47	1.49	0.60
1.66	9.67	9.79	10.59	10.99	10.42	9.09	7.40	6.15	4.80	3.50	2.43	1.46	0.60
1.68	9.99	9.98	10.58	10.83	10.22	8.95	7.24	6.02	4.73	3.49	2.41	1.43	0.60
1.7	10.32	10.20	10.59	10.64	10.02	8.80	7.10	5.88	4.65	3.47	2.39	1.39	0.60
1.72	10.72	10.44	10.59	10.43	9.80	8.66	6.96	5.75	4.57	3.45	2.37	1.38	0.61
1.74	11.16	10.71	10.61	10.23	9.61	8.50	6.86	5.61	4.49	3.44	2.35	1.36	0.60
1.76	11.55	10.97	10.62	10.04	9.43	8.36	6.74	5.49	4.42	3.41	2.34	1.35	0.59
1.78	11.86	11.18	10.64	9.86	9.25	8.22	6.64	5.37	4.36	3.38	2.32	1.33	0.58
1.8	12.13	11.37	10.64	9.69	9.05	8.05	6.54	5.26	4.29	3.36	2.30	1.33	0.57
1.82	12.51	11.56	10.64	9.51	8.81	7.88	6.45	5.16	4.23	3.33	2.31	1.33	0.56
1.84	12.91	11.78	10.62	9.34	8.54	7.68	6.34	5.08	4.16	3.28	2.30	1.34	0.55
1.86	13.18	12.00	10.61	9.17	8.32	7.46	6.24	5.01	4.10	3.23	2.30	1.36	0.54
1.88	13.37	12.15	10.57	9.03	8.12	7.26	6.09	4.94	4.04	3.19	2.31	1.37	0.52
1.9	13.52	12.27	10.55	8.90	7.93	7.07	5.92	4.87	3.98	3.15	2.32	1.37	0.52
1.92	13.67	12.35	10.52	8.78	7.73	6.89	5.74	4.82	3.92	3.11	2.33	1.39	0.52
1.94	13.77	12.42	10.49	8.65	7.50	6.68	5.59	4.76	3.85	3.06	2.33	1.40	0.52
1.96	13.83	12.45	10.46	8.52	7.27	6.43	5.46	4.69	3.80	3.03	2.33	1.42	0.52
1.98	13.85	12.45	10.43	8.39	7.07	6.21	5.34	4.63	3.75	2.99	2.32	1.42	0.54
2	13.78	12.43	10.38	8.29	6.90	6.02	5.21	4.54	3.69	2.98	2.31	1.43	0.55

Table 8.3d: Continuation of table 8.3

Time, ms	Radial position, mm												
	0	10	20	30	40	50	60	70	80	90	100	110	120
	0	10	20	30	40	50	60	70	80	90	100	110	120
2.02	13.67	12.37	10.33	8.18	6.73	5.85	5.05	4.45	3.64	2.94	2.31	1.44	0.55
2.04	13.53	12.28	10.26	8.08	6.56	5.64	4.84	4.35	3.60	2.92	2.28	1.45	0.57
2.06	13.37	12.18	10.20	7.99	6.39	5.43	4.67	4.26	3.57	2.90	2.26	1.43	0.58
2.08	13.20	12.05	10.12	7.90	6.21	5.18	4.51	4.15	3.54	2.89	2.23	1.43	0.58
2.1	13.03	11.89	10.04	7.81	6.05	4.98	4.36	4.04	3.50	2.88	2.21	1.42	0.59
2.12	12.79	11.70	9.95	7.72	5.88	4.79	4.21	3.90	3.48	2.87	2.19	1.41	0.61
2.14	12.48	11.46	9.84	7.61	5.73	4.61	4.03	3.78	3.43	2.85	2.16	1.40	0.61
2.16	12.07	11.19	9.70	7.51	5.56	4.41	3.85	3.66	3.40	2.83	2.13	1.39	0.62
2.18	11.68	10.94	9.56	7.37	5.42	4.22	3.66	3.54	3.36	2.80	2.09	1.36	0.62
2.2	11.37	10.71	9.37	7.22	5.29	4.05	3.46	3.43	3.32	2.78	2.05	1.32	0.60
2.22	11.11	10.48	9.18	7.09	5.19	3.88	3.29	3.33	3.28	2.76	2.02	1.30	0.58
2.24	10.82	10.21	8.98	6.98	5.12	3.76	3.12	3.23	3.24	2.73	2.00	1.27	0.56
2.26	10.49	9.87	8.78	6.87	5.08	3.65	2.98	3.12	3.18	2.71	1.98	1.25	0.54
2.28	10.08	9.48	8.55	6.77	5.02	3.59	2.87	3.01	3.11	2.66	1.96	1.24	0.52
2.3	9.72	9.15	8.32	6.65	4.96	3.52	2.77	2.91	3.03	2.63	1.96	1.21	0.50
2.32	9.43	8.85	8.05	6.54	4.89	3.44	2.69	2.82	2.97	2.59	1.94	1.19	0.48
2.34	9.13	8.56	7.80	6.43	4.79	3.35	2.57	2.73	2.90	2.57	1.93	1.15	0.46
2.36	8.79	8.25	7.52	6.29	4.71	3.27	2.48	2.63	2.83	2.55	1.94	1.15	0.43
2.38	8.32	7.87	7.25	6.12	4.61	3.20	2.38	2.50	2.74	2.55	1.96	1.13	0.39
2.4	7.85	7.52	6.95	5.93	4.50	3.12	2.28	2.39	2.65	2.53	1.98	1.14	0.39
2.42	7.51	7.22	6.64	5.72	4.38	3.03	2.18	2.29	2.58	2.50	1.98	1.14	0.38
2.44	7.24	6.94	6.37	5.52	4.27	2.97	2.09	2.19	2.50	2.48	1.97	1.12	0.37
2.46	6.93	6.59	6.12	5.33	4.16	2.90	2.01	2.05	2.42	2.45	1.98	1.11	0.36
2.48	6.52	6.18	5.86	5.16	4.06	2.84	1.93	1.95	2.33	2.41	2.00	1.11	0.36
2.5	6.09	5.81	5.56	4.97	3.96	2.80	1.87	1.84	2.26	2.38	1.98	1.13	0.36

Table 8.3e: Continuation of table 8.3

Time, ms	Radial position, mm												
	0	10	20	30	40	50	60	70	80	90	100	110	120
	0	10	20	30	40	50	60	70	80	90	100	110	120
2.52	5.78	5.49	5.25	4.75	3.84	2.74	1.82	1.75	2.16	2.34	1.97	1.12	0.38
2.54	5.48	5.20	4.96	4.53	3.74	2.69	1.79	1.68	2.09	2.29	1.95	1.13	0.38
2.56	5.09	4.85	4.71	4.32	3.62	2.63	1.74	1.61	2.01	2.24	1.95	1.14	0.39
2.58	4.59	4.46	4.48	4.11	3.49	2.59	1.71	1.54	1.93	2.18	1.92	1.16	0.42
2.6	4.11	4.12	4.23	3.91	3.35	2.55	1.70	1.50	1.84	2.11	1.89	1.17	0.43
2.62	3.81	3.85	3.94	3.71	3.21	2.50	1.67	1.47	1.79	2.05	1.85	1.18	0.44
2.64	3.58	3.60	3.64	3.49	3.09	2.44	1.66	1.43	1.72	2.00	1.82	1.19	0.45
2.66	3.32	3.32	3.36	3.28	2.98	2.38	1.64	1.41	1.64	1.93	1.80	1.22	0.48
2.68	2.99	2.99	3.14	3.07	2.88	2.31	1.62	1.38	1.58	1.86	1.79	1.24	0.50
2.7	2.60	2.63	2.91	2.87	2.77	2.26	1.61	1.37	1.51	1.80	1.76	1.27	0.53
2.72	2.26	2.32	2.65	2.67	2.66	2.17	1.61	1.37	1.46	1.71	1.73	1.30	0.57
2.74	1.97	2.03	2.35	2.48	2.53	2.13	1.59	1.38	1.41	1.63	1.69	1.32	0.60
2.76	1.67	1.74	2.02	2.27	2.38	2.06	1.58	1.35	1.35	1.56	1.66	1.34	0.63
2.78	1.31	1.35	1.73	2.08	2.20	2.00	1.57	1.35	1.30	1.49	1.63	1.35	0.66
2.8	0.89	0.94	1.49	1.87	2.04	1.92	1.55	1.34	1.26	1.41	1.61	1.37	0.67
2.82	0.45	0.59	1.24	1.66	1.89	1.85	1.54	1.35	1.22	1.35	1.56	1.39	0.71
2.84	0.12	0.29	0.96	1.44	1.76	1.79	1.54	1.36	1.19	1.29	1.53	1.39	0.74
2.86	-0.12	0.04	0.62	1.23	1.64	1.73	1.52	1.35	1.17	1.24	1.50	1.39	0.73
2.88	-0.36	-0.22	0.31	1.02	1.51	1.65	1.52	1.37	1.14	1.20	1.46	1.39	0.74
2.9	-0.66	-0.53	0.04	0.83	1.38	1.59	1.50	1.35	1.13	1.14	1.43	1.38	0.76
2.92	-1.04	-0.86	-0.19	0.62	1.26	1.53	1.49	1.35	1.11	1.11	1.40	1.37	0.75
2.94	-1.49	-1.16	-0.39	0.42	1.09	1.47	1.48	1.36	1.10	1.08	1.36	1.33	0.73
2.96	-1.86	-1.44	-0.61	0.22	0.90	1.41	1.48	1.36	1.07	1.04	1.31	1.29	0.70
2.98	-2.20	-1.69	-0.86	0.02	0.75	1.36	1.45	1.34	1.07	1.02	1.28	1.24	0.69
3	-2.51	-2.00	-1.12	-0.21	0.59	1.27	1.42	1.34	1.07	1.01	1.25	1.20	0.66

Table 8.3f: Continuation of table 8.3

Time, ms	Radial position, mm												
	0	10	20	30	40	50	60	70	80	90	100	110	120
	0	10	20	30	40	50	60	70	80	90	100	110	120
3.02	-2.82	-2.34	-1.41	-0.44	0.45	1.21	1.40	1.32	1.06	1.00	1.22	1.14	0.63
3.04	-3.15	-2.72	-1.66	-0.64	0.34	1.13	1.38	1.33	1.05	0.99	1.18	1.08	0.58
3.06	-3.49	-3.05	-1.88	-0.85	0.24	1.08	1.34	1.31	1.06	0.97	1.12	1.01	0.56
3.08	-3.75	-3.33	-2.07	-1.05	0.12	1.02	1.28	1.27	1.04	0.98	1.11	0.96	0.53
3.1	-3.97	-3.56	-2.31	-1.22	-0.01	0.95	1.23	1.25	1.04	0.97	1.07	0.89	0.49
3.12	-4.18	-3.79	-2.61	-1.46	-0.19	0.89	1.18	1.25	1.05	0.98	1.03	0.84	0.46
3.14	-4.42	-4.05	-2.94	-1.67	-0.38	0.83	1.14	1.24	1.05	0.98	0.98	0.76	0.43
3.16	-4.76	-4.33	-3.25	-1.87	-0.54	0.78	1.10	1.24	1.07	0.99	0.93	0.69	0.38
3.18	-5.11	-4.66	-3.52	-2.09	-0.65	0.70	1.06	1.24	1.08	0.98	0.89	0.62	0.34
3.2	-5.50	-4.93	-3.77	-2.28	-0.77	0.61	1.01	1.22	1.09	0.97	0.84	0.56	0.32
3.22	-5.79	-5.22	-4.01	-2.48	-0.86	0.52	0.97	1.21	1.11	0.98	0.81	0.50	0.27
3.24	-6.04	-5.47	-4.27	-2.66	-0.97	0.42	0.94	1.22	1.13	0.99	0.76	0.42	0.22
3.26	-6.24	-5.72	-4.54	-2.87	-1.12	0.27	0.92	1.24	1.15	0.97	0.68	0.35	0.16
3.28	-6.44	-6.03	-4.84	-3.07	-1.28	0.16	0.88	1.23	1.17	0.96	0.63	0.28	0.14
3.3	-6.69	-6.31	-5.09	-3.30	-1.50	0.03	0.82	1.21	1.18	0.98	0.60	0.25	0.11
3.32	-6.96	-6.64	-5.30	-3.50	-1.70	-0.11	0.74	1.19	1.18	0.96	0.60	0.22	0.08
3.34	-7.28	-6.94	-5.51	-3.69	-1.86	-0.22	0.66	1.18	1.19	0.96	0.52	0.19	0.09
3.36	-7.58	-7.17	-5.70	-3.88	-2.01	-0.30	0.60	1.17	1.21	0.94	0.48	0.09	0.04
3.38	-7.80	-7.37	-5.92	-4.06	-2.14	-0.40	0.54	1.18	1.21	0.89	0.43	0.05	0.01
3.4	-8.03	-7.57	-6.14	-4.22	-2.27	-0.52	0.45	1.18	1.22	0.89	0.39	-0.02	-0.03
3.42	-8.31	-7.78	-6.35	-4.39	-2.41	-0.68	0.34	1.17	1.24	0.89	0.35	-0.06	-0.07
3.44	-8.62	-8.04	-6.61	-4.58	-2.58	-0.82	0.28	1.15	1.24	0.89	0.33	-0.09	-0.08
3.46	-8.95	-8.31	-6.82	-4.79	-2.76	-0.99	0.21	1.14	1.24	0.86	0.32	-0.11	-0.10
3.48	-9.26	-8.53	-7.00	-4.99	-2.98	-1.14	0.16	1.11	1.25	0.85	0.28	-0.15	-0.09
3.5	-9.53	-8.72	-7.15	-5.19	-3.18	-1.29	0.12	1.08	1.23	0.81	0.26	-0.17	-0.10

References

[1] M. Grujicic, B. P. DEntremont, B. Pandurangan, J. Runt, J. Tarter, and G. Dillon, "Concept-Level Analysis and Design of Polyurea for Enhanced Blast-Mitigation Performance," *Journal of Materials Engineering and Performance*, Dec. 2011.

[2] S. Okie, "Traumatic brain injury in the war zone.," *The New England journal of medicine*, vol. 353, pp. 633–4, Aug. 2005.

[3] R. A. Hurley, L. A. Hayman, K. H. Taber, D. Ph, and D. L. Warden, "Windows to the Brain, Blast-Related Traumatic Brain Injury: What Is Known?," *Journal Of Neuropsychiatry*, vol. 18, no. 2, pp. 141–145, 2006.

[4] N. Gardner, E. Wang, P. Kumar, and A. Shukla, "Blast Mitigation in a Sandwich Composite Using Graded Core and Polyurea Interlayer," *Experimental Mechanics*, June 2011.

[5] M. R. Amini, J. Isaacs, and S. Nemat-Nasser, "Investigation of effect of polyurea on response of steel plates to impulsive loads in direct pressure-pulse experiments," *Mechanics of Materials*, vol. 42, pp. 628–639, June 2010.

[6] G. Mcshane, C. Stewart, M. Aronson, H. Wadley, N. Fleck, and V. Deshpande, "Dynamic rupture of polymermetal bilayer plates," *International Journal of Solids and Structures*, vol. 45, pp. 4407–4426, Aug. 2008.

[7] C. M. Roland, D. Fragiadakis, and R. M. Gamache, "Elastomer-steel laminate armor," *Composite Structures*, vol. 92, no. 5, pp. 1059–1064, 2010.

[8] M. Grujicic, W. C. Bell, B. Pandurangan, and P. S. Glomski, "Fluid/Structure Interaction Computational Investigation of Blast-Wave Mitigation Efficacy of the

Advanced Combat Helmet," *Journal of Materials Engineering and Performance*, Aug. 2010.

[9] M. Grujicic, W. Bell, B. Pandurangan, and T. He, "Blast-wave impact-mitigation capability of polyurea when used as helmet suspension-pad material," *Materials & Design*, vol. 31, pp. 4050–4065, Oct. 2010.

[10] M. Grujicic, B. Pandurangan, T. He, B. Cheeseman, C.-F. Yen, and C. Randow, "Computational investigation of impact energy absorption capability of polyurea coatings via deformation-induced glass transition," *Materials Science and Engineering: A*, vol. 527, pp. 7741–7751, Nov. 2010.

[11] H. Kolsky, "Stress waves in solids," *Journal of sound and Vibration*, vol. 1, pp. 88–110, 1964.

[12] H. Hopkins and W. Prager, "The load carrying capacities of circular plates," *Journal of the Mechanics and Physics of Solids*, vol. 2, pp. 1–13, Oct. 1953.

[13] J. M. Walsh and R. H. Christian, "Equation of State of Metals from Shock Wave Measurements," *Phys. Rev.*, vol. 97, pp. 1544–1556, Mar. 1955.

[14] S. Katz, D. G. Doran, and D. R. Curran, "Hugoniot Equation of State of Aluminum and Steel from Oblique Shock Measurement," *Journal of Applied Physics*, vol. 30, no. 4, pp. 568–576, 1959.

[15] S. P. Carter, W. J. Marsh, "Hugoniot Equation of State of Polymers," tech. rep., 1995.

[16] J. Dodge, "Ch4: Polyurethanes and Polyureas," in *Synthetic Methods in Step-growth Polymers* (M. E. Rogers and T. E. Long, eds.), ch. 4, pp. 197–265, John Wiley & Sons, Inc., 2003.

[17] S. Tekalur, a. Shukla, and K. Shivakumar, "Blast resistance of polyurea based layered composite materials," *Composite Structures*, vol. 84, pp. 271–281, July 2008.

[18] M. Grujicic, T. He, B. Pandurangan, F. R. Svingala, G. S. Settles, and M. J. Hargather, "Experimental Characterization and Material-Model Development for Microphase-Segregated Polyurea: An Overview, url = http://dx.doi.org/10.1007/s11665-011-9875-6, year = 2011," pp. 1–15.

[19] W. Mock Jr., S. Bartyczak, G. Lee, J. Fedderly, and K. Jordan, "Dynamic properties of polyurea 1000," *AIP Conf. Proc.*, vol. 1195, pp. 1241–1244, Dec. 2009.

[20] M. Grujicic, T. He, B. Pandurangan, F. R. Svingala, G. S. Settles, and M. J. Hargather, "Experimental Characterization and Material-Model Development for Microphase-Segregated Polyurea: An Overview," *Journal of Materials Engineering and Performance*, Feb. 2011.

[21] Correlated Solutions Inc., "Vic-3d user manual," 2006.

[22] S. Cooreman, D. Lecompte, H. Sol, J. Vantomme, and D. Debruyne, "Identification of Mechanical Material Behavior Through Inverse Modeling and DIC," *Experimental Mechanics*, vol. 48, pp. 421–433, Nov. 2007.

[23] S. Cooreman, D. Lecompte, H. Sol, J. Vantomme, and D. Debruyne, "Elasto-plastic material parameter identification by inverse methods: Calculation of the sensitivity matrix," *International Journal of Solids and Structures*, vol. 44, pp. 4329–4341, June 2007.

[24] M. H. H. Meuwissen, C. W. J. Oomens, F. P. T. Baaijens, R. Petterson, and J. D. Janssen, "Determination of the elasto-plastic properties of aluminium using a mixed numerical-experimental method," *Journal of Materials Processing Technology*, vol. 75, pp. 204–211, Mar. 1998.

[25] S. Xu, V. Tiwari, X. Deng, M. A. Sutton, and W. L. Fourney, "Identification of Interaction Pressure Between Structure and Explosive with Inverse Approach," *Experimental Mechanics*, Aug. 2010.

[26] R. E. Barker L. M. Hollenbach, "Shock-Wave Studies of PMMA, Fused Silica, and Sapphire*," *Journal of Applied Physics*, vol. 41, pp. 4208–4226, 1970.

[27] G. Yiannakopoulos, "A Review of Manganin Gauge Technology for Measurements in the Gigapascal Range," tech. rep., Materials Research Labs Ascot Vale (Australia), 1990.

[28] G. S. Settles, *Schlieren and Shadowgraph Techniques*. Springer, 2001.

[29] T. Yamada, K. Kani, and A. Morita, "Shock Compression of Polymethylmethacrylate From 20 to 80 Kilobars," in *Proceedings of the 13th International Congress on High Speed Photography and Photonics*, pp. 743–746, 1978.

[30] A. H. Jones, W. M. Isbell, and C. J. Maiden, "Measurement of the Very-High-Pressure Properties of Materials using a Light-Gas Gun," *Journal of Applied Physics*, vol. 37, no. 9, pp. 3493–3499, 1966.

[31] D. Grady, M. Elert, M. D. Furnish, R. Chau, N. Holmes, and J. Nguyen, "the Shock Wave Profile," *AIP Conference Proceedings*, pp. 3–11, 2007.

[32] H. Hamad and A. Frohn, "Structure of fully dispersed waves in dusty gases," *Zeitschrift für angewandte Mathematik und Physik ZAMP*, vol. 31, pp. 66–82, Jan. 1980.

[33] D. Tsukinovsky, E. Zaretsky, and I. Rutkevich, "Material behavior in plane polyurethane-polyurethane impact with velocities from 10 to 400 m/sec," *Journal De Physique. IV : JP*, vol. 7, no. 3, pp. 335–339, 1997.

[34] A. K. Maji, J. P. Brown, and G. S. Urgessa, "Full-Scale Testing and Analysis for Blast-Resistant Design," *Journal of Aerospace Engineering*, vol. 21, no. 4, pp. 217–225, 2008.

[35] N. Gebbeken, S. Greulich, and A. Pietzsch, "Hugoniot properties for concrete determined by full-scale detonation experiments and flyer-plate-impact tests," *International Journal of Impact Engineering*, vol. 32, pp. 2017–2031, Dec. 2006.

[36] R. Houlston, J. Slater, N. Pegg, and C. Desrochers, "On analysis of structural response of ship panels subjected to air blast loading," *Computers & Structures*, vol. 21, no. 1-2, pp. 273–289, 1985.

[37] G. Nurick, "Deformation of thin plates subjected to impulsive loading–a review Part II: Experimental studies," *International journal of impact engineering*, vol. 8, no. 2, pp. 171–186, 1989.

[38] M. Hargather and G. Settles, "Laboratory-scale techniques for the measurement of a material response to an explosive blast," *International Journal of Impact Engineering*, vol. 36, pp. 940–947, July 2009.

[39] J. LeBlanc and A. Shukla, "Response of E-glass/vinyl ester composite panels to underwater explosive loading: Effects of laminate modifications," *International Journal of Impact Engineering*, vol. 38, pp. 796–803, Oct. 2011.

[40] J. Den Hartog, *Advanced strength of materials*. Dover books on engineering, Dover Publications, 1987.

[41] P. S. Symonds and T. Wierzbicki, "Membrane Mode Solutions for Impulsively Loaded Circular Plates," *Journal of Applied Mechanics*, vol. 46, no. 1, pp. 58–64, 1979.

[42] W. Baker, "Approximate techniques for plastic deformation of structures under impulsive loading," *The shock & vibration digest*, vol. 7, no. 7, pp. 107–117, 1975.

[43] Hapco Inc., "Ultralloy ultraclear." product borchure, 2010.

[44] A. Products and I. Chemicals, "Versalink p-1000 curative." product bulletin, 2011.

[45] A. Products and I. Chemicals, "Versalink p-650 curative." product bulletin, 2011.

[46] J. Runt. personal communication, 2011.

[47] K. Holzworth. personal communication, 2011.

[48] A. E. Seigel, *The Theory of High-Speed Guns*. Advisory Group for Aerospace Research and Development Neuilly-sur-seine (France), 1965.

[49] K. Uehara and M. Sakurai, "Bonding strength of adhesives and surface roughness of joined parts," *Journal of Materials Processing Technology*, vol. 127, pp. 178–181, Sept. 2002.

[50] P. Flynn and M. Frocht, "On Saint Venant's Principle under dynamic conditions," *Experimental Mechanics*, no. January, pp. 16–20, 1961.

[51] H. Kolsky, "Stress waves in solids," *Journal of Sound and Vibration*, vol. 1, no. 1, pp. 88–110, 1964.

[52] D. Radford and G. Willmott, "Failure mechanisms in ductile and brittle materials during Taylor impact," *Journal de Physique*, vol. 110, pp. 687–692, Sept. 2003.

[53] M. J. Hargather and G. S. Settles, "Optical measurement and scaling of blasts from gram-range explosive charges," *Shock Waves*, vol. 17, pp. 215–223, Oct. 2007.

[54] R. Kinslow, *High-velocity impact phenomena*. New York, NY, USA: Academic Press, inc., 1 ed., 1970.

[55] P. W. Cooper, *Explosives Engineering*. Wiley-VCH, 1996.

[56] J. Wackerle, "Shock-wave compression of quartz," *Journal of Applied Physics*, vol. 33, no. 3, p. 922, 1962.

[57] M. J. Hargather. personal communication, 2011.

[58] H. Miura and I. I. Glass, "On the passage of a shock wave through a dusty-gas layer," *Proceedings of the Royal Society of London. Series A, Mathematical and Physical*, vol. 385, no. 1788, pp. 85–105, 1983.

[59] K. Yano and Y. Horie, "Particle velocity dispersion in shock compression of solid mixtures," in *Shock Compression of Condensed Matter - 1997, 27 July-1 Aug. 1997*, AIP Conf. Proc., (USA), pp. 259–262, AIP, 1998.

[60] Y. Horie and S. Case, "Mesodynamics of shock waves in a polycrystalline metal," *Shock Waves*, vol. 17, pp. 135–141, June 2007.

[61] D. Z. Zhang, "Shock Dispersion in Composite Material with Polymer Binder," *AIP Conference Proceedings*, vol. 706, pp. 1073–1078, July 2004.

[62] M. Grujicic, B. Pandurangan, W. C. Bell, B. A. Cheeseman, C.-F. Yen, and C. L. Randow, "Molecular-level simulations of shock generation and propagation in polyurea," *Materials Science and Engineering: A*, vol. In Press,.

[63] W. J. Carter and S. P. Marsh, "Hugoniot equation of state of polymers," tech. rep., Los Alamos National Lab., NM, 1995.

[64] M. M. Biss and G. S. Settles, "On the Use of Composite Charges to Determine Insensitive Explosive Material Properties at the Laboratory Scale," *Propellants, Explosives, Pyrotechnics*, vol. 35, pp. 452–460, Oct. 2010.

[65] W. E. Baker, *Explosions in air*. University of Texas Press, 1973.

[66] M. M. Biss. personal communication, 2012.

[67] G. F. Kinney and K. J. Graham, *Explosive shocks in air*. Springer, Verlag, 1985.

[68] J. Anderson, *Modern Compressible Flow: With Historical Perspective*. McGraw-Hill Series in Aeronautical and Aerospace Engineering, McGraw-Hill, 2004.

[69] G. Munday and D. M. Newitt, "The Deformation of Transversely Loaded Disks under Dynamic Loads," *Philosophical Transactions of the Royal Society A: Mathematical, Physical and Engineering Sciences*, vol. 256, pp. 1–30, Dec. 1963.

Forrest R. Svingala
Forrest.Svingala@gmail.com

Education

Ph.D. in Mechanical Engineering
The Pennsylvania State University, University Park, PA, 2009–7/2012 (expected)
GPA: 3.6/4.0
M.S. and B.S. in Mechanical Engineering
Rochester Institute of Technology, Rochester, NY, 2004–2009
GPA: 3.8/4.0

Research Experience

Doctoral Research — Penn State Gas Dynamics Lab, University Park, PA — Dr. Gary S. Settles, Advisor, 2009–Present

Dissertation: *Laboratory-Scale Blast Testing of Polymers*, sponsored by the Office of Naval Research

- Developed new techniques to optically measure the shock Hugoniot of polymeric materials with high-explosive and ballistic projectile shock initiation
- Experimentally measured the time-resolved 3-D deformation of polymer plates exposed to explosive blast waves
- Created computational models of explosive and projectile-impact scenarios with both CTH and Abaqus
- Designed and fabricated a high-speed schlieren/shadowgraph system and a light gas gun for use in this work

Masters Research — Rochester Institute of Technology, Rochester, NY — Dr. Benjamin Varela, Advisor, 2007–2009

Thesis: *Alkali-Activated Aerogels*, sponsored by the National Science Foundation

- Developed a new type of inorganic polymer aerogel by alkali-activation and sublimation drying of alumino-silicate clays

Technical Publications

Published Works

Grujicic, M., He, T., Pandurangan, B., Svingala, F. R., Settles, G. S., & Hargather, M. J. Experimental Characterization and Material-Model Development for Microphase-Segregated Polyurea: An Overview. *Journal of Materials Engineering and Performance* (2011)

Svingala, F. R., Hargather, M. J., & Settles, G. S. Modern Optical Methods for Determining the Shock Hugoniot of Transparent Solids. *28th International Symposium on Shock Waves* (2011)

Svingala, F. R., & Varela, B. Alkai Activated Aerogels. *Mechanical Properties and Performance of Engineering Ceramics and Composites IV - A Collection of Papers Presented at the 33rd International Conference on Advanced Ceramics and Composites* (2010)

Works in Preparation

Svingala, F. R., Hargather, M. J., & Settles, G. S. Optical Techniques for Measuring the Shock Hugoniot,with Ballistic Projectile and High-Explosive Shock Initiation. *International Journal of Impact Engineering* (2011)